OPTICAL CHARACTERISATION OF SINGLE QUANTUM DOTS EMITTING AT 1300 nm

PAR

Carl ZINONI

B. Sc. in Engineering Physics, Sheffield Hallam Univeristy, Royaume-Uni
de nationalité britannique

EPFL
ÉCOLE POLYTECHNIQUE
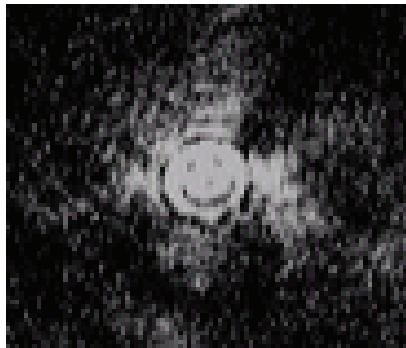FÉDÉRALE DE LAUSANNE

Lausanne, EPFL
2007

Optical characterisation of single quantum dots emitting at 1300nm

by

Carl Zinoni

Ecole Polytechnique Fédérale de Lausanne
Institute of Photonics and Quantum Electronics
Lausanne 2006

A 5µm mesa

Dedicated to my wife Rosa, and my children Alex and Sarah

Acknowledgments

The work documented in this thesis is the result of a common effort, after all there is no use for an ultra-stable super-efficient optical setup without anything to measure. I would like to start by thanking my thesis advisor Prof. Andrea Fiore for the countless hours spent on scientific discussions: I particularly appreciated his constant availability and high level of competence. I would like to thank Valery Zwiller who showed me my first steps in the field of experimental quantum optics, his enthusiasm for the subject and originality are unparalleled. I would like to thank and acknowledge the work of the members of the Quantum Devices group starting with: Blandine Alloing who produced the first low density quantum dots emitting at 1300nm, and Christelle Monat that processed the samples in collaboration with Lamberto Lunghi and Annamaria Gerardino (who work at the CNR in Rome). Also a special thanks to all the members of the group which contributed to make the working environment very pleasant: Laurent Balet, David Bitauld, Nicolas Chauvin, Lianhe Li, Alexander Marcus, Francesco Marsili, Pablo Moreno, Cyril Paranthoen, Phillip Ridha and Marco Rossetti.

I would like to thank the members of the IIS group at ETHZ who responded very positively when I contacted them for help in simulating our optical cavities: since then we setup a very healthy collaboration. Thanks to Peter Arbenz, Oscar Chinellato, Matias Streiff, Andreas Witzig and Bernd Witzigmann.

I am also grateful to the members of my thesis committee: Benoit Deveaud-Pledran, Jean-Michel Gerard, Robert Schaller and J Richard J. Warburton, for their constructive comments on the written thesis and for attending the defence.

Abstract

This thesis deals with the optical characterization of single quantum dot devices emitting at 1300nm. Thanks to the development and optimization of the growth technique we were able to achieve at the same time emission at 1300nm and ultra low QD densities. Our single QD devices present clear and reproducible spectral signatures in which we can identify exciton, biexciton and charged exciton transitions. Quasi-resonant excitation at 70K demonstrates background free single exciton transitions, which is very promising for the realization of a single photon device operating at temperatures in easy reach of thermoelectric coolers. A time-correlated single photon counting setup was built and used to measure the radiative lifetimes of single exciton transitions. These measurements also present new evidence on a background emission superposed to the narrow spectral transitions. Demonstration of single photon emission at these wavelengths required building a setup to measure the correlations between fiber-coupled single photons in a 300ps time window, emitted from a nano-device in free space at cryogenic temperatures, and with the capability of maintaining the optical alignment on a micrometer scale for several hours. With such a setup we have demonstrated that our QDs can generate single photon states at 1300nm. We used this single photon source to characterize novel detectors based on superconducting nanowires and measured for the first time the intensity correlation function at 1300nm on single photons from a QD. These detectors show at least 2 orders of magnitude improvement on the signal to noise ratio as compared to InGaAs APDs; this is very important since, for a QKD system, the detector noise, amongst others, determines the maximum distance over which a secure key can be exchanged. It should be noted that, due to the difficulties

in these measurements, to date there has been only one other clear demonstration of single photon emission at 1300nm.

Key words: single photon, quantum dot, spectroscopy, exciton lifetime, quantum cryptography, optoelectronics, detectors.

Astratto

Questa tesi tratta la caratterizzazione ottica di singoli dispositivi basati su punti quantici che emettono a 1300nm. Grazie allo sviluppo ed all'ottimizzazione della tecnica di crescita sono stati ottenuti allo stesso tempo l'emissione a 1300nm ed una densità ultra bassa di punti quantici. I nostri singoli dispositivi presentano chiare caratteristiche spettrali riproducibili in cui possiamo identificare l'eccitone, il bieccitone e le transizioni ecittoniche in presenza di altre particelle. Con la creazione di portatori direttamente nello stato eccitato ad una temperatura di 70K si ottengono transizioni eccitoniche in assenza del segnale di fondo: questo risultato è importante perché implica la possibilità di realizzare un dispositivo a singolo fotone che funziona a temperature facilmente raggiungibili con apparecchiature a raffreddamento termoelettrico. Un esperimento è stato sviluppato per misurare i tempi di vita dei portatori utilizzando rilevatori a singolo fotone. Le misure con questo sistema rivelano la presenza di un'emissione a larga banda sovrapposta alle strette righe spettrali. La dimostrazione di emissione di singolo fotone a queste lunghezze d'onda ha richiesto lo sviluppo e la messa a punto di un esperimento per misurare le correlazioni tra singoli fotoni accoppiati in fibra, in una finestra temporale di 300ps, emessi da un dispositivo a temperature criogeniche, e con la capacità di mantenere l'allineato ottico su una scala di qualche micrometro per parecchie ore. Abbiamo dimostrato che i nostri punti quantici possono generare singoli fotoni a 1300nm. Abbiamo usato questa sorgente a singoli fotoni per caratterizzare dei rivelatori superconduttori ed inoltre abbiamo misurato per la prima volta la funzione di correlazione di secondo ordine a 1300nm sui singoli fotoni emessi da un punto quantico.

Table of Contents

List of Abbreviations

AB	antibunching
AFM	atomic force microscope
APD	avalanche photodiode
BS	beam splitter
BP	band pass (filter)
CB	conduction band
cw	continuous wave
DCP	dark count probability
DE	detector efficiency
EBL	electron beam lithography
ES	excited state
em	electromagnetic
f	focal length
FIR	far infra-red
FWHM	full width at half maximum
GS	ground state
HBT	Hanbury-Brown and Twiss
LO	longitudinal optical (phonon)
MMF	multi mode fiber
NIR	near infra-red
PC	photonic crystal
PL	photoluminescence
Q	cavity quality factor
QBER	quantum bit error rate
qbit	quantum bit
QC	quantum computing
QD	quantum dot
QIP	quantum information processing
QKD	quantum key distribution
QW	quantum well
RF	radi frequency
SEM	scanning electron microscope
SMF	single mode fiber
SNR	signal to noise ratio
SPS	single photon source
SSPD	superconduction single photon detector
SRF	setup response function

TCSPC	time correlated single photon counting
TRPL	time resolved photoluminescence
UHV	ultra-high vacuum
VB	valence band
V_m	mode volume
WCP	weak coherent pulses
wd	working distance
WL	wetting layer
wrt	with respect to

Chapter 1

Introduction

The work documented in this thesis is part of a project which aims at developing a solid state single photon source based on quantum dots for quantum cryptography applications over telecom fibers. The outcome of the project relied on the successful research and development in two areas: optimization of epitaxial growth procedure for the realization of sparse quantum dots emitting in the telecom range and realization of an efficient optical bench with single photon sensitivity in the fiber-optic telecom windows (1300nm and 1550nm). This thesis documents the optical characterization of the single photon states produced by the device: by spatially isolating a single quantum dot we measured the integrated and time resolved photoluminescence to gain information about the carrier population and dynamics at the single exciton level. Single photon correlation experiments were used to characterize the statistics of the light emitted by the devices and we demonstrated single photon emission at 1300nm. At the time when the project was being set-up (2002) QKD experiments were (and still are) carried out using attenuated coherent sources: a single photon source at telecom wavelength was not available. Working with QDs emitting in the telecom window presents several challenges: first the QD emission has to be redshifted while maintaining a low spatial density - a difficult combination of requirements for conventional epitaxial growth methods. Second, the single photon detection technology for the near infrared is still in its infancy, and noise levels, quantum efficiency, and temporal response are considerably poorer

when compared to the single photon detection modules operating below 1000 nm based on silicon technology. Single-photon sources emitting in the visible and up to $1\mu m$ have been extensively characterized. In 2002, to our knowledge, there was only one reported integrated photoluminescence measurement on single quantum dots emitting around 1100nm (at 10K) using InGaAs technology [1]. During the course of this project some promising results on single quantum dot spectroscopy measurements at 1300nm and 1550nm have been published by various groups[2, 3, 4, 5]. On the other hand there has been only one other clear demonstration, besides the work reported in this thesis, of single photon emission in the telecom window[6].

1.1   The need for single photons

Manipulation of a single quantum state leads to the development of applications that are unachievable in the classical context. In particular the ability to generate, manipulate and detect single photon states leads to very interesting applications [7] such as: true random number generation[8], quantum cryptography [9, 10], and applications based on entangled photon states [11, 12] such as quantum computing. A true single photon source would also be an absolute standard of optical intensity. The application which is closest to a practical implementation is QKD, which involves the exchange of a secret key, encoded onto qubits, between two distant systems [9]. A qubit can take on values of 0 or 1, but it can also be in a mixture of both. While the security of classical cryptographic methods presents retroactive vulnerability and can be undermined by advances in technology and mathematical algorithms, the quantum approach can provide unconditional security. The secrecy is guaranteed by fundamental laws of quantum mechanics: any attempt to make a

measurement on qubits in a superposition of states will result in a collapse of the wavefunction onto one of the states. The impossibility to reconstruct the original superposition of states is guaranteed by the no-cloning theorem [13] that prevents the creation of identical copies of an unknown quantum state. It should be noted that quantum mechanics does not prevent from eavesdropping; it only enables us to detect the presence of an eavesdropper and since only the cryptographic key is transmitted, no information leak can take place.

The first protocol proposed by Bennet and Brassard in 1984, called BB84, is based on encoding Qbits on the polarization of the photon. The rectilinear basis is spanned by horizontally and vertically polarized photons (H and V), while the diagonal is spanned by photons polarized at 45 and 135(D and DD respectively). Any measurements in the diagonal (rectilinear) basis on photons prepared in the rectilinear (diagonal) basis will yield random outcomes with equal probabilities. On the other hand, measurements performed in the basis identical to the basis of preparation of states will produce deterministic results. At the beginning, the two parties that wish to communicate, traditionally called Alice a Bob, agree that, H and DD stand for the bit 0, and V and D stand for a binary 1. Alice, the sender, generates a sequence of random bits (the secret key) that she wants to transmit, and *randomly* for each bit she chooses her encoding basis, rectilinear or diagonal. Bob, the receiver, *randomly and independently* of Alice, chooses his measurement bases, either rectilinear or diagonal. Statistically, in 50% of the cases Bob's measurements provide deterministic outcomes and agree with Alice's bits. In order to know when the outcomes were deterministic, Alice and Bob have to exchange the sequence of basis used over a public channel. It should be noted that only information about

the used bases is exchanged, not the outcomes of the measurements. If Eve (the eavesdropper) measures each of Alice's photons and sends new photons to Bob she will introduce a 25% error rate into the key data, making it possible for Alice and Bob to detect eavesdropping. Although single-photon polarization is a convenient way to explain QKD, imperfections in real world telecom fiber make it unpractical and phase encoding is one of the most commonly used techniques [14]. An overview on QKD protocols can be found in [10].

For most of the demonstrated implementations of quantum key distribution, scientists have been using attenuated coherent sources (see section 1.3 for details) with emission in the 1300 and 1550nm region for transmission of approximate single photon states in the telecom fibers. A combination of vulnerability to attacks that exploit multiphoton pulses, detector dark counts and attenuation in the quantum channel limit the maximum distance to around 100km for fiber based communications[15]. The advantage of using a single photon source is that it is intrinsically secure from photon-number splitting attacks. Demonstrations of single photon source have achieved a $g^{(2)}(0)$ as low as 0.02 at 900nm [16] which means that there is a 50 fold decrease in the probability of emitting more than one photon per pulse as compared to a coherent source of the same intensity. Attenuated sources recover security through privacy amplification, which consists in masking the values of the qbits, at the expense of the usable key bit rate.

1.2   How to measure single photons

In Fig. 1.1 are represented the time distribution of photons for different types of sources. The statistical photon time distribution is accurately described by the

second order correlation function $g^{(2)}(\tau)$, which quantifies the probability of emitting a photon at time $t + \tau$ after a photon has been emitted at time t, normalized by the average probability of emitting a photon at any time. While bunched and coherent

Chaotic source: bunching

$g^{(2)}(0) > 1$

t

Coherent source: random

$g^{(2)}(0) = 1$

t

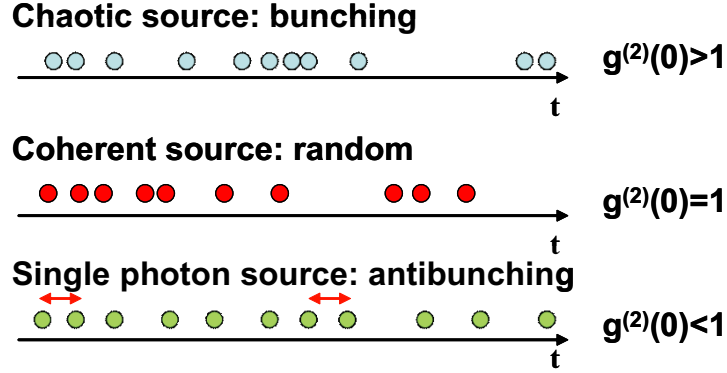**Single photon source: antibunching**

$g^{(2)}(0) < 1$

t

Figure 1.1: *Time distribution of photons from a thermal, coherent and non-classical emitter.*

light, $g^{(2)}(\tau) \geq 1$, are accurately described by the intensity correlation function for classical fields:

$$g^{(2)}(\tau) = \frac{\langle I(t)I(t+\tau) \rangle}{\langle I(t) \rangle^2}, \tag{1.1}$$

this function cannot describe the antibunching behavior since the numerator will always be larger than the denominator: $\langle I^2 \rangle \geq \langle I \rangle^2$. To describe the sub-Poissonian statistics of a single photon source we must resort to the quantum interpretation of a beam of light and the correlation function is expressed [17, 18] in terms of creation and destruction operators that operate on the field modes to increase or lower the energy by an amount $\hbar\omega$ equivalent to the energy of a single photon:

$$g^{(2)}(\tau) = \frac{\langle \hat{a}^\dagger(t)\hat{a}^\dagger(t+\tau)\hat{a}(t)\hat{a}(t+\tau) \rangle}{\langle \hat{a}^\dagger(t)\hat{a}(t) \rangle} \tag{1.2}$$

The value of $g^{(2)}$ goes to zero since two applications of the destruction operator to a single photon state $|1\rangle$ yields 0. If we consider a single mode of the field, Eqn. 1.2

becomes time-independent:

$$g^{(2)}(\tau) = \frac{\langle \hat{a}^{\dagger} \hat{a}^{\dagger} \hat{a} \hat{a} \rangle}{\langle \hat{a}^{\dagger} \hat{a} \rangle} = \frac{\langle n(n-1) \rangle}{\langle n \rangle^2}. \tag{1.3}$$

The correlation function is expressed in terms of the mean and mean-square photon

number (n) using the commutation relation, $\hat{a}\hat{a}^{\dagger} - \hat{a}^{\dagger}\hat{a} = 1$ and the photon number

operator $\hat{n} = \hat{a}\hat{a}^{\dagger}$. The magnitude of $g^{(2)}(\tau)$ as a function of the mean photon

number is obtained by using the definition of the photon number variance(Δn^2) and

eqn. 1.3:

$$\begin{aligned} (\Delta n^2) &= \langle n^2 \rangle - \langle n \rangle^2 \geq 0 \tag{1.4} \\ (\Delta n^2) &= \langle n \rangle^2 g^{(2)}(\tau) - \langle n \rangle^2 + \langle n \rangle \geq 0 \\ g^{(2)}(\tau) &\geq 1 - \frac{1}{\langle n \rangle}. \tag{1.5} \end{aligned}$$

The correlation function can take on values between 0, for a single photon state

input, and 1 for $n \gg 1$, which is consistent for a single mode beam.

From the representation in Fig. 1.1 it is straightforward to assume that the

$g^{(2)}(\tau)$ can be simply measured by time-stamping the clicks of the detector and

then by correlating the arrival times of the photons. The problem is that real

world detectors are inactive for a given length of time after detecting a photon and

current technology does not have photon-number resolving capabilities. An elegant

solution was proposed by Hanbury-Brown and Twiss [19] which consisted in feeding

the beam to the input of a symmetrical BS and then measuring the correlations

with two detectors between the reflected and transmitted beams. In this thesis the

ability of our sources to emit a single photon is established using this technique,

and in the following the theoretical proof that the intensity correlation between the

output beams from the BS is the second order correlation function of the input

beam is demonstrated. Figure 1.2 is a schematic of the beam splitter where $\hat{a}_i$ is the
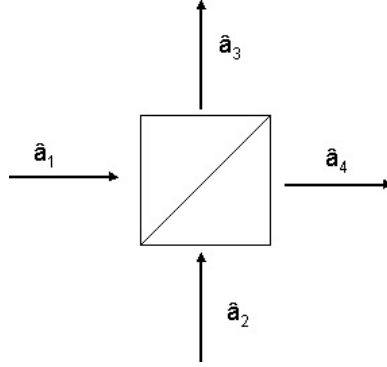

Figure 1.2: *Input and output fields with the associated destruction operators for a symmetric beam splitter.*

destruction operator associated with the input and output fields. From the classical input-output relations of a BS [17] and the correspondence principle, the lossless BS has the following properties:

$$\hat{a}_1 = R^*\hat{a}_3 + T^*\hat{a}_4 \tag{1.6}$$

$$\hat{a}_2 = T^*\hat{a}_3 + R^*\hat{a}_4 \tag{1.7}$$

$$\hat{a}_3 = R\hat{a}_1 + T\hat{a}_2 \tag{1.8}$$

$$\hat{a}_4 = T\hat{a}_1 + R\hat{a}_2. \tag{1.9}$$

where R and T are the reflection and transmission coefficients and:

$$|R|^2 + |T|^2 = 1 \ and \ RT^* + TR^* = 0. \tag{1.10}$$

We want to show that:

$$g_1^{(2)}(\tau) = g_{3,4}^{(2)}(\tau) \tag{1.11}$$

The mean photon outputs from the BS arms for an arbitrary input state $|m\rangle$ in arm 1 and a vacuum state $|0\rangle$ in arm 2 are:

$$\langle n_3 \rangle = {}_2\langle 0|_1\langle m|\hat{n}_3|m\rangle_1|0\rangle_2$$

$$= \ _2\langle 0|_1\langle m|(R^*\hat{a}_1^\dagger + T^*\hat{a}_2^\dagger)(R\hat{a}_1 + T\hat{a}_2)|m\rangle_1|0\rangle_2$$

$$= \ _1\langle m|(|R|^2\hat{a}_1^\dagger\hat{a}_1)|m\rangle_1 = |R|^2\langle n_1\rangle, \tag{1.12}$$

and for output in arm 4:

$$\langle n_4\rangle = |T|^2\langle n_1\rangle. \tag{1.13}$$

And the quantum mechanical average of the product is:

$$\begin{aligned}\langle n_3 n_4\rangle &= \ _2\langle 0|_1\langle m|\hat{n}_3\hat{n}_4|m\rangle_1|0\rangle_2 \\[6pt]
&= R^*RT^*T\,_1\langle m|\hat{a}_1^\dagger\hat{a}_1\hat{a}_1^\dagger\hat{a}_1|m\rangle_1 + R^*(-RT^*)T\,_1\langle m|\hat{a}_1^\dagger\hat{a}_1|m\rangle_1 \\[6pt]
&= |R|^2|T|_1^2\langle m|\hat{a}_1^\dagger\hat{a}_1\hat{a}_1^\dagger\hat{a}_1 - \hat{a}_1^\dagger\hat{a}_1|m\rangle_1 \\[6pt]
&= |R|^2|T|^2\langle n_1(n_1-1)\rangle. \tag{1.14}\end{aligned}$$

Writing the correlation between the output arms and making use of eqn. 1.3:

$$g_{3,4}^{(2)}(\tau) = \frac{\langle n_3 n_4\rangle}{\langle n_3\rangle\langle n_4\rangle} = \frac{\langle n_1(n_1-1)\rangle}{\langle n_1\rangle\langle n_1\rangle} = g_1^{(2)}(\tau) \tag{1.15}$$

1.3 Single photon 'guns'

Sources than can be used for quantum information applications fall in two categories: true single photon sources and attenuated coherent sources [20, 21]. In Fig. 1.3 are plotted the probability distributions, for the sources shown in Fig. 1.1, for an average photon number $\langle n\rangle = 1$. A thermal source follows the Bose-Einstein distribution of black-body radiation where the empty state has always the highest probability of occupation. The number of photons in a coherent state fluctuates according to Poisson statistics, which is an improvement over thermal light. Pulsed lasers that are used for demonstrations of QKD achieve low multiphoton probability by working with beams with an average photon number $\langle n\rangle < 0.1$ [22], which implies
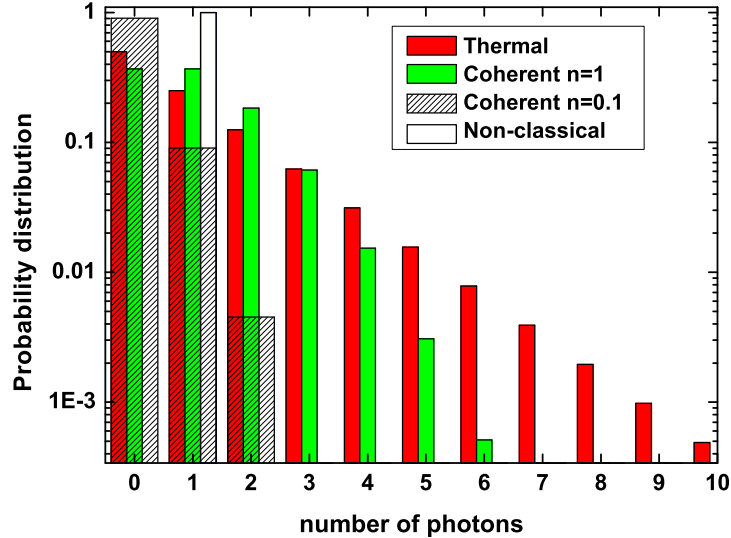
Figure 1.3: *Probability distributions for sources with an average photon number* $\langle n \rangle = 1$. *Textured plot gives the distribution for a coherent source with* $\langle n \rangle = 0.1$ *as used in QKD experiments.*

that most of the pulses are empty. This has the effect of reducing the SNR on the receiver's apparatus, since every pulse must be checked for the presence of a photon. The approximate 'single photon' performance of these emitters is compensated by the fact that they are easy to build and operate.

An ideal single photon source should have the following properties: due to the dispersion in fiber transmission a narrow emission linewidth is important, and a transform-limited emission is essential for quantum computing with linear optics. The emission wavelength of the device should overlap with the minima in the attenuation for the quantum communication channels: ~800nm for free space and 1300 and 1550nm for telecom fibers. A high extraction efficiency into the collection optics is required for achieving QKD exchange over long distances: the efficiency can be enhanced by controlling the position of the emitter in a cavity with a high Q/V_m ratio[23]. The emission properties must be stable in time: bleaching [24] and blinking[25] are not acceptable. The running cost should be low and the technology

9

simple: the use of UHV chambers and liquid helium will limit the use of the source to specialized research centers.

Table 1.1 summarizes the properties of single photon sources under development, demonstrating a wide variety of systems each one with it's own characteristics and advantages.

Table 1.1: Single photon sources characteristics. The values reported in the table are extracted from the references in the column headers.

Ref.	Cesium atom [26]	Heralded PDC [27]	TDI Molec. [28]	Molc. [29]	Col.cent. NV [30]	QD InAs III-V	Nanocr. CdSe [31]	QDs in nanowr. [32]
Linewidth	40neV	7nm	0.6neV	40meV	4meV	20μeV	120μeV	2meV
Lifetime	120ns	<1ps	3.4ns	4ns	10ns	1ns	30ns	500ps
Stability	No	Yes	Yes	No	Yes	Yes	No	Yes
Temp	μK	300K	1.4K	300K	300K	10K	300K	10K
Cavity	Yes	No	Yes	Yes	Yes	Yes	Yes	No
Site cont.	Yes	Yes	No	No	No	Yes	No	Yes
Technology	UHV	Easy	Liq.He	Easy	Easy	Liq.He	Easy	Liq.He

Atoms have Fourier limited transitions with high extraction efficiencies, but require a high level of technological complexity. Heralded single photon sources generated in a parametric down conversion (PDC) process change the light statistics of a beam from Poissonian to sub-Poissonian by elegantly suppressing the empty state [27]. Although this source is easy to implement it is not used for fiber transmission due to the broad linewidth. Similarly molecules and color centers although technologically easy have relatively broad emission and it is difficult to include them in cavities or address them electrically. Recent work [32] on QDs in nanowiers show promising results with very high extraction efficiencies, but more development is required to understand the origin of the broad line width and to investigate the

possibilities of tuning the optical mode density around the nanowires. II-VI QDs can be embedded in microcavities require simple technology, but they are not stable and have a broad emission linewidth. III-V semiconductor quantum dots present the best compromise between the optical properties and technological requirements. These quantum dots have narrow spectral width (we measured $\sim 30\mu$eV resolution limited), are tunable over the telecom window and by controlling the position of the QD [33] in high-Q and small mode volume cavities [34], reasonable repetition rates and efficiencies can be achieved[35].

1.3.1 Semiconductor quantum dots

QDs are nanometer-sized islands of semiconductor material embedded in other semiconductor material with a higher band gap. QDs are often referred to as "artificial atoms" although they contain from a few hundred to many thousand of atoms and the electrons move in the crystal lattice. The comparison with atoms arises from the nanoscale confinement which leads to the quantization of the kinetic energy, allowing only a few electrons and holes to populate the conduction and valence bands of the QD. The electronic and optical properties are sizably modified by the additional presence of a single charge through the Coulomb interactions. Fig. 1.4 shows the schematic structure of a QD obtained from the solution of the Schrödinger equation [36]. The confinement potential is a complex 3D field resulting from the combination of QD composition, shape, size, material, strain and piezoelectricity. The single particle Schrödinger equation is not enough to account for observed spectra since only certain solutions with a given symmetry are allowed: electrons are indistinguishable particles with spin 1/2 therefore must have antisymmetric wave
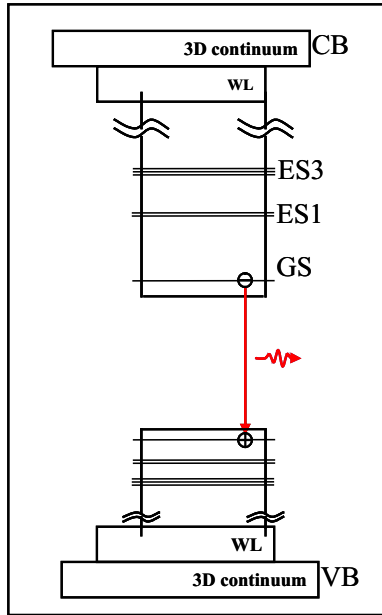
Figure 1.4: *Quantum dot energy levels, showing the recombination of an electron-hole pair on the ground state (GS) of the QD emitting a photon of energy equal to the energy level separation.*

functions. Three terms contribute to the Coulomb interaction between charges in the QD to lift the degeneracies of the energy levels: the direct Coulomb, the correlation and the exchange interactions. The magnitude of the changes in the electrical and optical properties due to the Coulomb interaction depends on the difference between the QD size and the exciton Bohr radius (the electron-hole separation). If the dot size is greater than the exciton Bohr radius, then the exciton binding energy is determined by the Coulomb interaction and the QD is said to be in a weak confinement regime. A dot size smaller than the Bohr radius (strong confinement regime) results in a strong quantization of the electron and hole kinetic energies. In this case the Coulomb interaction acts as a perturbation to the confinement potential giving rise to the possibility of forming antibinding biexciton complexes: the four-particle state is kept stable by the confining potential[37, 38]. Since the Bohr radius depends on the dielectric constant, it is easier to achieve strong confinement

12

in III-V materials rather than II-VI which requires a much smaller dot size.

1.3.2   Growth of low density QDs emitting at 1300nm

The quantum dots developed and optimized for this project were grown by molecular beam epitaxy. In MBE ultra-pure elements such as gallium and arsenic are heated in effusion cells until they slowly begin to evaporate into an UHV chamber where they can be adsorbed to the wafer surface and may react with each other (see Ref.[39] for further reading). This growth method yields high purity samples with the possibility of including abrupt interfaces for the realization of structures such as Bragg reflectors. The main problems with MBE are linked to the high technological complexity required for the ultra-high vacuum in the growth chamber.

Our dots are grown by evaporating In and As onto a GaAs substrate. Due to the lattice mismatch the InAs layer reaches a critical thickness beyond which it is energetically more favorable to form strained islands rather than continue a two dimensional growth mode. This is known as the Stranski-Krastanov growth method. The islands are subsequently buried to form the quantum dot, and in between the dots a wetting layer is formed from the InAs that was not included in the dots. This growth method presents several advantages: it is a simple growth mechanism, the emission wavelength is tunable by changing material concentration and growth parameters, and the structures have a high radiative efficciency. On the negative side it is not possible to control the nucleation site of the QD and due to size dispersion the PL is inhomogeneously broadened.

For this project we required large and thick QDs for emission at 1300nm at low temperature (10K) and a low dot density $< 10 dots/\mu m^2$: several growth techniques

where developed before [40, 41] and during this project [6] but none of them achieved at the same time low density and efficient PL at 1300nm. We used a combination of an ultra-low InAs growth rate and an InGaAs capping layer to obtain [42].

The optimization of the growth process involved finding the values for the In flux, sample temperature and As pressure that give at the same time low dot density and an efficient red-shifted PL signal. The convergence of the optimization process was verified by AFM and PL measurements. The effect of the individual parameters on the growth of the QDs is the following:

- by decreasing the In cell temperature, hence the In flux, a reduction of QD density is expected as a consequence of an increased migration length of the In adatoms on the substrate: it is energetically more favorable for In adatoms to be incorporated into existing dots instead of forming new ones,

- the temperature of the substrate during growth affects the dot formation process: high temperatures increase both the adatom mobility and the In desorption rate resulting in an increased QD size and low density,

- a low As pressure results in an increase of the diffusion length of the adsorbed atom, red-shits the PL emission and QDs have a higher QE. The optimum growth parameters were found to be: InAs growth rate=$2 * 10^{-3}$ML/s, As pressure=$5 * 10^{-7}$mbar and substrate temperature=505°C. Since these ultra-low growth rates are difficult to monitor with traditional methods, such as RHEED oscillations, the 2D-3D transition was timed by monitoring the RHEED pattern and by assuming a critical thickness of 1.7ML. With this method the growth rate could be estimated with an error of 10%.

In Figure 1.5(a) are plotted the QD densities as a function of growth rate:
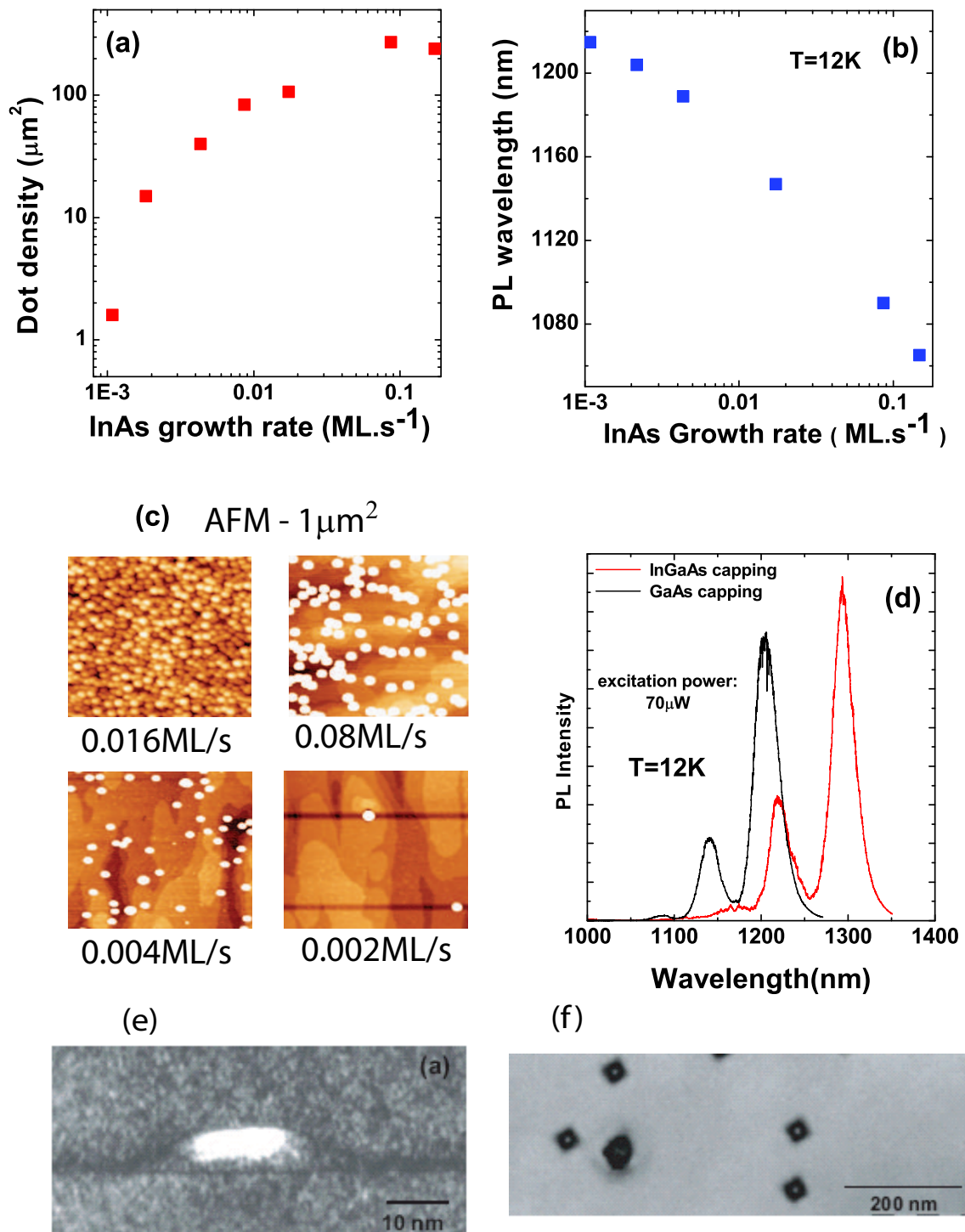
Figure 1.5: (a)Dot density vs. growth rate. (b) Emission wavelength vs growth rate. (c) AFM images of samples at different growth rates. (d) Comparison between the PL emission from samples with GaAs and InGaAs capping.(e) Dark-Field images of QDs grown at low InAs growth rate (0.0015ML/s) and capped by GaAs. (f) Plan view of QDs grown at low InAs growth rate (0.0015ML/s) and capped by GaAs.

15

for a rate of $2*10^{-3}$ML/s the dot density decreases to $< 2 dots/\mu m^2$. Figure 1.5(b) reports the trend of the PL as function of dot size: indeed we obtain a significant red shift in the emission spectrum and at the same time a low dot density. The redshift of PL peak emission wavelength is attributed to the increased QD size as demonstrated by the AFM images for samples with different growth rates (Fig. 1.5(c)). In order to further shift the PL emission to 1300 nm, we used an InGaAs capping layer to reduce the In segregation from the QDs. The best compromise between the red-shift in the PL and the efficiency was obtained for an In composition of 15% and a layer thickness of 5nm. A comparison for the PL spectra from samples with an InGaAs and a GaAs capping layer are reported in Fig. 1.5(d): we have achieved emission from the GS of the QD at 1300nm at 10K and low density dots. In Fig. 1.5(e) we show a cross-sectional dark field TEM image of the QDs capped with InGaAs: the QDs are lens shaped with a height of 7.5nm. From the plan-view image Fig. 1.5(f) the QDs have a square base and a mean width of 37.5nm along the $\langle 100 \rangle$ axis. The dimensions of the QD imply that the dots should be in a strong confinement regime since exciton Bohr radius in InAs is $\sim$34nm [43].

Chapter 2

Experimental methods

2.1 Micro-Photoluminescence

In general the difficulty of measuring the optical emission from a single QD lies in the low intensity of the signal. Since our QDs emit in the telecom wavelength range, InGaAs based technology with noise levels higher by more than 2 orders of magnitude when compared to silicon technology is required. As a consequence the measurements are much more challenging and the microphotoluminescence setup must be designed to reduce to a minimum the optical losses while maintaining a high spatial and spectral resolution.

A schematic of the optical setup is shown in Fig. 2.1. The pump station is composed of three cw diode lasers emitting at 660nm, 850nm and 980nm. The red (660nm) laser is used mainly for a rough alignment of the optical components. The 850nm and 980nm lasers were used for non-resonant excitation of carriers in the WL. A pulsed diode laser with a max rep frequency of 80MHz emitting at 750nm and a temporal jitter, at low power, of 50ps is used for TRPL and correlation measurements. All the light sources can be coupled into the same $50\mu m$ optical fiber (MMF) using flip mirrors, which makes it convenient to change between one source and another without having to realign all the optics. A high power 1300nm cw laser (not shown in the diagram) is used for fine tuning the optical alignment and the focal distances of the lens.

The laser light from the MMF is collimated with a 25mm lens and transmitted through a dichroic mirror which was custom made for our application to work at $45°$ with a reflectivity >99% for $\lambda > 1000nm$ and transmission greater than 50% for $\lambda < 1000nm$. The light is focused to a $\sim 4\mu m$ spot on the sample with a x100 objective (Mitutoyo NIR-series NA=0.5, wd=12mm and f=2mm). A 100mm lens can be placed in the path of the collimated laser beam to provide a uniform sample illumination for device identification: due to the monochromatic illumination shallow structures can be easily identified. The sample is held at 10K in a liquid helium flow cryostat equipped with two step-motors for moving the sample in the plane with a resolution of 100nm.
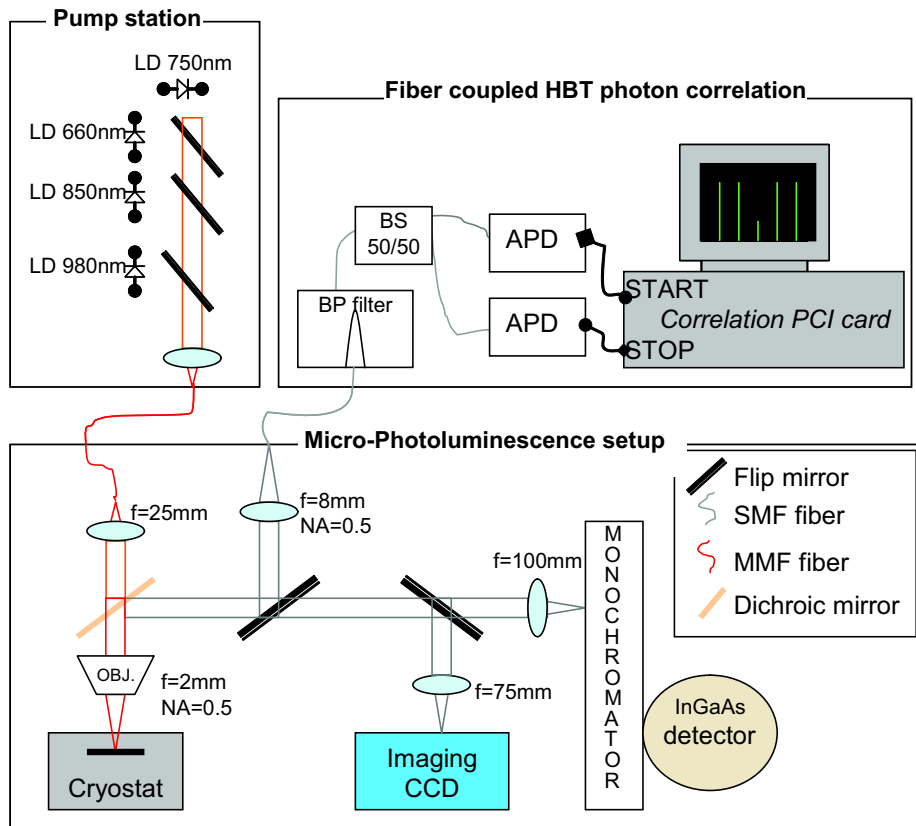

Figure 2.1: Optical setup for measuring PL, TRPL and antibunching.

The PL from the sample is collected by the same objective and the collimated

beam is reflected by the dichroic mirror. The light can be directed to single mode fiber coupling optics, or focused, by a planoconvex lens with a 100mm focal, onto the slits of a 1m monochromator which disperses the light onto an InGaAs array (IGA3000 HORIBA Jobin-Yvon, pixel dimensions: $25\mu m$X$500\mu m$) for spectroscopy measurements. The spectrometer is equipped with two gratings: the first is blazed at 900nm with 1200 lines/mm, while the second is blazed at 1000nm with 300 lines/mm.

A $1\mu m$ feature on the sample is imaged on the entrance slits with a spot size of $50\mu m$ and a NA of 0.01 which is compatible with the NA of the monochromator (NA=0.04). This implies that the light from the QD forms a spot at the entrance slits of the monochromator which is comparable to the width of a pixel of the InGaAs detector ($25\mu m$): no significant improvement in the resolution is gained by closing the slits hence all the light coupled into the objective is efficiently coupled into the spectrometer. In this configuration the resolution was measured to be below $30\mu eV$.

For time resolved and antibunching experiments the light is coupled into a SMF by an aspheric lens with a focal of 8mm and NA=0.5, the image of the 9um SMF core on the sample is $\sim 2\mu m$. The single exciton transition from the QD is spectrally filtered by a fiber-coupled tunable band pass filter (Santec-OTF 300 tunable between 1270nm and 1310nm with a FWHM of 0.8nm). For TRPL the fiber is directly connected to the optical input of an APD detector, while for correlation measurements a 1x2 splitter with a 50/50 ratio is used to feed the optical inputs of two APDs.

On of the major problems of working with QDs emitting at more that 500nm above the pump wavelength is that the objective cannot focus in the same focal

plane the laser and the QD PL due to chromatic aberrations. As a result the highest obtainable PL signal, in a free space spectroscopy measurement, is not achieved for the highest coupling efficiency of the light from the QD into the objective: focusing the laser light optimizes the power density but reduces the coupling of the PL into the objective, while focusing at 1300nm reduces considerably the power density. This is why a multimode fiber was used for guiding the laser pump light to the setup: the spatial distribution of the guided modes projected on the sample produces an approximate uniform spot as the objective is defocused, in contrast to the Gaussian spot from a SMF that gives origin to diffraction rings as the objective is defocused producing large local fluctuations in the power density. To solve this problem for experiments that require small excitation areas, we adjusted the divergence of the collimated laser beam to force the focal plane of the objective at 750nm to match the focal plane at 1300nm.

The alignment strategy used for coupling the single photons from a QD to the single mode fiber was the following: after a rough alignment of the light collected from the ensemble of dots, the single X emission was selected by the BP filter and the count rate monitored on the APD. By setting the pump power to saturate the X emission it is possible to optimize the coupling of the signal into the fiber.

2.1.1 A tunable laser between 1210nm and 1300nm

Quasi-resonant excitation measurement in the excited state of the QD require a tunable laser in the range 1200nm to 1270nm. Since such a laser does not exist on the market, we used the temperature dependence of the bandgap to tune the emission wavelength of a fiber-coupled telecom Fabry-Perot laser (Zarlink ZL60402)

emitting at 1300nm at room temperature. The electrical contacts of the laser chip housing were soldered directly to an SMA connector: the lowest pulse duration obtained was 47ps FWHM (Fig. 2.2a). The laser was pumped by a AVTECH pulse generator (AVM-2-C with 100ps rise time and 135ps fall time). To control the temperature, the laser was mounted on a cold finger together with a 10W resistor and a temperature sensor, the other end of the cold finger was dipped in liquid N_2. The laser wavelength could then be calibrated as a function of the temperature (Fig. 2.2b) by adjusting the power dissipated by the resistor. A PID controller was used to set and stabilize the output wavelength of the laser.
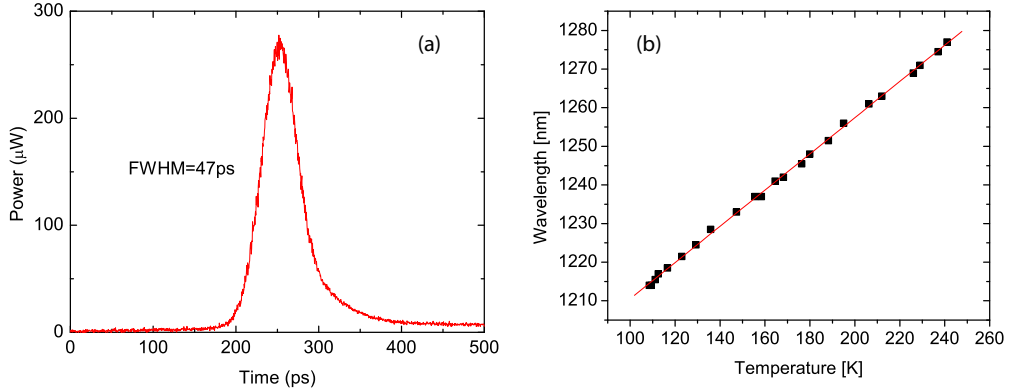

Figure 2.2: (a)Output laser pulse measured on a digital oscilloscope. (b)Calibration of laser emission wavelength as a function of temperature.

2.2 TCSPC

Time correlated single photon counting (TCSPC) is a technique that was developed for measuring the PL time evolution for very weak signals, since it takes advantage of the sensitivity of single photon detectors. The setup built for measuring the radiative lifetime on our QDs is more complicated than the standard TCSPC setups since the detectors are operated in gated mode. In Fig. 2.3 there
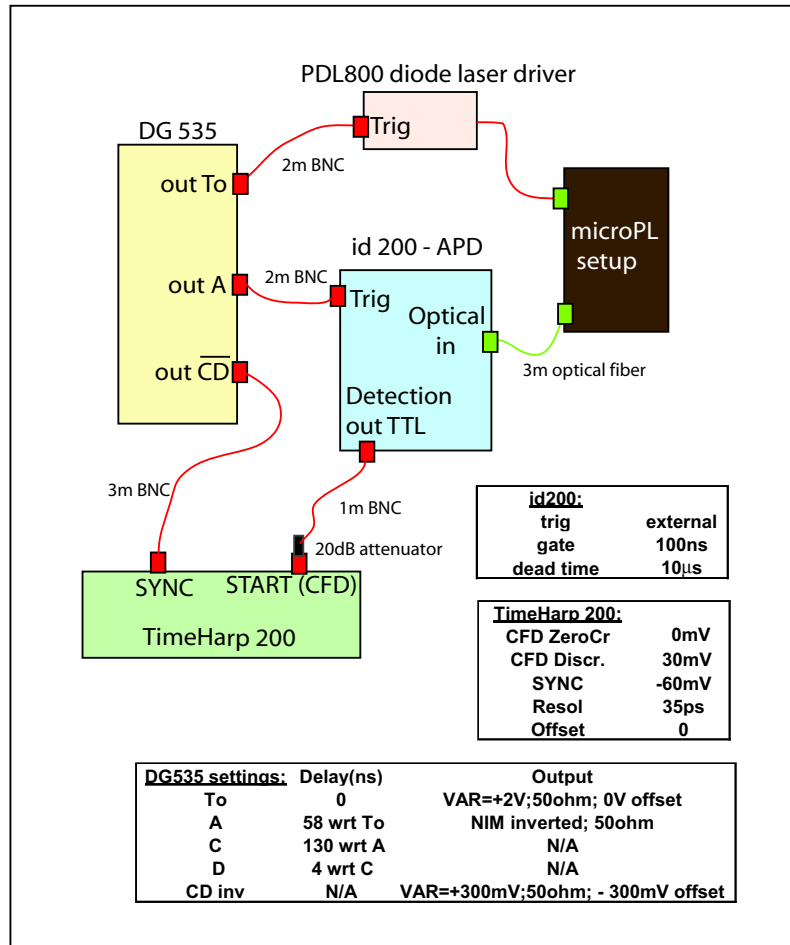
21

Figure 2.3: Detailed diagram of the setup used for TRPL measurements.

is a detailed diagram including all the instrument configurations. We used a delay generator (SRS-DG535) to coordinate the complex sequence of trigger signals for the different instruments. The APD gate must be activated when the light emitted from the QD is expected to arrive on the detector. If the APD detects an event it sends a trigger signal to the START input of the correlation card which must receive the synchronization pulse from the delay generator (the time reference signal) before 120ns have elapsed from the arrival of the detection pulse from the APD. Due to the high time resolution and high laser repetition rates used in TCSPC measurements, in this correlation card the traditional START-STOP inputs have been

replaced by SYNC-START inputs: the card measures the time between the photon arrival(START) and the next laser pulse(SYNC), then by inverting the time axis it reconstructs the correct fluorescence decay curve. The most critical settings are the trigger levels (SYNC and CFD) for the correlation card. The jitter and noise in the trigger pulses combined with the high resolution of the card, will result in different temporal resolutions for different trigger levels. It should be noted that the level settings shown in Fig. 3.13 are valid only for this setup; different instrumentation or different configurations require an optimization of the SYNC and CFD levels. The START input is designed as a Constant Fraction Discriminator to handle the output signals from SPADs and PMTs. In our setup we use clean pulses therefore the CFD Zero Cross setting should always be zero. A good introduction to TCSPC theory, techniques data analysis can be found in [44].

2.3   Antibunching setup

The antibunching setup used in this experiment is a fiber-coupled HBT setup with the added complexity arising from the detector gating. Due to the high dark counts the detectors are operated with an optical active window of 300ps. The synchronization of the different instruments is controlled by a 35MHz function generator (SRS-DS340, see Fig. 2.4): the SYNC signal triggers the laser pulse, while the OUT signal triggers the opening of the gates of the APDs. To get the values for the delay between the SYNC and the OUT signals in the correct order of magnitude, i.e. to synchronize the detector gate opening with the photon arrival time, we initially set long gates (100ns) and used high intensity signals (PL from QD ensemble). The gate duration is then gradually reduced and the delays tuned to achieve

the nominal 2.5ns gate length, corresponding to a ~300ps active window. For the final optimization the signal from the single exciton transition must be fed into the detectors and both the gate width and delay must be tuned to optimize the SNR. To measure the correlations for negative times we shifted the zero time delay (t_0) by introducing a $2.5\mu s$ delay on the output of one of the detectors with the delay generator (DG535).
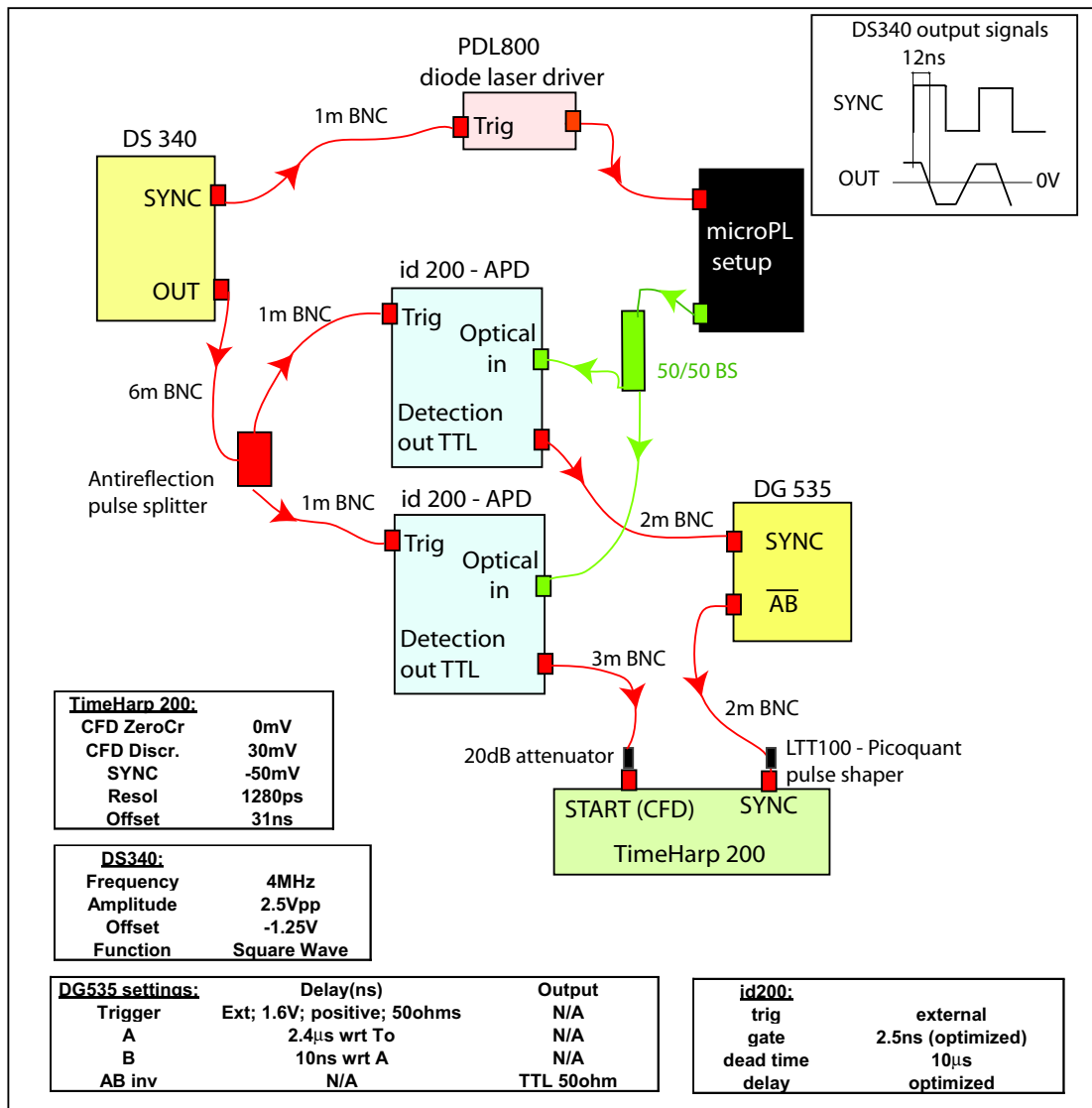

Figure 2.4: Detailed diagram of the setup used for antibunching measurements with SSPDs.

Due to the long integration times and mechanical instability it was necessary to

constantly monitor the count rates on the detector and control the optical alignment. For this purpose, the control signal of the X and Y movements of the cryostat sample holder, the piezo control voltage for the Z movement of the objective and the detector count rate were fed to an ethernet bus coupler (WAGO I/O-750): a simple software program (developed in LabView) running on a PC outside the lab could then be used to monitor and control the experiment in real time without interfering with the data acquisition.

The setup for measuring single photon correlations with the SSPDs (Fig. 2.5a) looks trivial when compared to the one for APDs since the SSPDs do not require any gating. Attention is only needed in setting the delay ($\sim 70ns$) between the SSPD and the SYNC input of the correlation card to ensure that the t_0 falls within the time window of the correlation card. The t_0 can be checked by feeding the signal from one SSPD (or any other source) to an antireflection splitter and by connecting the outputs to the correlation card as shown in Fig. 2.5b. The same configuration can be used to obtain the jitter of the correlation card. It should also be noted that the amplitude of a detection pulse from an SSPD depends on the level of the DC-bias, hence the trigger levels on the correlation card and the detector pulses should be regularly verified.
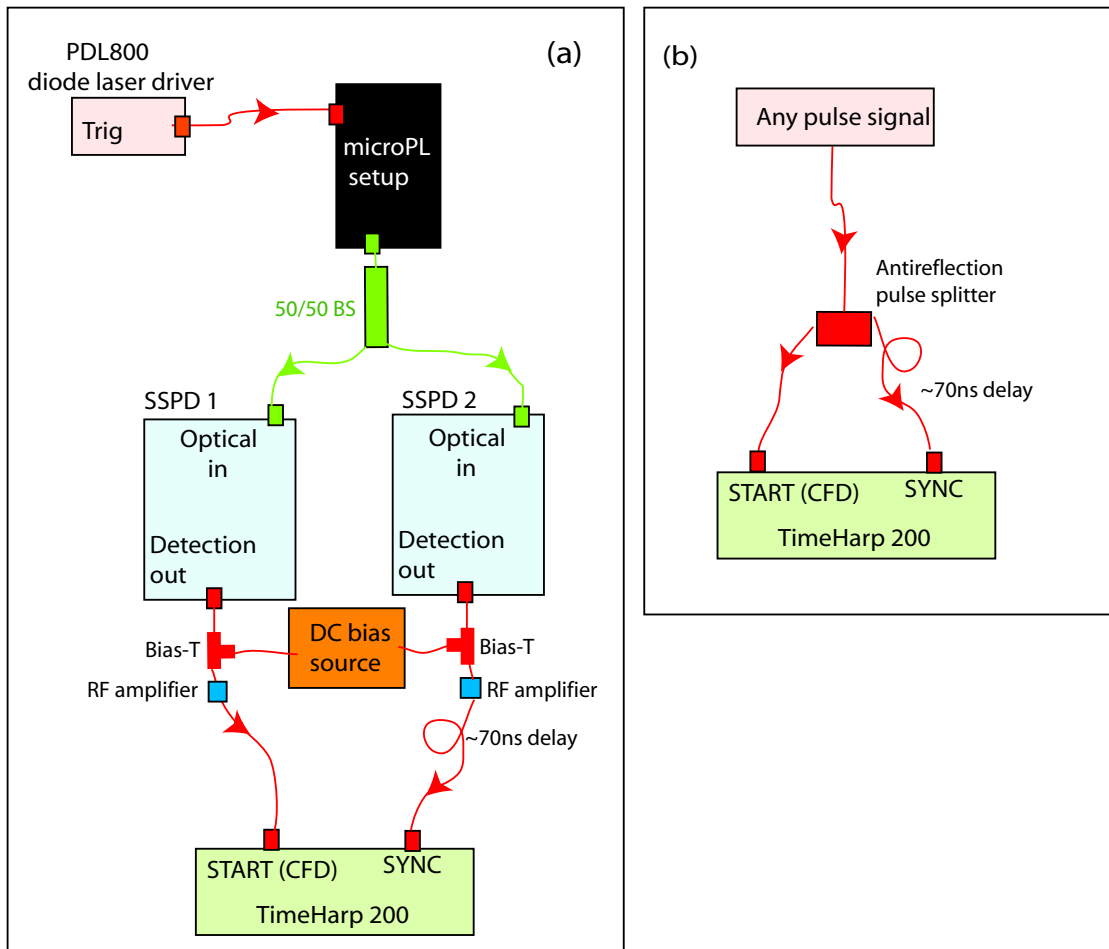
Figure 2.5: (a)Detailed diagram of the setup used for antibunching measurements with SSPDs.(b) Setup for setting To.

Chapter 3

Single QD spectroscopy

By spatially isolating a single QD in mesas or metallic apertures we measured the power dependence of a single QD PL spectra and related the spectral lines to specific charge configurations in the QD. An extraction efficiency grater than 10% was obtained for QDs embedded in planar microcavities. By spectrally isolating a single exciton transition line we measured the time dependence of the PL and used the results to fit the power dependence of the integrated PL signal from the X and BX lines with a simple rate equation model. Finally we discuss the experimental evidence of a background emission revealed in time-integrated and time-resolved measurements.

3.1   A single quantum dot device

The design of a single photon source device based on QDs requires consideration of two fundamental problems: the extraction efficiency and the spatial isolation of the emitter. As a first approximation a QD can be considered as an isotropic emitter embedded in a semiconductor material (GaAs n$\approx$3.4) with an index of refraction greater that air. A simple analysis of the problem, using Snell's law, shows that less than 2% of the QD emission can be extracted in air in a cone of light from the top of the sample. In most cases the efficiency is further reduced by the limited NA of the collection optics. Numerous light extraction strategies have been devel-

oped for the LED industry [45], but only few of them are applicable to our system, manly due to the spatial resolution required to isolate a single QD. To optimize the extraction efficiency into the NA of the objective we embedded our QDs in a planar microcavity with the aim of reducing the allowed optical modes to which the emitter can couple to [46]. This approach is more fundamental as compared to other collection strategies, since emission of the source is modified by the cavity: the emitted photons are funneled in the optical modes. A well designed microcavity can couple a large fraction of the emission of the dipole to a single mode having an angular distribution matching the extraction cone determined by the GaAs/air interface. A planar microcavity consists of a spacer embedded between two planar mirrors. The mirrors can be metallic, Distributed Bragg Reflectors (DBRs) or a combination of both. DBRs are periodic multilayer structures with a unit cell of two dielectric layers. Each unit cell, a DBR pair, consists of a low and high refractive index material with an optical thickness equal to $\lambda/4$ for the designed wavelength. The advantages of these mirrors is that they can be easily included in the device structure during the epitaxial growth. The reflectivity of a DBR covers a limited spectral range which changes with the incidence angle. The optical properties of DBRs can be calculated with the transfer-matrix formalism [47]. The microcavity designed for our quantum dots consisted of a bottom DBR (14 pairs of GaAs and $Al_{0.9}Ga_{0.1}As$), a λ GaAs cavity centered around a layer of QDs and a top reflector made by one DBR pair (see SEM photo Fig. 3.1a). The cavity was designed to achieve an extraction efficiency of 9% into an external NA of 0.5. PL from QDs embedded in the micro-cavity show more than an order of magnitude increase over QDs, grown in the same conditions, embedded in bulk GaAs (Fig. 3.1b), as expected
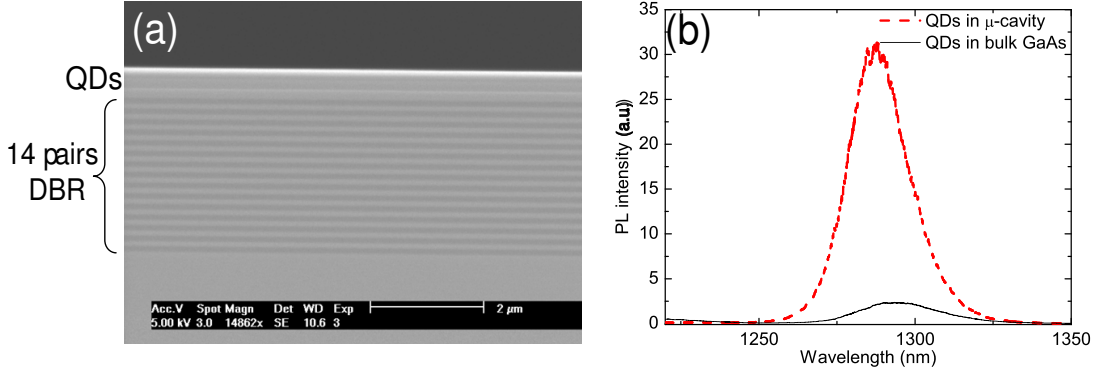
Figure 3.1: (a) SEM image of planar microcavity. (b) Comparison of PL intensity for QDs in bulk and buried in a planar microcavity.

from the calculation. The spatial resolution required to isolate a single QD depends on the QD density. The new growth method developed as part of this project [48], achieved densities as low as 1-2$dots/\mu m^2$ simplifying the task of QD isolation. Two different approaches where tested for isolating a single QD[49]. Mesas of 1-2μm by etching through the active region. The processing steps are described in Fig. 3.2a, where the aim is to first form the SiO_X masks used to define the mesas during the RIE etching step. The fact that the QDs are not embedded any more in a planar micro-cavities does not change significantly the pattern of the angular emission. The alternative method consists in using metallic apertures with diameters ranging from 3μm down to 800nm to limit both the injection and collection area. A uniform layer of resist (UV3) was spin-coated on the sample and the pattern was defined by EBL. After a 2min baking at 140°C the resist is developed and a Au-Ti alloy 120-140nm thick is evaporated onto the sample. Lift-off is realized in an ultrasonic bath of acetone for a duration of 10 min to expose the apertures (Fig. 3.2b). Both methods yield similar results as shown by the single QD PL in Fig. 3.2c. It was observed that mesas provide improved spectral isolation since in the metallic aper-
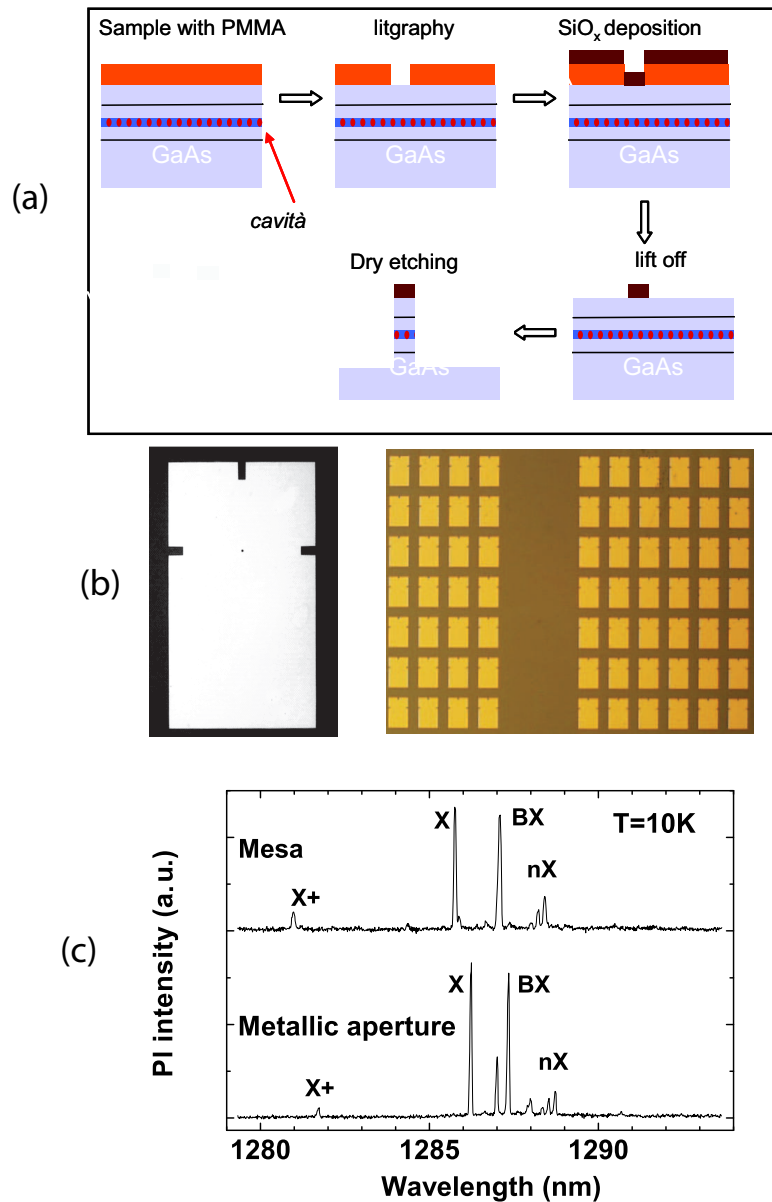
Figure 3.2: (a) Mesa processing steps. (b) SEM image of metallic apertures (pads are $10x15\mu m$). (c) Single quantum dot emission from the ground state isolated by a mesa and metallic aperture.

ture, light is collected from dots in the vicinity of the aperture contributing to a higher background. As compared to mesas, metallic apertures have a lower device yield due to problems related to the lift-off process: for a successful process a ratio of 10 is required between the thickness of the resist and the metal film. Thanks to the success in growing ultra low density dots , we where not confronted with the

problems reported in literature typical for high density QDs. High density samples require small diameter mesas that influence the carrier dynamics in the QDs [50], or small metallic aperture that cause losses due to diffraction effects.

For further reading on light propagation in optical media see [47], while for an overview on light collection strategies for single photon sources see [51, 52, 35] and for the concepts behind the design of planar cavities see [46, 53].

3.2   Non-resonant Photoluminescence

A QD can be optically excited in different ways, depending on where the photo-generated carriers are created. One method consists in creating a reservoir of carriers in the material surrounding the QD by tuning the laser energy to promote electrons into the conduction band of the wetting layer or of the bulk GaAs (Fig. 3.3a). The carriers then relax to lower energy states, through scattering events, and sequentially fill the confined energy levels of the QD and recombine through spontaneous emission to emit a photon. The second approach consists in tuning the laser to the energy states in the QD (see next section). Above-band excitation is a convenient way of generating carriers for several reasons. It is efficient since the absorber material (GaAs) is relatively thick requiring low power densities, and scattered laser light can be efficiently filtered since the emission wavelength is far from the emission of the QD. The photoluminescence spectrum of the ensemble of QDs, shown in Fig. 3.3b for high power density, is characterized by several broad peaks corresponding to the transitions represented in Fig. 3.3a between the confined energy levels in the QD. The transitions are broadened inhomogeneously by the contribution of the individual dots which emit at slightly different energies due to the
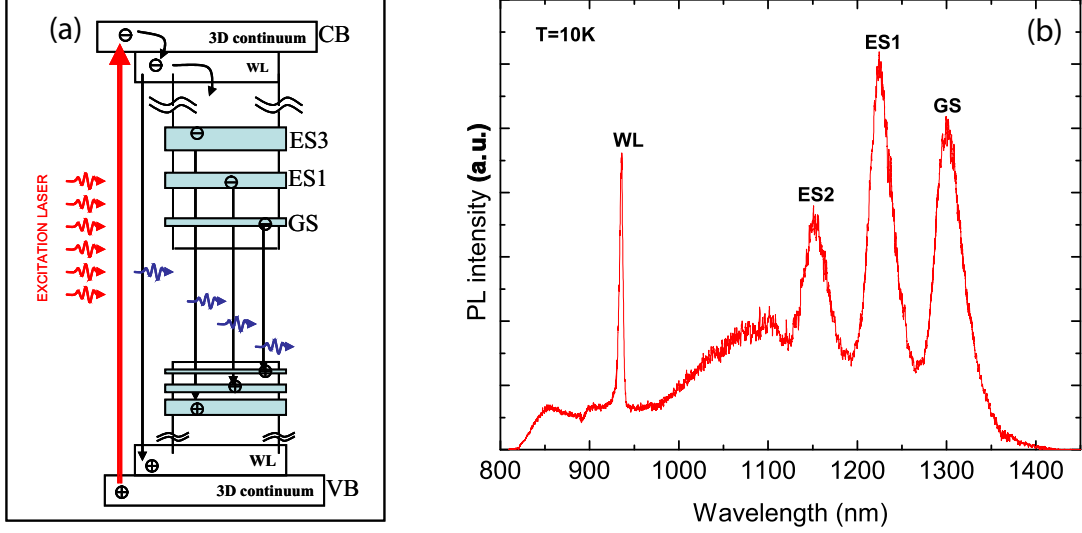
Figure 3.3: (a)Schematic of carrier capture of QD under non-resonant excitation.(b) PL from ensemble of dots at high excitation intensity, the background signal above 1000nm is due to emission from doping levels in the substrate.

size dispersion. The transition with the lowest energy corresponds to the emission of excitons recombining in the GS. The higher energy peaks correspond to emission from the higher excited states of the QD. At 940nm we identify an emission due to the exciton population in the WL. Non-resonant excitation provides a practical tool for investigating the confined energy structure of the QD: by increasing the excitation intensity of the laser the sequential filling of the QD states can be controlled. Assuming that the number of carriers excited above-band follow the same statistics of the incident laser, the capture probability is random and independent from the dot population, the probability (P_n) of finding n excitons in the QD is given by a Poisson distribution:

$$\mathbf{P_n} = \frac{\alpha^n}{n!} e^{-\alpha} \tag{3.1}$$

where α is the average number of excitons in the dot and is proportional to the intensity of the laser. P_n is plotted as a function of alpha for the first four excitons in Fig. 3.4(b) together with the spectra from the GS of a single QD for increasing

32

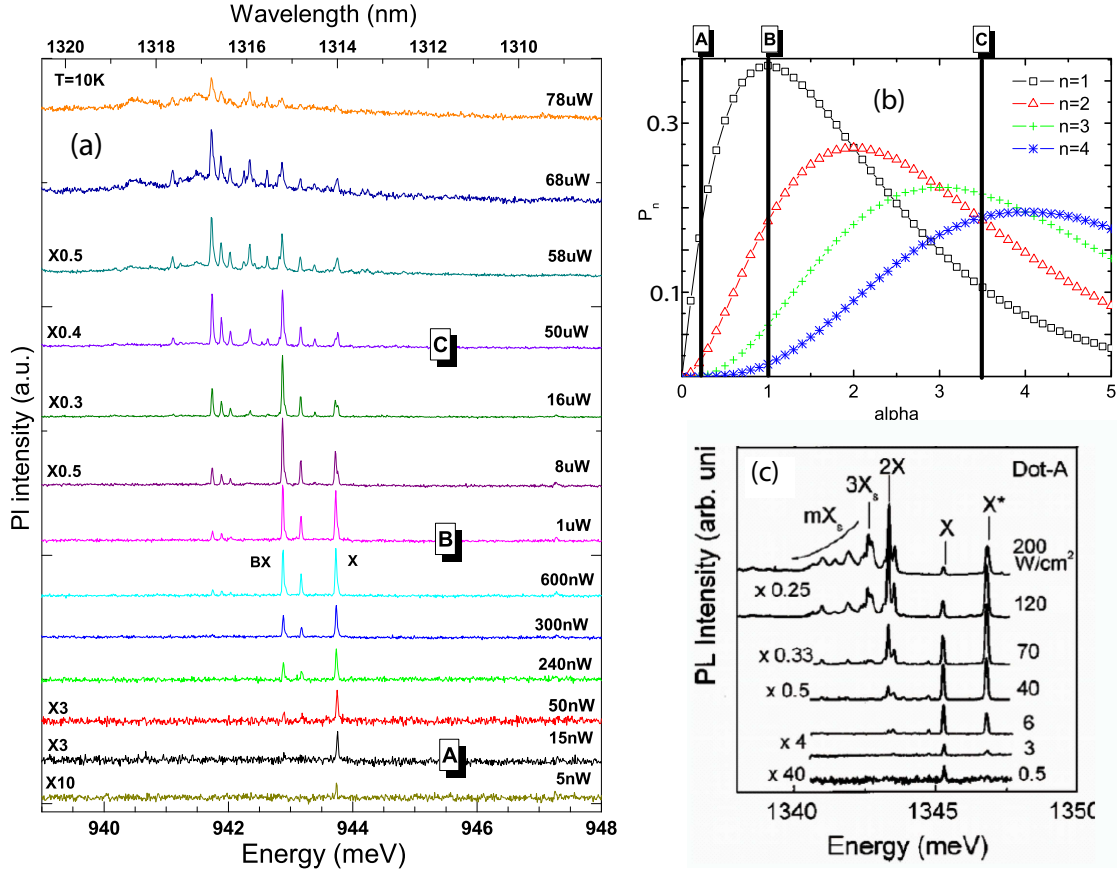cw laser excitation.   At the lowest excitation density a single line is present in

Figure 3.4: (a)Power dependence of the GS emission from a single QD.(b) Probability occupation as a function of average number of electron hole pairs in the dot (alpha).(c) PL from smaller QDs showing similar spectral features.

the spectrum, corresponding to the QD populated by a single exciton (marker A in Fig. 3.4b) in the GS. It should be noted that the position of the markers is only indicative. As the power is increased the intensity of the X increases due to the increased probability of finding an exciton in the QD, and more spectral lines begin to appear on the low energy side of the X transition, these lines correspond to the recombination of an electron-hole pair in the GS in the presence of other charges in the QD (marker B in Fig. 3.4b), the shift in energy of the new transition lines is due to the Coulomb interaction between the carriers (see below). At yet higher excitation

intensities the spectrum becomes more complex with the appearance of more lines, and the X peak reduces in intensity: due to the large number of carriers generated there is a higher probability of finding multiexciton complexes in the dot rather than the single exciton (marker C Fig. 3.4b). In general the intensity of any emission line under cw excitation increases, reaches a maximum, and then decreases as the excitation power is increased. It is interesting to note that there is a remarkable similarity in the spectral signatures between our QDs and the QDs emitting in the 900nm region studied by J.J.Finley *et al.* [54]: the clean multiexciton transitions indicates the presence of a larger confinement energy in our QDs (Fig. 3.4c).

Poisson statistics can also be used for describing the QD population for pulsed excitation, but in this case the probability of occupation only describes the initial condition after the laser pulse. The PL spectra at low power densities presents similar characteristics to the cw spectra, as shown in Fig. 3.5 where we compare the integrated PL intensities of the spectral lines marked X and BX as a function of excitation intensity for the two pump regimes. At low excitation power, the PL intensity dependence on the laser power P for both pump modes can be fitted by the relation $I_{X,BX} \propto P^n$, with $n = 0.70 \pm 0.05$ and 1.35 ± 0.05 for X and BX lines, respectively. This fit is only shown for the cw measurements. The fact that the ratio of the exponents is equal to 2 ($n_{BX}/n_X = 2$) confirms that the BX line corresponds to the biexciton emission. Under pulsed excitation at high power densities, unlike the cw case, both lines reach a maximum then the PL saturates at the same intensity: due to cascade emission the multiexciton state always decay to the single exciton state, so that a photon from the exciton recombination is emitted after each pulse. This is true only if the laser pulse duration is much shorter than
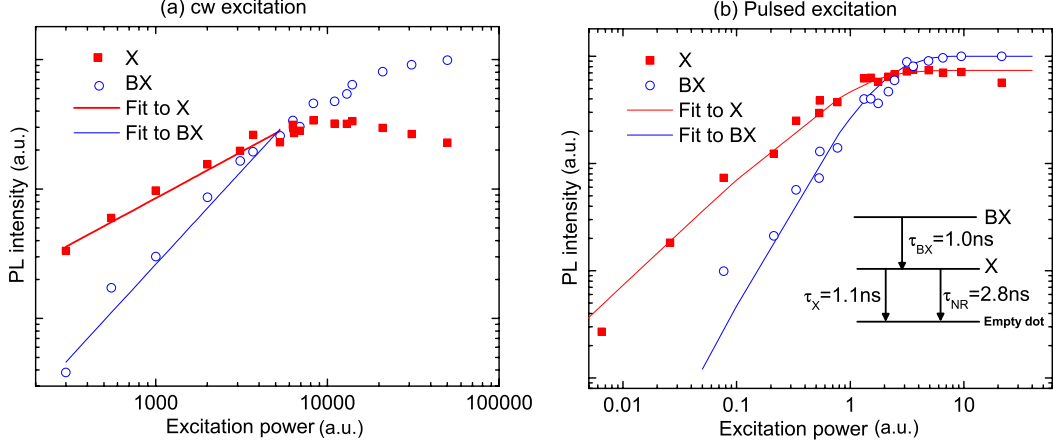
Figure 3.5: Integrated PL for X and BX under (a) cw excitation with fit to low power densities and (b) pulsed excitation with steady state solution to the system schematically represented in the inset.

the X lifetime and the repetition period is much longer than the time it takes to empty the dot. To model the change in PL intensity with excitation intensity, we used the following system of rate equations for the simple two level model shown as an inset in Fig. 3.5b:

$$\frac{dP_X}{dt} = \frac{P_{BX}}{\tau_{BX}} - \frac{P_X}{\tau_X} - \frac{P_{NR}}{\tau_{NR}}$$
$$\frac{dP_{BX}}{dt} = -\frac{P_{BX}}{\tau_{BX}}$$

assuming the initial populations:

$$P_0 = e^{\alpha}$$

$$P_X = \alpha e^{\alpha}$$

$$P_{BX} = 1 - P_0 - P_X$$

Where P_X and P_{BX} are the exciton and biexciton population probabilities, with the respective radiative lifetimes, τ_X and τ_{BX}, obtained from TRPL measurements on the same QD(section 3.4). The steady state solution of this system is used to fit the pulsed measurements in Fig. 3.5b. The only fitting parameter used in the model to

35

fit the experimental data is the value of τ_{NR} which represents a non-radiative decay channel for the exciton population and is responsible for reducing the saturation intensity.

The energy difference between the multiexcitonic peaks and the single X transition represents the binding energy of the multi-charge complex. It should be noted that there is no clear physical meaning in defining an exciton binding energy for a QD since it is not possible to populate a QD with a single hole and a single electron without them interacting [55]. In a QD the energy shift of an exciton transition due to the presence of spectator charges is given by the sum of the three Coulomb terms [56, 57]:

$$
\begin{aligned}
\triangle E_{e_1,h_1}^{(N_e,N_h)} &= \; [\varepsilon_{e_1} - \varepsilon_{h_1} - J_{e_1,h_1}] \\
&- \; [\sum_{i=2}^{N_e}(J_{e_1,e_i} - J_{h_1,e_i}) + \sum_{j=2}^{N_h}(J_{h_1,h_j} - J_{e_1,h_j})] \\
&+ \; [\Delta_{exch}^{(N_e)} + \Delta_{exch}^{(N_h)}] \\
&+ \; \Delta_{corr}^{(N_e,N_h)}.
\end{aligned}
\tag{3.2}
$$

The first term represents the transition energy of the neutral exciton, given by the sum of the single particles energies (ε_{e_1} and ε_{h_1}) and the Coulomb energy (J_{e_1,h_1}). The second term describes the direct Coulomb interaction between the spectator charges and the exciton. The third term takes into account the exchange energy arising from the spin of the system (the Hartree-Fock model[58]). The last term takes into account the correlation energy due to the change in the Coulomb interaction as a result of the perturbation of the wavefunctions. In a strongly confined system (Bohr radious>QD size) the electron and hole wavefunctions are determined by the confining potential, as a consequence the direct Coulomb energy always dominates

36

over the exchange and correlation terms. It should be noted that for a non-zero direct Coulomb term (second term in eqn. 3.2) the spatial distribution of the electron and hole wavefunctions must differ, for example in the case of InAs where the hole has a higher effective mass leading to a more localized spatial distribution as compared to the electron. As a consequence the addition of a hole to the GS of an InAs QD populated with an exciton will cause a blue shift in the emitted spectra: in the second term the first summation goes to zero while the second summation becomes positive [59]. In Fig. 3.6 we show the spectra for a QD pumped non-resonantly with a pulsed laser emitting at 750nm: the X and BX emission intensities have been identified through the power dependence (Fig. 3.5b). At low power densities the spectra is characterized by a sharp transition blue shifted with respect to the X transition by 5nm, on the basis of the analysis made above we attribute this line to the recombination of an electron hole pair in the presence of a spectator hole in the GS.
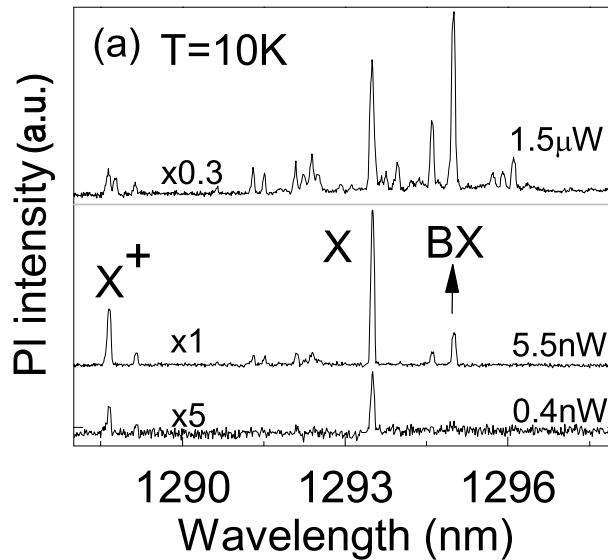

Figure 3.6: PL spectra of a single QD for increasing power densities under pulsed excitation.

In non-resonant excitation the spectra of a QD can change as the laser energy is tuned to excite in the GaAS bulk or in the WL. In Fig. 3.7 we show the spectra from a mesa that contains two QDs and for which we identify both the X and X+ line (labeled X_1, X_1^+, X_2, X_2^+). When exciting in the bulk a higher number of spectral lines are present in the spectra and for both dots we observe a group of lines redshifted by ~10nm. For QD_2 the lines overlap with the transitions of QD_1. A redshift in the binding energy suggest that the transition are due to negative charging of the dot. For InAs QDs, larger binding energies for the X^- as compared to the X^+ have been both calculated [60] and measured[61]. The emergence of negatively charged excitons as the pump energy is tuned to excite in the bulk GaAs has been already observed in InAs QDs and attributed to higher effective diffusivities[62].
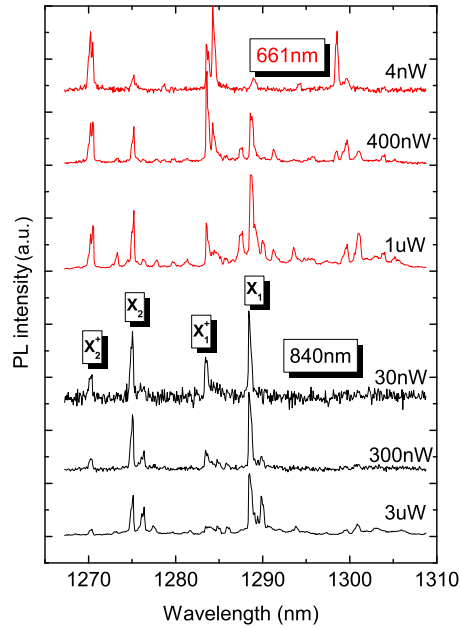

Figure 3.7: Comparison of the PL of two QDs in the same mesa for excitation in the GaAs and in the WL.

3.3 Resonant Photoluminescence

In quasi-resonant excitation, the laser is tuned to a higher transition within the quantum dot (Fig. 3.8a), so that electron-hole pairs are created directly, for example in the ES1, and can then relax to the GS where it recombines. A much larger laser power is required than for above-band excitation, since the absorption cross-section of a single quantum dot is very small. PL excitation spectroscopy (PLE) consist in measuring the intensity of the emission of the GS transition as the laser energy is scanned across the excited states. This technique is used to study the the relaxation mechanisms in QDs [63]. The major problem of making such measurements on our QDs is that to excite in the ES states we require a laser that is tunable between 1200nm and 1250nm. Although materials such as InGaAsP provide optical gain in the required spectral range, there is no commercial application and tunable lasers do not exist at these wavelengths. To pump in the excited state
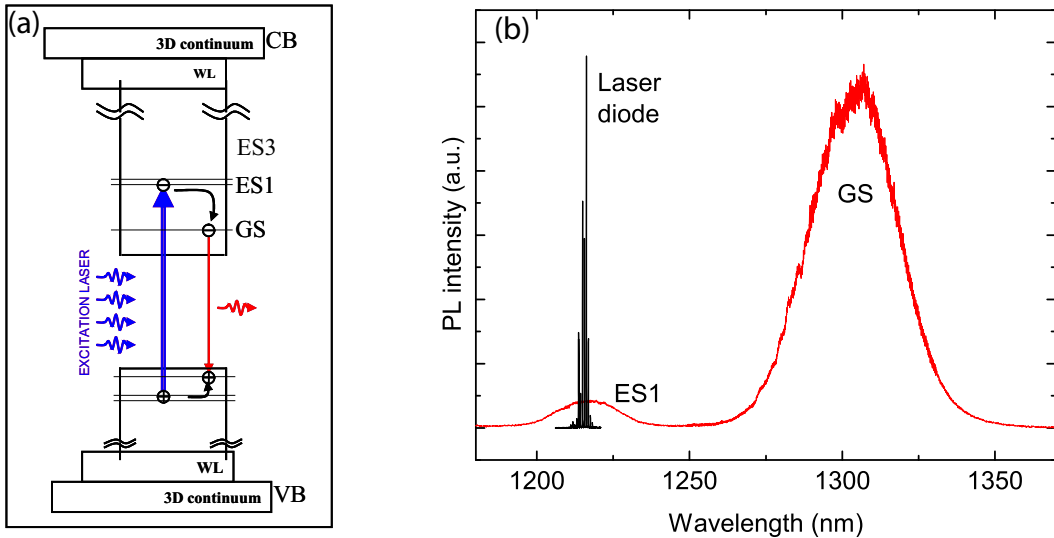

Figure 3.8: (a)Schematic of quasi-resonant excitation in the ES. (b) Spectra of the cooled laser diode (black line) and the QD ensemble at 10K under non-resonant excitation, showing the overlap of the laser with the ES1.

we took a standard telecom pulsed diode laser emitting at 1300nm and cooled it to approx 100K to achieve an emission around 1215nm to overlap the transition energy of ES1(Fig. 3.8b), as demonstrated in section 2.1.1. Although a Fabry-Perot cavity
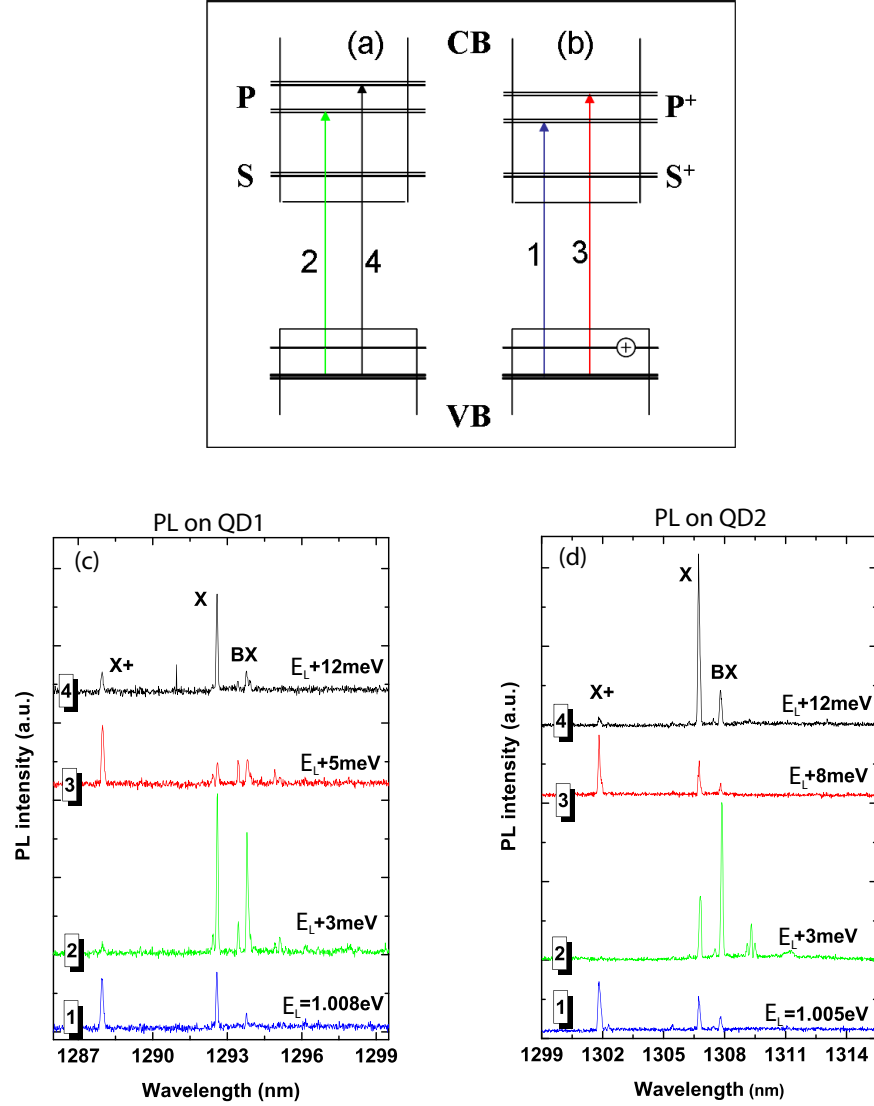
Figure 3.9: (a) and (b) schematic QD energy diagram for neutral dot and charged dot respectively. (c) PL for two QDs in separate mesas emitting at different energies for different pump power energies.

laser can be tuned over a wide spectrum the emission is multi-mode limiting the resolution of PLE measurements. The PL of the ground state of two QDs are shown in Fig. 3.9 as the laser is scanned across the excited states. The emission lines are

identified by comparison with the PL from non-resonant excitation. As the emission energy of the laser is scanned across the excited states, the spectra from the two dots present very similar features which are reproduced for the same relative change in excitation energy. In spectra 2 and 4 (Fig. 3.9c,d) a high PL efficiency is observed, with the neutral transitions dominating the spectrum: the laser energy is resonant in the ES1 states (Fig. 3.9a). In the spectra 1 and 3 (Fig. 3.9c,d) the intensity of the X+ line is enhanced, implying that the laser energy is resonant with the excited states of the charged exciton as shown in Fig. 3.9(b): the presence of a hole in the GS renormalizes the energy levels in the QD inducing a red shift.

The presence of charges in the surrounding of the QD also explains the origin of the gaussian line shapes as opposed to lorentzian (Fig. 3.10) as would be expected in quasi-resonant excitation [64, 65]. The advantages of quasi-resonant excitation
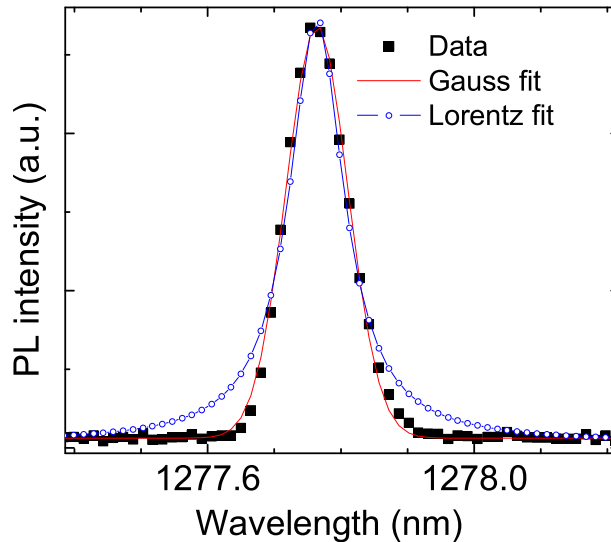

Figure 3.10: Positively charged exciton transition under quasi-resonant excitation showing the Gaussian profile of the spectral line.

become evident when we raise the temperature of the sample to about 70K. Fig. 3.11

compares the spectra of the same dot for an excitation wavelength of 750nm and
>1220nm at high temperature. Under resonant excitation we obtain a complete
suppression of the broad background emission and the recovery of the narrow PL
lines. To compare the spectra for similar QD populations under both excitation
regimes, a series of measurements showing the power dependence of the PL spectra
is need to obtain an accurate estimate of the background contribution to the PL
signal. The background emission is of particular relevance to our application since
it is a source of uncorrelated photon emission and deteriorates the single photon
light statistics of the device. A discussion on the background emission can be found
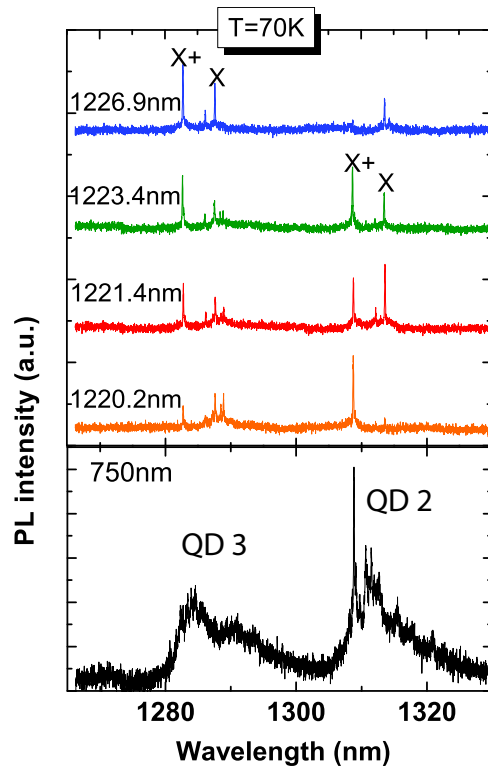in the last section of this chapter.

Figure 3.11: Quasi-resonant PL at 70K compared to non-resonant excitation.

3.4 Time resolved Photoluminescence

To study the rate of depopulation of the excitonic states we used the TCSPC setup described in section 2.2. This technique is well adapted for measurements on our long-wavelength emitting dots since it takes advantage of the high sensitivity of the single photon detectors. Other methods, such us up-conversion techniques and streak-cameras, are not suitable due to the low sensitivity at these wavelengths. The setup used in these experiments is more complicated as compared to standard TCSPC measurements since the APD must be gated. The arrival time of photons on the detector have to be synchronized with the opening of the gate and the time window of the correlation card. It must be noted that the APD resolution depends on the count rate hence it is important to measure the time resolution of the setup (SRF:setup response function) at a rate close to the experimental one. Due to the mismatch between the APDs spectral response and laser wavelength, the SRF (Fig. 3.12a) was measured with a sample of GaNInAs quantum wells, emitting at 1300nm at room temperature, with a lifetime previously measured to be 50ps [66], which is well below the temporal resolution of the detector ($\sim$600ps).
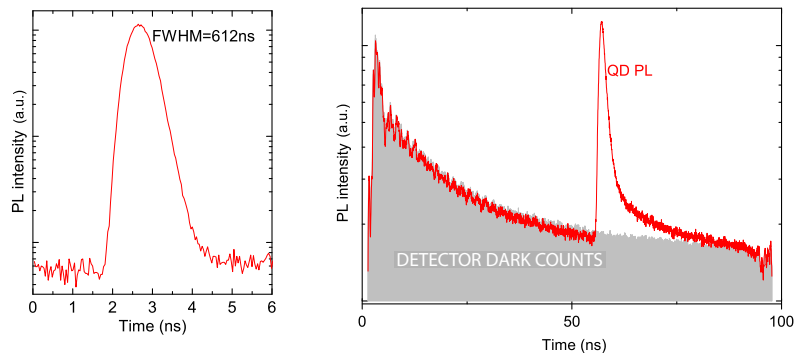

Figure 3.12: (a)Setup response function (SRF) measured on GaNInAs QW. (b) Raw TRPL measurement on a single exction (continuous line) and detector dark counts in a 100ns gate (filled gray area).

In Fig. 3.12b we compare a raw TRPL measurement on the exciton transition with a measurement of the same integration time but with the laser switched off: the shape of the 100ns gate used to measure TRPL presents unexpected features. The higher dark counts at the beginning of the gate are due to the way in which the APD functions: when an avalanche is detected the bias on the APD is switched off and for the remaining duration of the gate the APD is disabled. As a consequence there will be a greater number of events recorded at beginning of the gate. The ripples at the beginning and at the end of the gate are due to reflections in the electronics.
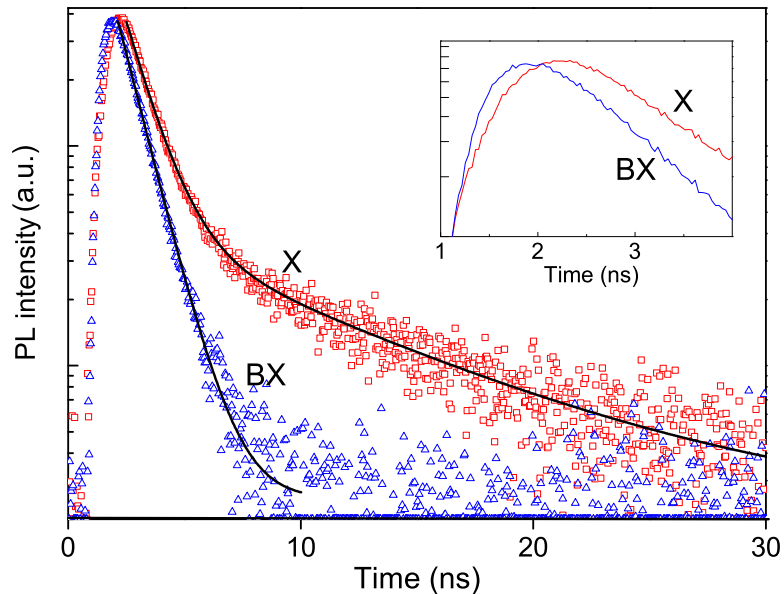
Figure 3.13: TRPL on single X and BX emission. Inset: evidence of cascade emission at short time delays.

By isolating the single X and BX transition with a narrow band pass filter we measured the time dependence of the single exciton transitions. The continuous lines in Fig. 3.13 show the least square fits to the decaying part of the PL for the X and BX after dark noise subtraction. The least square fits are calculated from the convolution between a two (one) term exponential decay function for the

44

X (BX) and the SRF. The error on the fits is estimated at ± 0.2ns. The delay in the start of the decay of the X emission compared to the BX, is evidence of cascade emission and validates the peak assignment (inset Fig. 3.13). The exciton lifetime is characterized by a double exponential decay of 1.1ns and 8.6ns: the fast component derives from the recombination of a bright exciton while, the slower decaying part suggests the presence of a dark exciton state that is repopulating the allowed exciton transition [67, 64]. A measurement of the temperature dependence of the exponential decay will be required to validate this conclusion. The BX decay time was measured to be 1.0ns: the ratio of 1.1 between the exciton and biexciton lifetime is consistent with previous studies on single QDs [68]. When the QD size is comparable to the Bohr radius, the Coulomb effects are not any more a small perturbation to the dominating quantization of the kinetic energy. For holes, the changes in the wavefunction spatial distribution are more significant, as compared to electrons, due to their higher effective mass. As a consequence, a larger QD size results in an increased spatial separation of the hole wavefunction, a reduction of the overlap integral and an increased BX radiative lifetime. From the cross-sectional TEM images (Fig. 1.5(f)) QDs have base dimensions of 37.5nm which is comparable to the exciton Bohr radius in bulk InAs (34nm [43]).

3.5 Discussion on QD background emission

In chapter 4 we show that, like atoms, QDs can produce single photon states, but unlike atoms QDs are not isolated from their environment. A constant reminder that we are dealing with a quantized energy system coupled to a continuum of states [63] is that the confined states in the QD can be populated by charges created in

the barriers by optical or electrical injection. The most compelling evidence found in literature that sets epitaxial QDs apart from atoms are the intensity correlation measurements on single exciton transition. QDs behave as perfect single photon emitters only under special measurement conditions. An increase in the number of excited carriers or a rise in the temperature show a degradation of the light statistics: the QD is emitting an uncorrelated signal together with the single photons as demonstrated in Fig. 4.7. Few reports [69, 70] have tried to explain the origin of this uncorrelated light and attribute the background emission to the overlap of phonon-broadened spectral lines belonging to the same QD or a separate one, but no clear evidence is presented that demonstrates the overlap of spectral lines. Next we present an overview of the data collected during this thesis in which we emphasize the presence of the background emission. In Fig. 3.14(a) we present the PL spectrum of a single QD populated by optically exciting carriers in the WL using a cw laser emitting at 835nm. At low power densities on average only a few carriers populate the dot and the spectra is dominated by narrow spectral lines. In contrast at high power densities a large number of carriers are present in the dot and in the surroundings: the spectrum shows a weak and broad emission with a few spectral features reminiscent of the narrow transitions.   In Fig. 3.14(b,c and d) we present the PL spectra, at 10K, of a single quantum dot populated by carriers excited in the bulk using a pulsed laser. At 250pW the spectra is dominated by narrow spectral transitions in which we can identify the X and BX, at 700pW the BX is saturated and a background signal starts to emerge. Three order of magnitude higher in power (262nW) the BX intensity has not changed but the background emission has become more intense and has spread over the spectrum
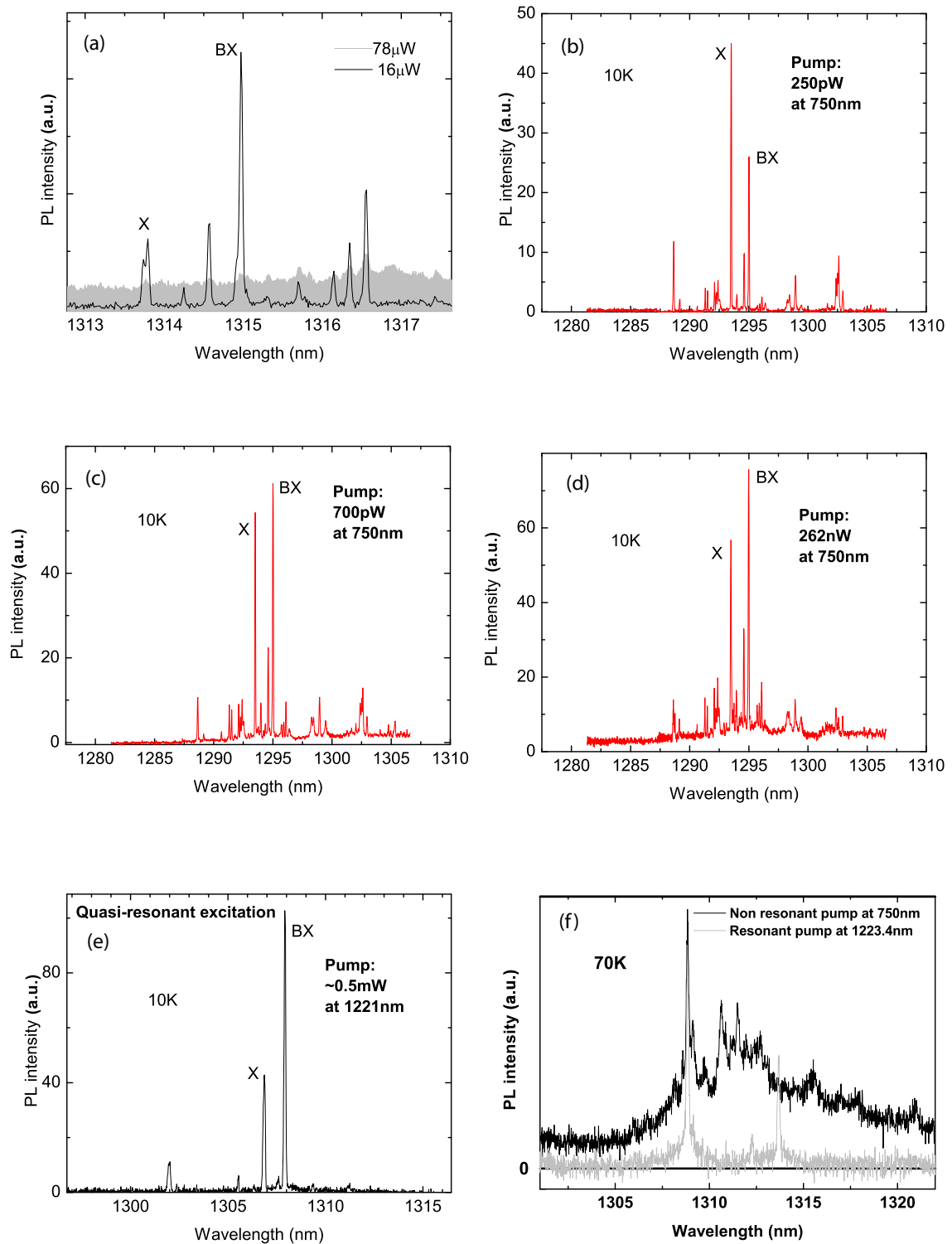
Figure 3.14: (a)Single QD PL under cw excitation at 835nm. (b,c,d) PL from single QD under pulsed excitaion at 750nm for different power densities. (e) Quasi resonant PL on single QD pumping in the excited state at 1221nm. (f) Comparison between resonant and non-resonant excitation at 70K.

of the GS. In Fig. 3.14(e) we present another QD pumped quasi-resonantly in the excited state: while it has similar PL intensity and a similar X to BX ratio as the QD in Fig. 3.14(d), it does not show the presence of any background emission. Similar results have been obtained before on smaller QDs([71]). The difference between the PL signals from the QD for different pump energies is amplified when we rise the temperature of the sample to 70K Fig. 3.14(f): while the signal from the non resonant excitation is dominated by a broad background with small narrow features, the PL resulting from the quasi-resonant pumping shows a remarkable recovery of the narrow exciton transitions. The quasi-resonant measurements reveal spectral lines with broadened bases which are the typical signature of the coupling between excitons and acoustic phonons [72, 73, 74]. This phonon broadened base cannot account for the background emission.

We further investigated the temporal dynamics of exciton transitions and background emission. In Fig. 3.15(a) we present the time evolution of the biexciton emission, spectrally isolated by a 0.8nm FWHM band-pass filter, for the same power densities as shown in Fig. 3.14(b,c,d): at low excitation intensity the time evolution of the PL shows the standard BX signature (section 3.4). As the pump power is increased to 750pW to saturate the BX emission, the delay in the decay of the PL increases to 1.5ns. A further increase in the excitation intensity by three order of magnitude further shifts the decay of the BX to 4ns exposing another decay developing on faster time scales (with a risetime limited by the resolution of the setup) at the same recombination energy of the BX. This new decay curve will be referred to as the broadband emission. The same behavior is observed on the X emission, the positive trion and on the ensemble of dots. There is a good correspondence between

the increase of the background emission in the integrated PL data (Fig. 3.14(b,c,d))
and the emergence of the broadband emission: we tentatively associate the broad-
band signal in the TRPL to the background emission in the PL. In Fig. 3.15(b) we
compare preliminary TRPL measurements made by pumping in the excited state the
unpaterned QD sample. The spectrum for the resonant excitation (inset Fig. 3.15b)
is characterized by a single exciton transition that dominates the spectra and a few
other weak narrow lines. Indeed we observe a significant difference between the rise
time of the two curves: due to the time scales involved it is not possible to attribute
the different rise times to the delay caused by the capture time of the carriers. The
delay in emission from the GS under non-resonant excitation has to be attributed
to another process. Finally we isolate the broad background emission by placing
a narrow band pass filter in a region of the spectrum where narrow transitions are
absent (inset Fig. 3.15c) and measure the TRPL at a pump power of 262nW: the
rise of the luminescence is limited by the setup resolution.

The TRPL measurements on the BX line Fig. 3.15(a) imply the existence of
a reservoir of carriers that can repopulate the QD. Evidence for the presence of
long lived carriers in the WL is found in the TRPL measurements made on the WL
PL signal (Fig. 3.15e) using a 40nm bandpass filter (Fig. 3.15d). The PL decay
is characterized by a double exponential decay of 0.3ns and 4.9ns, obtained after
deconvolution with the SRF. The fast component is tentatively attributed to the
recombination of the exciton, while the slower decaying part is tentatively attributed
to free carrier recombination. Szczytko et al.[75] measure and calculate the evolution
of the population of excitons and free carriers in a QW, and present evidence for of
long lived free carriers in the WL in agreement with our measurements. In the same

49
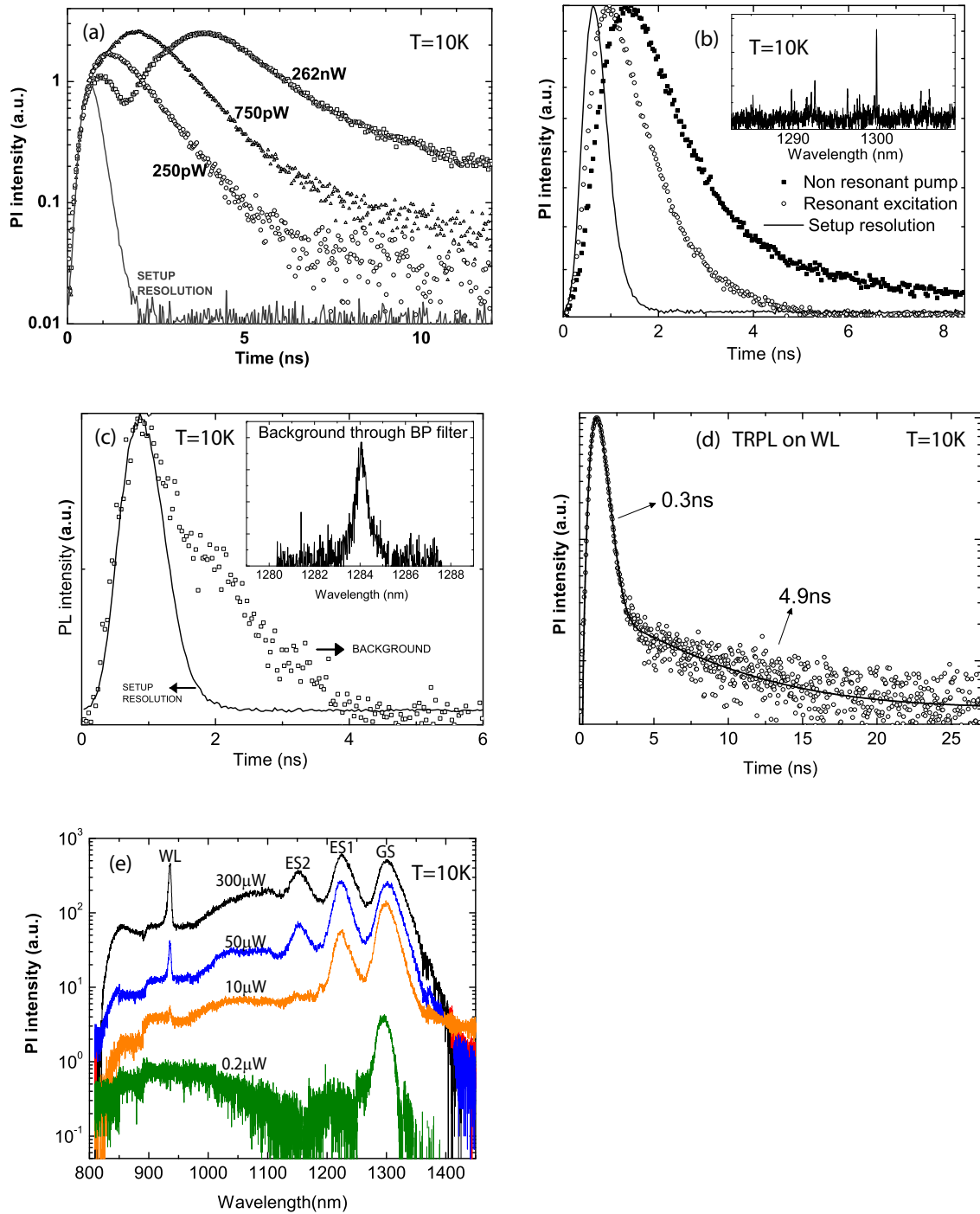
Figure 3.15: (a)TRPL for the same power densities as in Fig. 3.14b,c and d. (b) TRPL of ensemble of QDs for excitaion in the P state. (c) TRPL on background emission filtered through a narrow BP filter as shown in the inset. (d) TRPL on the WL measured with a 40nm FWHM bandpass filter. The solid line is the convolution between a two term exponential decay function and the SRF.(e) PL power dependence of an ensemble of dots including the WL under cw excitation.

work, the exciton formation process is explained through the coupling to optical photons. The formation rate evolves with plasma concentration and temperature affecting the probability of interaction with phonons. This explanation can be used to justify the presence of the PL signal from the WL only at relatively high power densities as compared to PL signal from the GS of the dots (Fig. 3.15e): at low powers the carrier capture, relaxation and recombination in the QD is more efficient that the exciton formation process in the WL.

Two conclusion can be drawn from the evidence presented: first, the background emission is coming from transitions between electron and holes in the GS of the QD since there is no other energy structure in the system that can emit at this wavelength. Second, the presence of carriers in the surrounding of the QD are a playing a role in the uncorrelated broadband emission. The non-resonant TRPL measurements suggest that the emission from the GS, at high power densities, is characterized by distinct phases. In an initial phase, after the pump pulse, a large density of free carriers surrounding the QD is causing a featureless broadband multiphoton emission from the ground state. As the number of carriers in the wetting layer is reduced, by radiative, non-radiative recombination and repopulation of the dot, we observe the expected decay from the undisturbed exciton transitions in the QD. This picture is confirmed by the steady state carrier populations obtained under cw excitation: at high power intensities only a featureless and broad signal is measured in the PL spectrum Fig. 3.14(a). As the power is reduced fewer carriers are interacting with the excitons in the QD and we see a mixture of both narrow transitions and broad background.

It is interesting to investigate the carrier dynamics that are required to give

Figure 3.16: Fit to the TRPL data at 262nW. On the right side: a schematic of the model with the fitting parameters.

origin to the unusual time-dependent PL signature measured on our QDs. We chose to represent the energy of the system, after the laser pulse, with n-excitonic levels which undergo cascade emission. The model consists of 5 multi-excitonic states and the BX state schematically represented in Fig. 3.16. There is no specific reasoning behind the choice of the number of levels, the system could be well modeled by more levels and different recombination times. We have neglected the X transition since it does not influence the PL dynamics of the higher laying levels. The following system of equations was used:

$$\frac{dP_n}{t_n} = -\frac{P_n}{t_n} + \frac{P_{n+1}}{t_{n+1}} \longrightarrow 1 \leq n \leq 5 \tag{3.3}$$

and for the last level (n=6):

$$\frac{dP_n}{t_n} = -\frac{P_6}{t_6} \tag{3.4}$$

Where P_n is the population probability of the energy level n and t_n is the radiative

52

lifetime. The broadband emission (**B**) measured in the TRPL data emerging at high powers and shifting the BX emission to longer time delays is given by the sum over the steady state solutions for the levels above the BX:

$$\mathbf{B} = \sum_{n=2}^{6} \frac{P_n}{t_n} \tag{3.5}$$

In the initial condition the system is in it's highest energy state ($P_6 = 1$ and $P_{n<6} = 0$), corresponding to the instant when carriers are excited in the bulk by the laser pulse. We then let the carrier populations evolve through cascade emission down to the lowest level. The change in excitation intensity is simulated by removing energy levels. The level at n=1 corresponds the QD dot populated by the BX, with a radiative lifetime of 1ns. To simulate the effect of the BP filter on the collected intensity we reduce by a factor of $I_\mathbf{B}/I_{BX}$ the broadband emission: an initial guess of this factor was obtained from comparing the narrow BX transition to the broadband emission and taking into account the profile of the band pass filter. Fig. 3.16 shows the fit made to the experimental data obtained for an excitation of 262nW on the BX and on the background, using values of τ shown in the diagram of Fig. 3.16. The model fits the data to a good accuracy except for long time delays. We note that we can simultaneously fit the broadband emission (measured at the same power density Fig. 3.15(c)) and the filtered TRPL signal from the BX emission, only the intensity of the measurements have been scaled. At lower excitation densities (Fig. 3.17) the model is reduced to a three level system and the characteristic rise time is well described by the model. A better fit could be achieved with a higher number of energy levels to increase the resolution of the model, but more experimental data is required to help in the non-trivial task of refining the values of the fitting parameters.
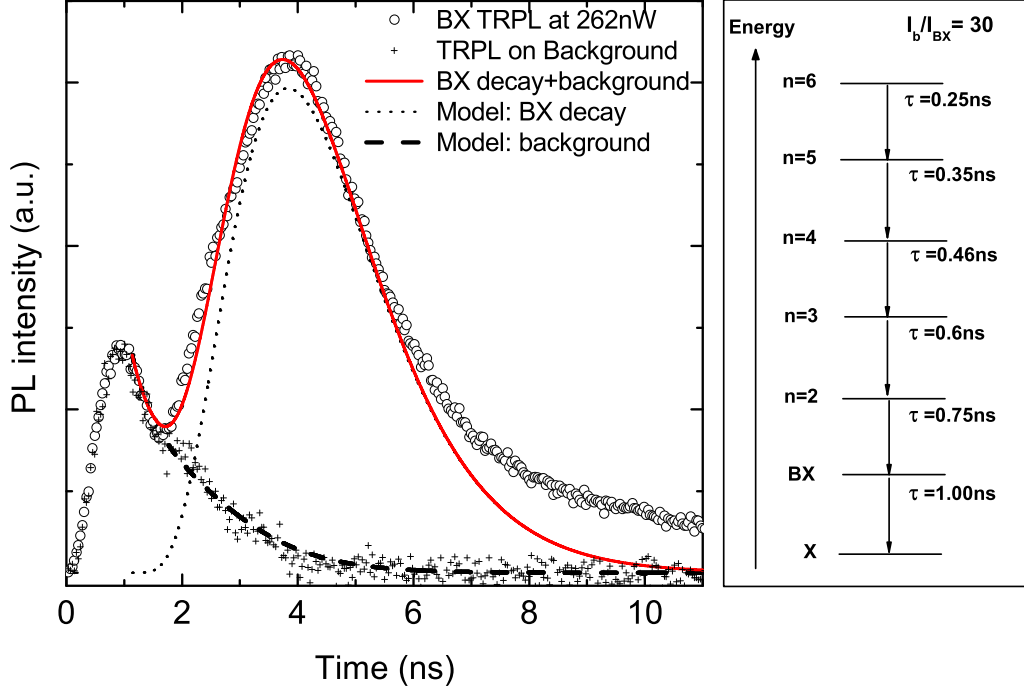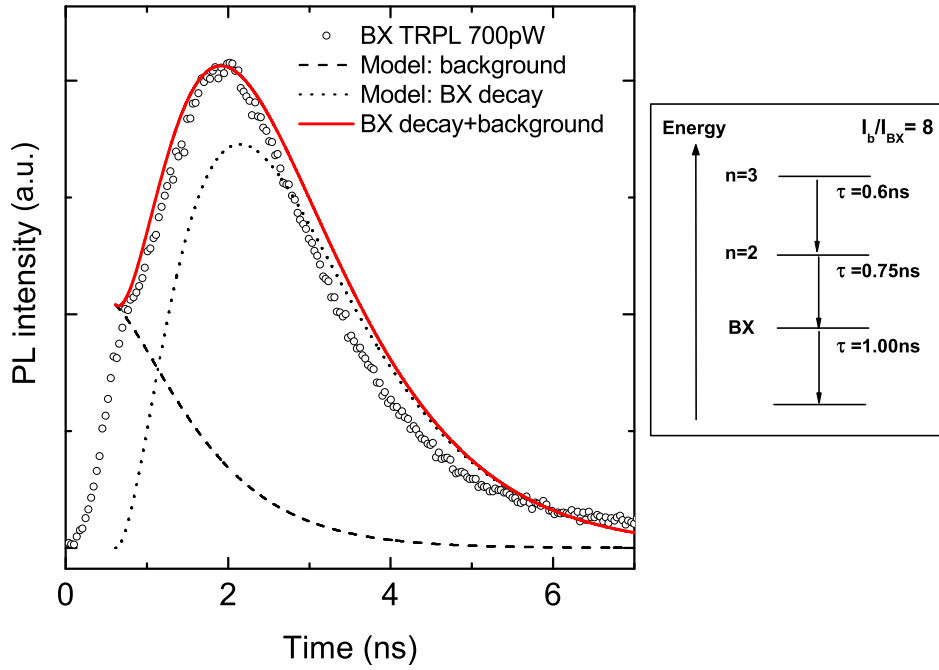
Figure 3.17: Fit to the TRPL data at 700pW. On the right side: a schematic of the model with the fitting parameters.

In agreement with the interpretation of the experimental data made above, the model suggests that for each laser pump pulse several excitons are recombining in the GS of the QD: the GS is being fed by a reservoir of charges which modifies the radiative lifetime and emission energy. A dedicated series of PL and TRPL measurements are required to establish the correlation between the emission from the ground state of the QD and the WL under the same excitation conditions. To gain further insight into the origins of the interaction on the carriers confined in the QD, it would be interesting to measure the PLE to investigate the onset of the continuum in these deeply confined QDs.

This model was developed independently without the knowledge of the existence of similar work [76] used to give a quantitative explanation of a BX sideband in shallow QDs.

Chapter 4

Counting single photons

In Chapter 3 we showed that we are able to isolate a single X transition and measure the time evolution of the photoluminescence. In this Chapter we measure the light statistics from this transition and show that the QDs can emit single photons under pulsed and cw excitation. We provide an analysis of the setup efficiency and suggest ways of improving the efficiency to make the devices suitable for QKD applications. Finally we measure the second order correlation function on the emission from the single exciton transitions under quasi-resonant excitation using novel detectors based on superconducting nanowires.

4.1 Measurement of $g^{(2)}(0)$

The standard technology used for single photon detection at telecom wavelength is based on InGaAs APDs. Due to the high noise levels and low QEs these detectors must be operated in Geiger mode, i.e. the APD is biased above avalanche to achieve single photon sensitivity for short times, of the order of a few nanoseconds. As a consequence a measurement of the $g^{(2)}(\tau)$ is not possible since it requires photon correlations spanning the lifetime of the two level system. For this reason we excite the QD with laser pulses at a well defined repetition rate and synchronize the opening of the gate on the APDs with the expected arrival time of the photons. For an application to QKD this operation mode does not present a limitation

since synchronization is required between parties. In these conditions the intensity correlation function is defined as [77]:

$$g^{(2)}[i] = \frac{\langle C_2[i]C_1[i] \rangle}{\langle C_2 \rangle \langle C_1 \rangle} \tag{4.1}$$

where C_1 and C_2 are the counts recorded on the detectors for pulse [i]. A plot of this function (Fig. 4.5) is characterized by a series of peaks separated by the repetition period of the laser: the peaks at $i \neq 0$ correspond to events when photons are detected from two different pulses while the central peak at i = 0 corresponds to events where two photons are detected from the same pulse. This measurement technique is useful only for obtaining a value for the $g^{(2)}(0)$. The number of coincidences (C_C) in each peak are:

$$C_C = C_{R1} * C_{R2} * T * P, \tag{4.2}$$

where $C_{R1,2}$ is the count rate recorded on each detector, T is the integration time and P the laser repetition period. For a coherent source all peaks have the same area, while for a single photon source the central peak goes to zero. In this discussion we are assuming that the source properties are periodic, so that all expectation values are unchanged when the pulse number index is shifted. In characterizing a single photon source, it is evident from equation [4.1] that any uncorrelated event that produces a count on the detector will contribute to the $g^{(2)}(\tau = 0)$ and if the uncorrelated events are a significant part of the total events, it will not be possible to correctly characterize the light statistics of the source. To quantify the influence of uncorrelated noise on the measured $g_m^{(2)}(0)$ we can write the correlation function taking into account the noise $N_{1,2}$ at each detector [30]:

$$g_m^{(2)}(0) = \frac{\langle C_1C_2 + N_1C_2 + C_1N_2 + N_1N_2 \rangle}{\langle C + N \rangle^2} \tag{4.3}$$
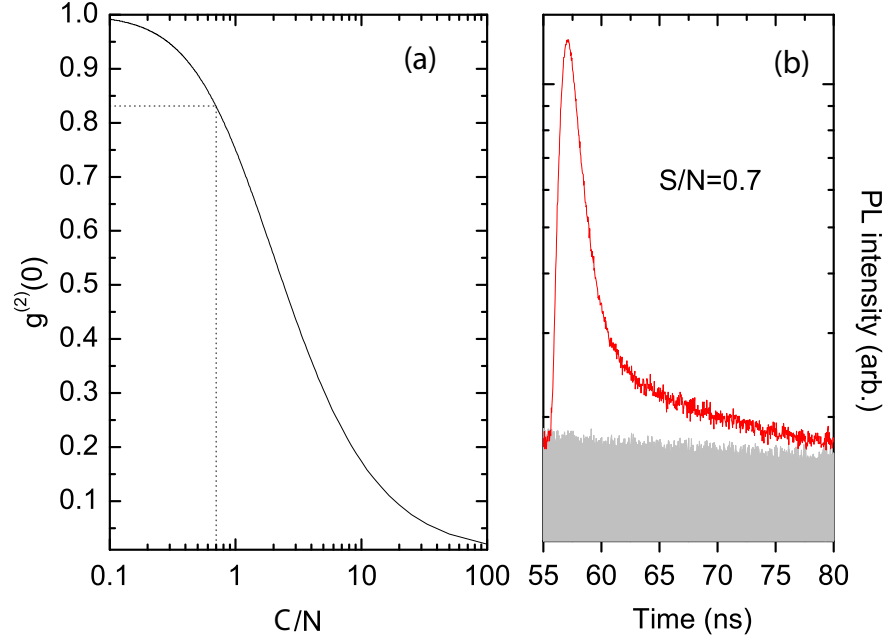
56

Figure 4.1: *(a) Intensity correlation function at t=0 as a function of SNR. (b) Time resolved PL measurement on the X transition.*

which can be simplified to give:

$$g_m^{(2)}(0) = 1 + \rho^2 g^{(2)}(0) - \rho^2 \tag{4.4}$$

where: $\rho = \frac{C}{C+N}$ for $C_1 = C_2$ and $N_1 = N_2$. The simulation of the $g^{(2)}$ (eqn. 4.4)

calculated for a perfect single photon source in the presence of uncorrelated noise is

plotted in figure 4.1a as a function of the ratio C/N. In figure 4.1b we show the

raw data obtained for the lifetime measurement on the X line: from this plot we

can estimate the C/N ratio by comparing the grey area (noise) and the signal from

the exciton to be approximately equal to 0.7 which gives a $g^{(2)}(0) = 0.83$.

This is the minimum value we could ever hope to measure from a perfect single

photon source. The signal in the TRPL measurements is already optimized as

discussed in the previous chapters: the QDs are embedded in a planar micro-cavity

to optimize the extraction efficiency into the objective, a narrow BP filter is used to

isolate the single X transition and the sample is kept at low temperature. The only possibility of demonstrating single photon emission is to reduce the detector dark counts.

4.1.1   The APD

An APD is affected by two sources of noise, dark noise and afterpulsing. Dark noise is due to the thermal excitation of electrons in the ionization region. The dark noise is reduced by adjusting the temperature and the reverse bias, which reduce also the QE. Afterpulsing is due to the trapping of electrons during an avalanche in defect levels in the ionization area of the APD. The trapped charges trigger an avalanche during the next gate. An easy way to reduce the afterpulsing is to use a dead time longer than the lifetime of the trapped carriers, which is of the order of several microseconds. For the APD we define a dark count probability (DCP) per gate, which can be calculated from:

$$DCP = \frac{No.OfDarkCountsPerSecond}{TotalOpenTime} \qquad (4.5)$$

where: Total Open Time = No Of Gates In One Second * Gate Length.

The APDs used in our experiments are operated at an optimized temperature and the reverse bias is adjusted so that for the predefined nominal gate length (2.5, 5, 20, 50 and 100ns) the QE is 10%. It is important to note that for these detectors there is a difference between the nominal gate and the optical gate. The optical gate is the actual time during which the APD is optically sensitive, while the nominal gate is the time during which the reverse bias is applied. To measure the optical gate the detector is arranged in a set-up similar to the one used in time-resolved

PL measurements (section 2.2), except that the optical input is illuminated by a cw source. The remarkable difference between the nominal gate width and optical gate width is shown in Fig. 4.2 for the settings used in the single photon correlation experiments. It is important to be aware of the difference for two reasons:

a - A measurement of the DCP requires normalization to the optical gate width and,

b - The APD optical gate duration must be tuned to the X lifetime to optimize the ratio C/N.
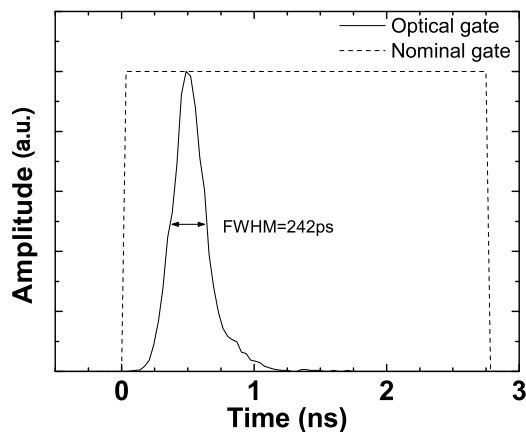
Figure 4.2: *Comparison between optical gate and nominal gate on the idQ200.*

Figure 4.3a shows the DCP as a function of the gate width: below a nominal gate width of 5ns the DCP drops down by an order of magnitude. Although the optical gate width is significantly smaller than the X lifetime (Fig. 4.2), by fine tuning the duration of the gate (Fig. 4.3b) we obtain a C/N ratio of 10 which is acceptable for characterizing single photon sources. It turns out that the optimal optical gate width ($\sim$300ps) corresponds to a nominal gate of about 2.8ns which is close to a standard setting in the APD for which the bias voltage is tuned to give a QE of 10%. This reduction of DCP for short gates is not understood and it is not

repeatable from chip to chip.

Figure 4.3: *(a) Measured values of DCP as a function of gate width. (b) Optimization of the gate width to obtain the highest C/N on the X emission.*

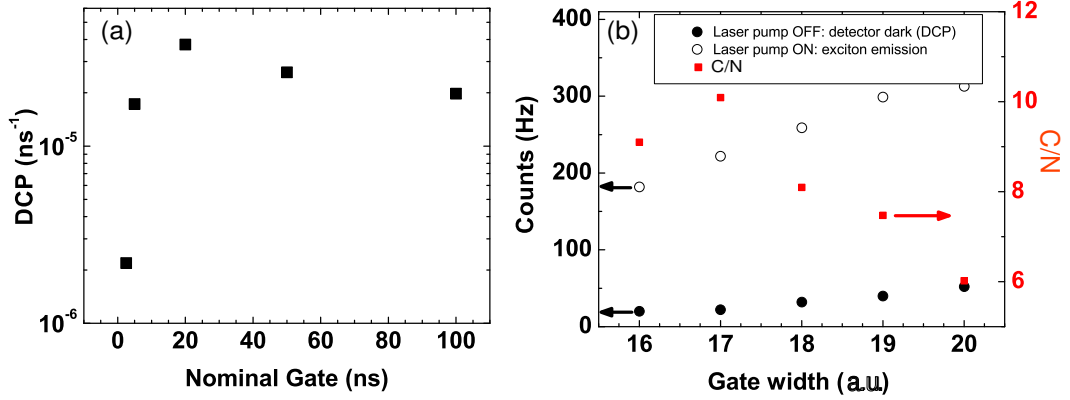A source of correlated noise to be aware of is the cross talk between the detectors. When an avalanche is triggered in the APD, a burst of electromagnetic radiation is emitted with a spectral range overlapping the APD response curve. We tested this in the setup in Fig. 4.4(a) where we connect the optical input of APD1 (acting as the source of the em radiation) to the optical input of APD2 (acting as the detector of the em radiation emitted by detector1) via an optical fiber. The delay can be set to 0ns or 50ns. When the delay is 50ns the gate on detector 2 is synchronized with the arrival time of the photons emitted from detector1 and the average count rate is about 530Hz (Fig. 4.4(b)). When the delay is 0ns the detector 2 opens too soon to detect the light signal emitted from detector 1 and we measure the dark counts of detector 2 (480Hz). In Fig. 4.4(b) we show the counts on detector 2 while the delay is switched repeatedly from 0 to 50ns: there is a clear correlation between the delay and the count rate, demonstrating that an avalanche in the APD generates a burst of em radiation that can interfere with single photon measurements. The antibunching measurements should not be affected by the APD optical

60

emissions since the detectors are operated simultaneously at a repetition period of 250ns and the optical delay between the detectors is 10ns.
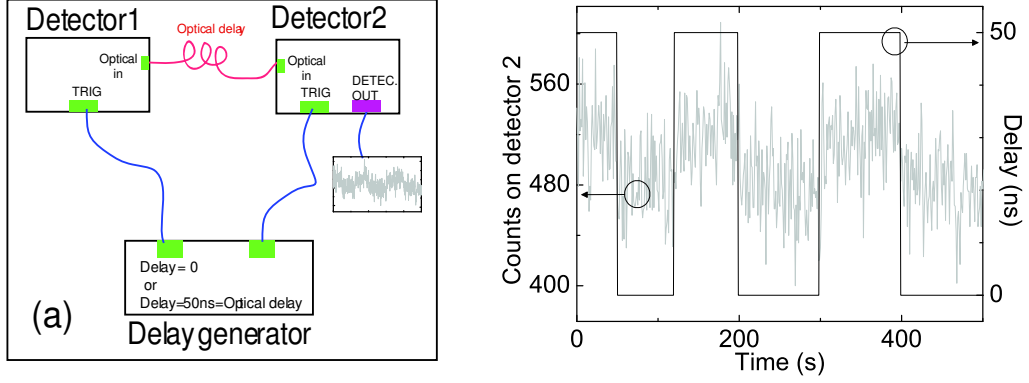
Figure 4.4: *(a) Setup for measuring the APD emission. (b) Correlation between delay and counts on detector 2.*

4.1.2 Results

The correlation setup described in section 2.3 is used to measure the intensity correlation function at zero time delay for a single exciton transition selected by the 0.8nm band-pass filter. The results are show in fig. 4.5 for increasing power densities and a summary of the experimental parameters are reported in table 4.1. For calculating the suppression of multiphoton probability the counts in the time bins at $t \neq 0$ must be normalized using equation 4.2. For each measurement the calculated number of coincidences (using eqn. 4.2) is in agreement with the average number of correlations in time bins at t$\neq$0. Moreover the standard deviation is close to the square root of the average which indicates that the fluctuations in the bins are random. The measured $g_m^{(2)}(0)$ decreases from 1 at a pump power of 350nW to 0.38 at 0.6nW, then increases again for a pump of 0.4nW. The fact that the $g^{(2)}(0)$

Figure 4.5: *Antibunching measurements for increasing excitation power.*
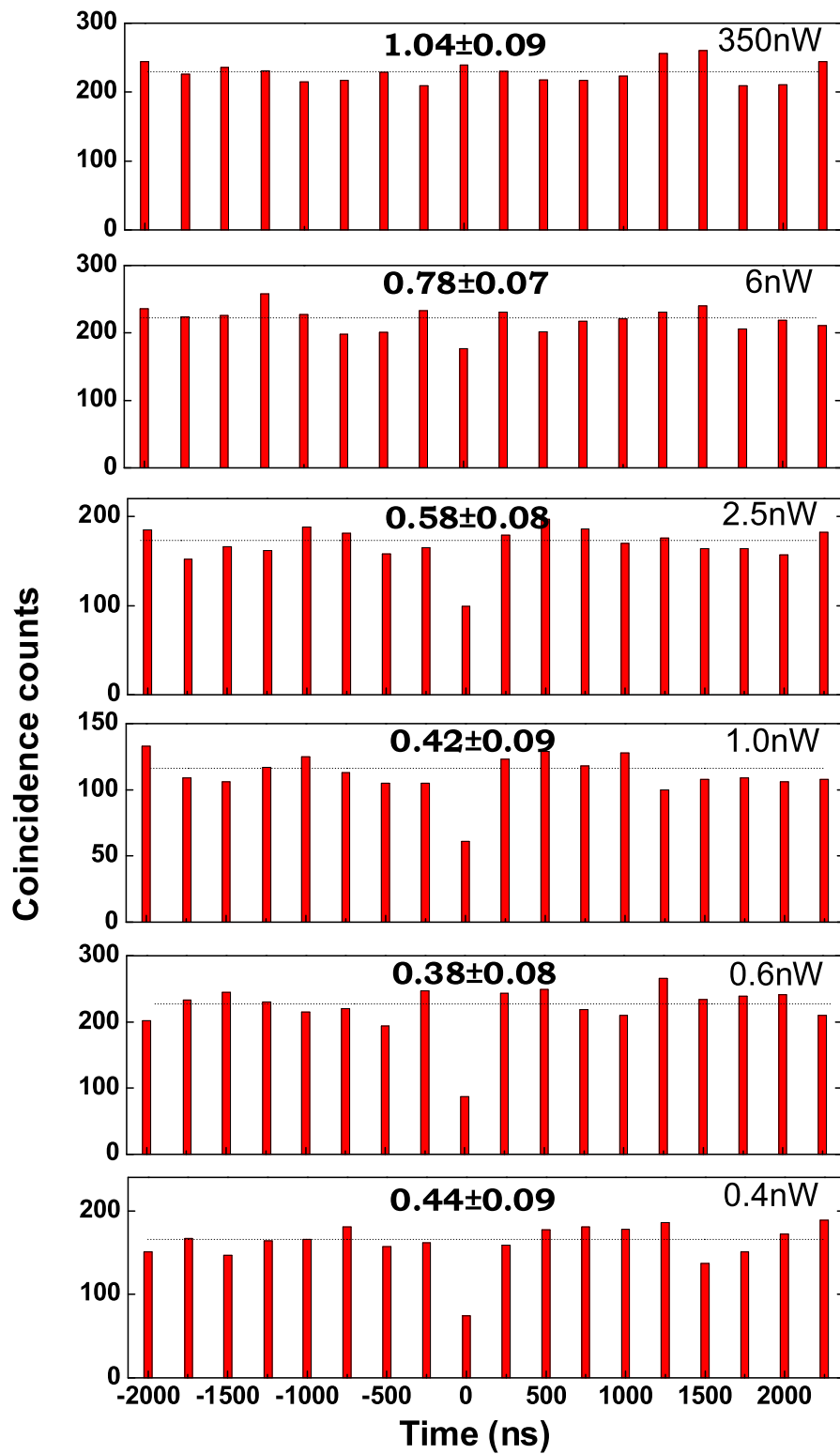
goes below 0.5 implies that the device is emitting less than two photons per pulse.

While the detector dark counts (N_D) can be easily measured by switching the pump laser off, it is more difficult to get an estimate and to establish the origin of uncorrelated counts (N_U) during a measurement. There are two types of uncorrelated events: those due to the detection of an uncorrelated signal from the QD emitted together with the single photon signal and those due to imperfections in the setup such as detector afterpulsing and stray light. Assuming that the intensity of the uncorrelated light from the QD is power dependent, as the reduction of the $g_m^{(2)}(0)$ implies, it is possible to get an estimate of the detection events generated through the power dependence of the $g_m^{(2)}(0)$. In table 4.1 are shown the measured values of $g_m^{(2)}(0)$ for the different pump powers and in column SNR_m the calculated values of the ratio of single photons to the total noise $N_D + N_U$ (using equation 4.4) required to give the measured $g_m^{(2)}(0)$. The total count rate measured on the single photon detector during an experiment can be expressed as a sum of there components:

1 - detector dark counts N_D; detector counts due to thermal excitation of charges in the ionization region during a gate. Can be measured by switching the pump laser off.

2 - uncorrelated noise N_U: the number of clicks per second due to uncorrelated events which are not included in the detector dark counts N_D;

3 - photon counts C: number of clicks per second due to detection of single photons. During an experiment the count rate measured on the detector is the sum of the three terms mentioned above. The quantity $C + N_U = S$ can easily be deducted by measuring the detector dark counts(N_D): in the analysis that follows we sepa-

63

rate the uncorrelated noise (N_U) from the single photon counts (C) and calculate

the values of the power dependent and constant components that contribute to the

value of the uncorrelated noise (N_U). The SNR_m can be expressed as:

$$SNR_m = \frac{C}{N_D + N_U} = \frac{S - N_U}{N_D + N_U} \tag{4.6}$$

where all the quantities are known from the experiment, except for N_U. Note that

the sum $C + N_U$ has the same power dependence as the exciton integrated PL

intensity measured (chapter 3) on similar QDs (fig. 4.6). Solving for N_U gives:

$$N_U = \frac{S - N_D * SNR_m}{1 + SNR_m}. \tag{4.7}$$

The calculated values for N_U and C are reported in table 4.1.

Table 4.1: Antibunching data. The reported values are: S=C+N_U, N_D: detector dark counts, C: single photon counts, N_U: uncorrelated counts, $g_m^{(2)}(0)$: calculated from raw correlation data, SNR_m: required SNR to give $g_m^{(2)}(0)$, $g^{(2)}(0)$: calculated after noise ($N_D + N_{CB}$) subtraction.

Power [nW]	Int.Time [hrs]	S [Hz]	N_D [Hz]	$g_m^{(2)}(0)$	SNRm	N_U [Hz]	C [Hz]	$g^{(2)}(0)$
6	0.6	602	33	0.78	0.88	305	297	0.75
2.5	0.6	537	33	0.58	1.85	107	370	0.45
1	0.5	397	33	0.42	3.21	69	327	0.41
0.6	2	30.7	33	0.38	3.7	39	268	0.09
0.4	2	227	33	0.44	2.94	33	194	0.19

As the excitation power is reduced the photon counts (C) decrease and the

uncorrelated noise N_U decrease too but with a different rate as revealed by the ratio

C/N_U fig. 4.7(a). It is this ratio that determines the trend of the correlation function:

the $g^{(2)}(0)$ decreases because of an improvement in the SNR due to a reduction of

the uncorrelated photon emissions at lower powers, below 0.6nW the uncorrelated

photon emission does not reduce any further, in contrast to the PL signal, revealing

a constant background of 33Hz (N_{CB}). The different contributions of the noise are plotted in Fig. 4.7b: the noise N_U can be separated into two components: a constant background (gray area) and a power dependent component (grid patterned area).

Contributions to the power dependent part of N_U are mainly dominated by
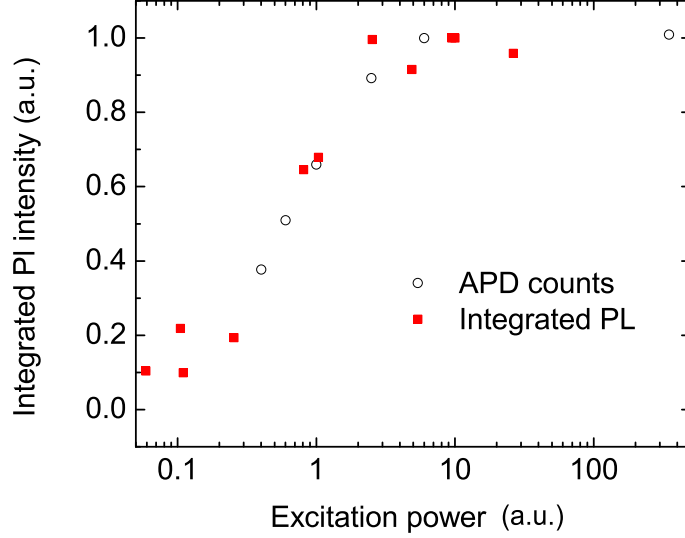
Figure 4.6: *Integrated PL measured on the APD and on the InGaAS array.*

uncorrelated light from the QD due to interactions with the carriers surrounding the QD. A discussion on the QD background emission was presented in section (3.5). A small contribution to the power dependent noise is given by: multiphoton emissions due to repopulation of the X state (laser line width is about 5% of the X lifetime) and afterpulsing events due to the increase in count rates. The increase in afterpulsing is very small since there is no change in the PL intensity dependence on power when compared to PL integrated measurements made with the InGaAs array detector (fig. 4.6).

Finally we can calculate the 'true' values of $g^{(2)}(0)$ that characterizes our source. The signal originating from the single QD device is given by $S_D = C + N_U - N_{CB}$, while the noise from the experimental setup is: $N_S = N_D + N_{CB}$. Since

Figure 4.7: *(a) SNR as a function of excitation power. (b) Breakdown of the components that add-up to make the signal measured during antibunching experiments.*
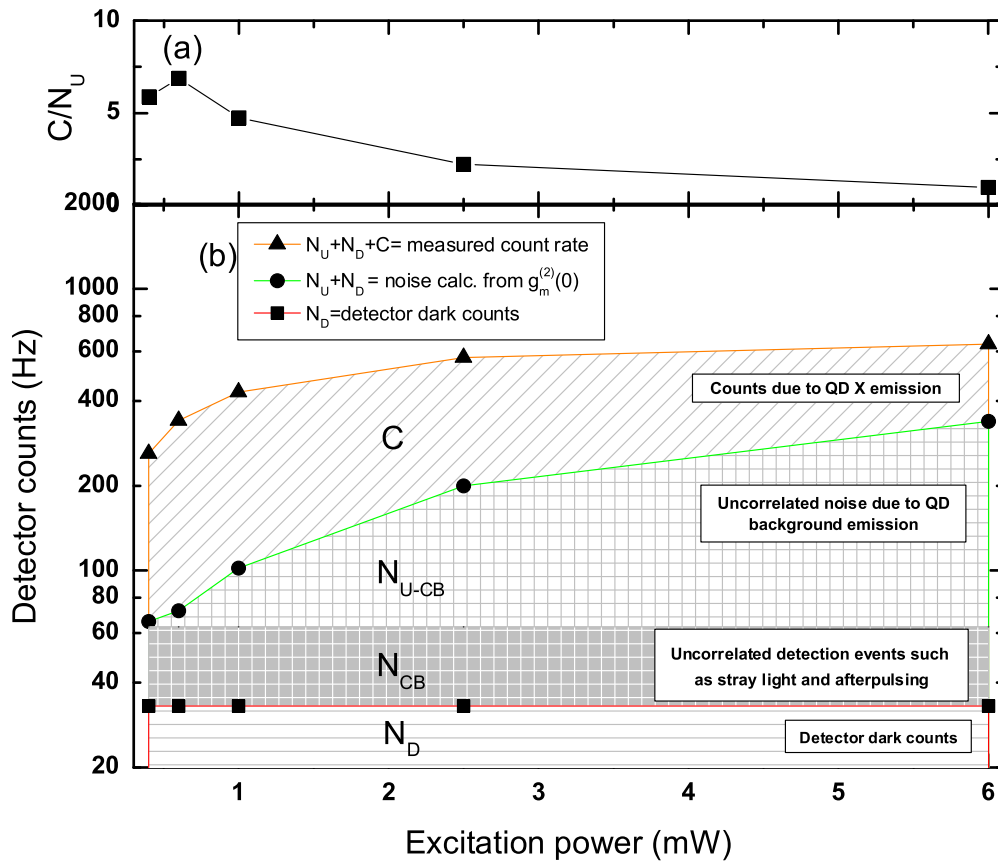
the difference between the detector counts is small we can assume that the bright and dark events are the same for each detector hence the number of coincidences contributed by the noise is (from eqn. 4.2): $2 * S_D + N_S^2 * T * P$. Subtracting these values from the raw coincidence counts we get the $g^{(2)}(0)$ values reported in table 4.2: a minimum of 0.09 is reached which fulfills the requirements for a single photon source for QKD applications [78].

4.1.3 Single photon efficiency

Having established that the QD embedded in the planar microcavity emits single photon states, the next step is to examine the single photon efficiency since it has a direct impact on the security of a quantum transmission. During a QKD session the two parties detect the presence of an eavesdropper by counting the number of errors in the bit sequence. The problem is that discrepancies between the exchanged keys also happen because of experimental imperfections. The QBER is defined as:

$$QBER = \frac{NoOfWrongBits}{TotalNoOfBits}. \tag{4.8}$$

In a practical QKD system many factors contribute to the QBER [10], here we consider only the contributions from the dark count rate of the detectors used in our experiment and the resulting error rate from the single photon efficiency:

$$QBER = \frac{DarkCounts/2}{DarkCounts + PhotonCounts} = \frac{(N_D + N_{CB})/2}{N_D + N_U + C} = \frac{(33 + 33)/2}{33 + 39 + 268} = 0.1, \tag{4.9}$$

The QBER security limit is 11% [79] which is just satisfied by our system: realistic implementation of the single QD device for fiber based QKD requires at least an or-

der of magnitude decrease in the QBER since losses are to be expected in the optical circuits used for processing the qbits and from the attenuation in the fiber optic link. Improvements in the detectors SNR and optimization of the single photon efficiency at the fiber output are required. During this thesis the SNR of the APDs has been pushed to the limit (section 4.1.1), an improvement of an order of magnitude is not to be expected from this technology. New single photon detection technology based on superconducting nanowires promise orders of magnitude improvement in SNR over the APDs. In section 4.2.2 of this chapter we investigate the properties of a prototype device based on these detectors.

An analysis of the optical losses in our system is presented in the following. In Fig. 4.8 we present a schematic of the optical setup used in the single photon correlation measurements with the transmission efficiency for each stage in the optical circuit. There are two stages, each of which introduces an order of magnitude loss in the optical signal: the coupling to the single mode fiber and the light extraction from the QD. To assess the the coupling efficiency to the optical fiber we set an upper limit of 4dB by measuring the coupling efficiency between two SMFs and a lower limit of 10dB by comparing the PL intensity from the ensemble of QDs collected by the objective and dispersed into the spectrometer, and the intensity measured by coupling the signal from objective into the SMF fiber and back to free space into the spectrometer. The actual single QD coupling efficiency can never be lower since the image of the fiber on the sample is smaller than the laser spot. From the planar cavity design the extraction efficiency of the QD spontaneous emission into the NA of the objective was calculated to be 9%. This figure is confirmed by the thirteen-fold increase in PL intensity from single QDs in the microcavity as compared to the
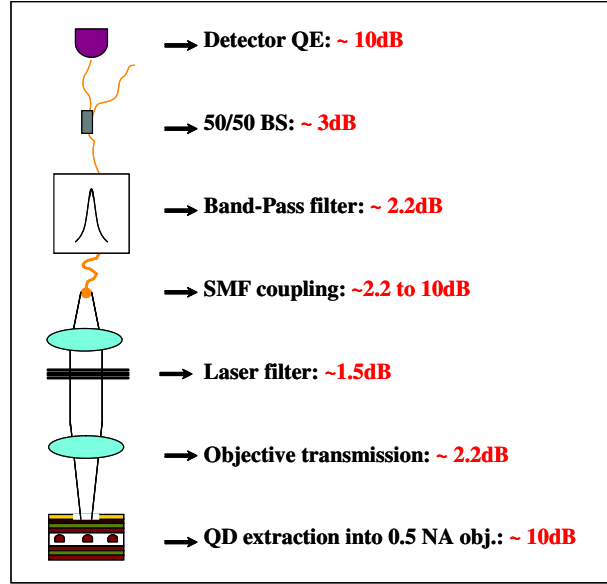
Figure 4.8: Schematic of antibunching setup with the optical efficiency for each component.

intensity from QDs in bulk GaAs (Fig. 3.1b). The calculated extraction efficiency in bulk GaAs into the objective NA is 0.55%. The total estimated setup efficiency adds up to 38.9dB (for a SMF coupling efficiency of 10dB), a further 0.5dB has to be added since single photon emission is obtained below the saturation of the X transition, as shown in Fig. 4.7. The total estimated efficiency compares well with the measured efficiency of 41.6dB obtained by taking into account only the emission from the sample ($C+N_U$-$N_C B$=274Hz (see table 4.1) at a repetition rate of 4MHz) and assuming that for every laser pulse the QD emits a photon in the microcavity. Similar correlation experiments made on single quantum dots by other groups [6, 5] using fiber-coupled APDs measure efficiencies similar to ours. Anticorrelation measurements on QDs emitting below 1000nm report efficiencies between 30dB and 40dB [80, 81, 82, 16, 83]. In planar micro cavities there is no in plane confinement so most of the SE from the QD is guided in the plane of the cavity and lost in the leaky modes propagating in the DBR beyond the stop-band: only a small fraction

(14% in our case) is coupled to air, of which 9% is collected by the objective. Small diameter micropillars, on the contrary, can achieve very high extraction efficiencies into air, up to 70% has been predicted [35], through careful optimization of the mode density around the emitter (Purcell effect [23]). But as the pillar diameter is reduced, to achieve higher Purcell factors, the funneled photons in the extracted mode are lost because the divergence of the mode is not compatible with the NA of the collection optics. It would appear that a significant increase of the collection efficiency could be obtained by combining the Purcell effect in microcavities with a careful design of the far-field, to mach the numerical aperture of a SMF directly coupled to the cavity to avoid the loss in the objective and focussing in the fiber [84]. But in the realization of such a device one will run into the following setback problems: first the technological complexity involved is mindboggling, and second for a large micropillar, required for compatibility with the spatial mode of the fiber, it is difficult to isolate a single QD in the antinode of the field to achieve a high device yield.

4.2   Measurement of $g^{(2)}(\tau)$

While the measurement of $g^{(2)}(0)$ is important for the characterization of the light statistics for single photon emitters, many important physical properties of the system are hidden in the correlation function $g^{(2)}(\tau)$ for any delay [85, 60, 80]. The measurement of the $g^{(2)}(\tau)$ with APDs is exceedingly difficult since the use of relatively long ($> 10ns$) gates would drive the experimental C/N ratio below unity. The recent development of single-photon detectors based on NbN superconducting nanostructures [86], promise orders-of-magnitude improvement over InGaAs APDs

in sensitivity, dark count, jitter and repetition frequency. This is why this new technology is attracting a lot of attention in the single photon and QKD community. In collaboration with the authors in ref. [86], who provided the detectors, we measured the correlation function on the single states produced by our QDs.

4.2.1 The SSPD

The detection principle of the SSPDs is based on the local inhibition of superconductivity in a current-biased ultra-thin superconducting nanowire due to the absorption of a light quantum [87]. The detection principle is illustrated in Fig. 4.9: as
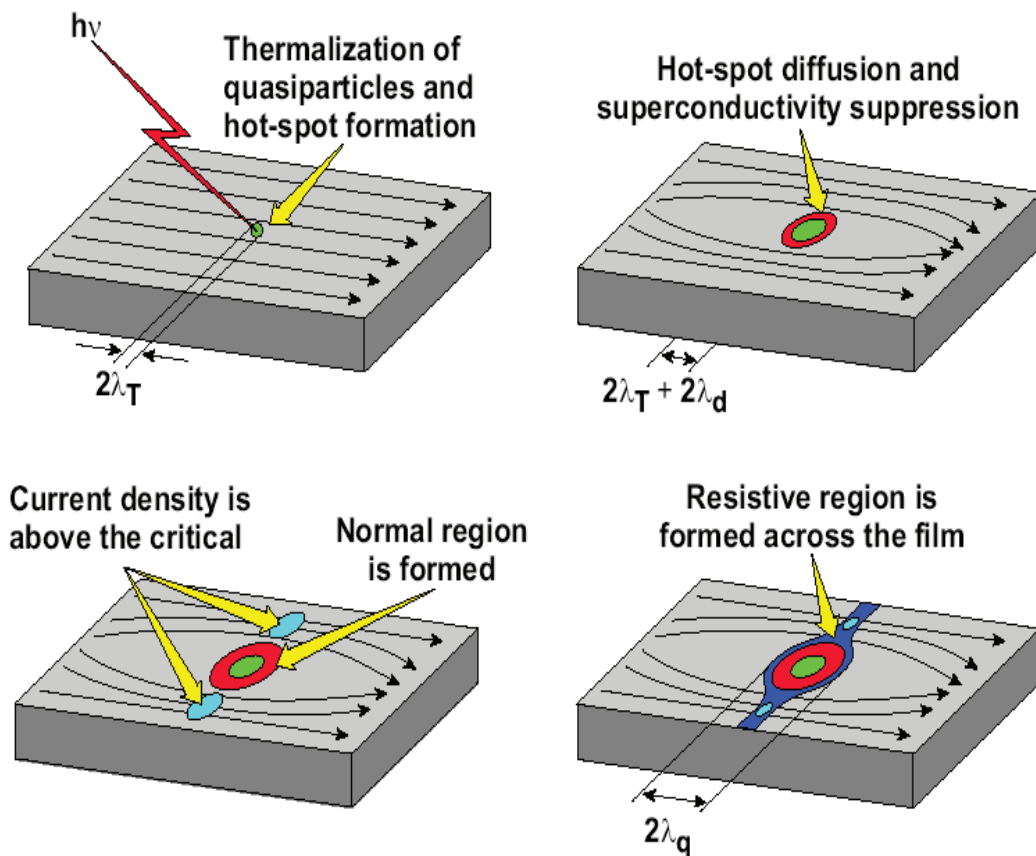

Figure 4.9: Detection principle of SSPDs.

the superconducting energy gap is about 2meV for NbN, an absorbed near-infrared

photon supplies a sufficient amount of energy to split a Cooper pair and promote an electron to a highly excited state. During the relaxation process secondary carriers are efficiently generated and the local electron effective temperature exceeds the superconducting critical temperature, thus creating a 'hot spot'. As the super-current avoids the hot spot and accumulates towards the edge of the nanowire, the critical current density may be reached inducing a transition to a resistive state and a subsequent pulse in the external circuit.
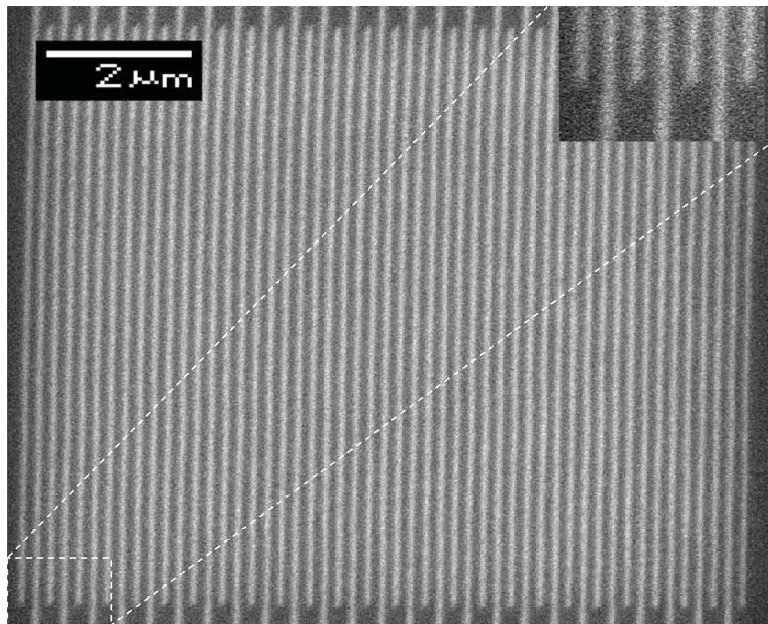
Figure 4.10: SEM image of the $10x10\mu m^2$ NbN meander composed of 100nm wide and 3.5nm thick wires.

The SSPDs used in this work consist of $10x10\mu m^2$ meanders (Fig. 4.10) made of a 100nm wide, 3.5nm thick NbN nanowire. The fabrication technology is described in [88]. Two SSPD chips are mounted on a micromechanical support and aligned to a pair of single mode fibers, the system is then cooled down to 2.3K in a liquid He insert. Input fiber connectors and output SMA cables are mounted at room temperature on the flange of the cryogenic insert. The high frequency components

72

of the detector output are fed to a 60 dB-gain amplifier with a 2.5 GHz bandwidth.

The efficiency of the fiber coupled detector is measured using a gain-switched diode

laser at 1300nm and a calibrated InGaAs APD as a reference.   The dependence
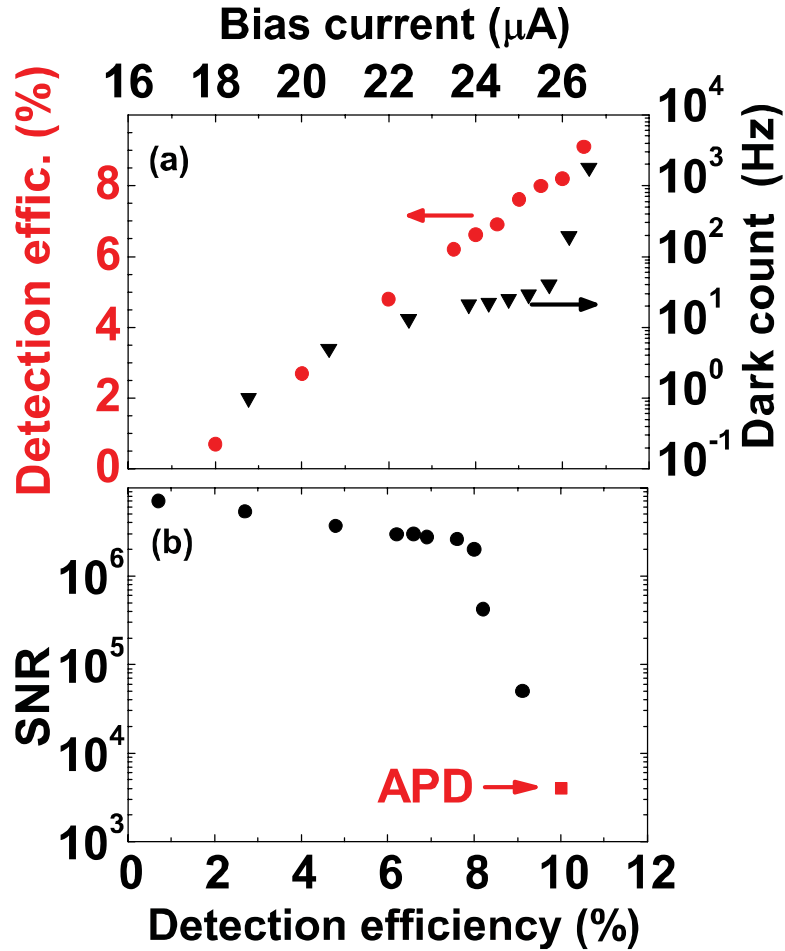
Figure 4.11: (a) SSPD detection efficiency and dark count rate plotted as a function
of bias current at 2.3K. (b) Comparison between SSPD and APD performance.

of the detection efficiency (DE) as a function of bias current is shown along with

the dark count rate (DCR) in Fig. 4.11 for the best SSPD. The DE for the SSPD

refers to the percentage of single-photon pulses coupled to the fiber that produce an

output signal. Both DE and dark counts increase with increasing bias current. At a

bias current of $I_B = 22\mu A$ an efficiency $DE = 4.8\%$ and dark count rate DCR=13Hz

are measured. The other SSPD had lower efficiency (2.5%) for the same DCR. The

corresponding DE/DCR ratios are over a factor of 10 higher than previous reports for fiber-coupled SSPDs [89, 90]. The tail in the DCR, measured below a bias current of $25\mu A$ (Fig. 4.11a), is attributed to the room temperature background radiation entering the system, which can be suppressed by a cold filter. A very attractive property of this detector is the low dark count rate. A quantification of the improvement of the SNR of the SSPDs as compared to APDs is difficult due to the very different operating regimes of the two detectors. Due to the gated operation mode of APDs, only a dark count probability (DCP) per gate can be defined, which is a function of the gate width. We define the SNR=DE/DCP as a figure of merit, where the DCP is measured for a gate width of 1ns. In Fig. 4.11b the SNR values for the SSPD are deduced from the data presented in Fig. 4.11a. For the APD: the DCP (for a 1ns gate) was extrapolated from the dark count rate (33Hz) measured during in a 300ps optical active window and at a repetition frequency of 4MHz. These values correspond to the optimized working regime used for antibunching measurements presented in the previous section. The SSPD displays several orders of magnitude improvement in the SNRs.

The SSPDs also provide improved temporal resolution: Fig. 4.12 reports the temporal dynamics of a laser diode pulse as measured directly using a sampling oscilloscope and by TCSPC using the SSPD and the APD. From the jitter characteristics of the correlation card, we estimate the time resolution of the SSPD and APD at 150ps and 400ps respectively. Lower jitter values (18ps have been reported [91]) could be achieved by improving the amplification electronics. We note that the SSPD response follows a Gaussian distribution, while the APD presents an asymmetric profile, which depends on the count rate and limits their application for

74
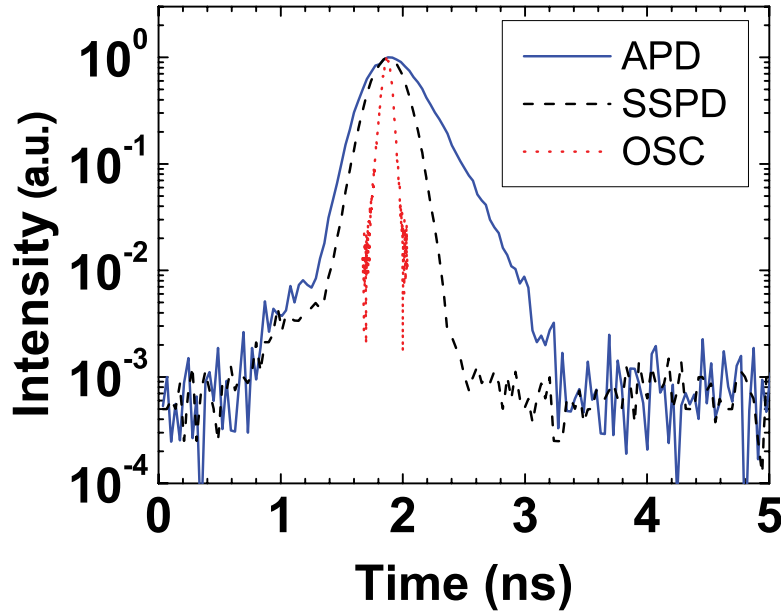
Figure 4.12: Measurement of the jitter of the detectors. Dotted line: laser pulse (FWHM=88ps) measured on a sampling oscilloscope (OSC) with 24GHz bandwidth. Continuous line: temporal response of the APD (FWHM=480ps). Dashed line: temporal response of the SSPD (FWHM=320ps).

TCSPC experiments.

4.2.2   Results with SSPDs

Although the SSPDs present a very attractive alternative to APDs the operational complexity of the detector is high. Difficulties arise from two causes: the prototype packaging and the high sensitivity. While the meander alignment to the optical fiber is stable, the electrical contact to the detector deteriorates quickly as the system goes through each thermal cycle (2K to 300K). Due to the high sensitivity of these detectors, any kind of em noise such as mobile phones, electrical machines or a light switch operated in the vicinity of the detector will induce a peak in the dark count rate of several kHz. During an antibunching experiment the count rates have to be constantly monitored since on occasions the detectors

become unstable and the dark count starts to oscillate with increasing amplitude due to external interferences.

Using the setup described in section 2.3, and adjusting the bias current on the SSPDs to obtain a dark count of 10-30Hz, the setup is tested by measuring the correlations between the output detection signal of the two SSPDs illuminated by laser pulses emitting at 750nm (Fig. 4.13). As expected the histogram in characterized by a series of peaks whose integrated areas are all the same within the statistical fluctuation of the measurement: this is the signature of the intensity correlation function for a coherent pulsed source. The FWHM=440ps of the peaks corresponds to twice the jitter of the system. Using the same setup we measured the $g^{(2)}(0)$
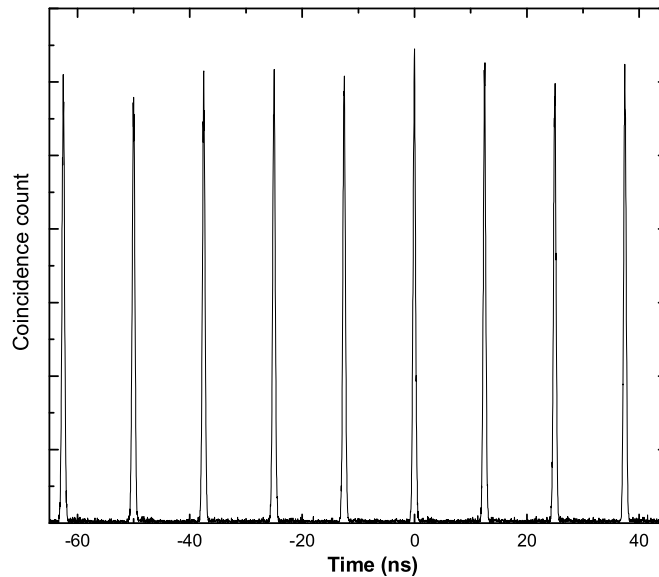

Figure 4.13: Intensity correlation measured on a pulsed laser.

for a single X line from a QD. As we have seen (section 4.1.2) the choice of the power density is very important and to avoid investing a lot of time in measuring the correlation function at different power intensities, a convenient way of finding

76

the optimum regime is to plot the power as a function of the count rates and perform a first correlation measurement at 50% of the saturation power. A preliminary measurement is shown in Fig. 4.14 made at a power of 50nW at 750nm and repetition frequency of 80MHz. We remark that this repetition frequency is unachievable with our APDs. Although a recent demonstration of gated operation at a repetition frequency of 800MHz has been achieved [92], the SNR is still to low for single photon experiments. The coincidence histogram is characterized by periodic peaks separated by the laser repetition period except for zero delays; this is the signature of a single photon emitter under pulsed excitation. The peaks are well fitted by Gaussian time distributions with an offset of 3 coincidences and a FWHM = 2.2ns that corresponds to twice the X lifetime [93]. The coincidences between the peaks are due to uncorrelated light entering the system and detector dark counts.

A more interesting measurement which reveals the dynamics of the charge population of the QD is the measurement of the $g^{(2)}(\tau)$. The measurement was made on the positively charged exciton emission (inset Fig. 4.15b) under cw excitation by pumping resonantly in the excited state of the trion (section 3.3). The resulting histogram, measured for a pump power of 0.2mW, is shown in Fig. 4.15a for long delays (0.5μs). For time delays between 3ns and 200ns an increase of the correlation function is observed: this bunching behavior, already studied for short-wavelength QDs [94], shows that after emission of a photon from the positive trion the QD remains charged allowing the re-excitation of the charged exciton state. For short time delays <3ns, (see Fig. 4.15b), an antibunching dip is observed, confirming the sub-Poissonian statistics of the light emitted by the trion line. The bunching and antibunching behavior can be modeled in a three level system with the following
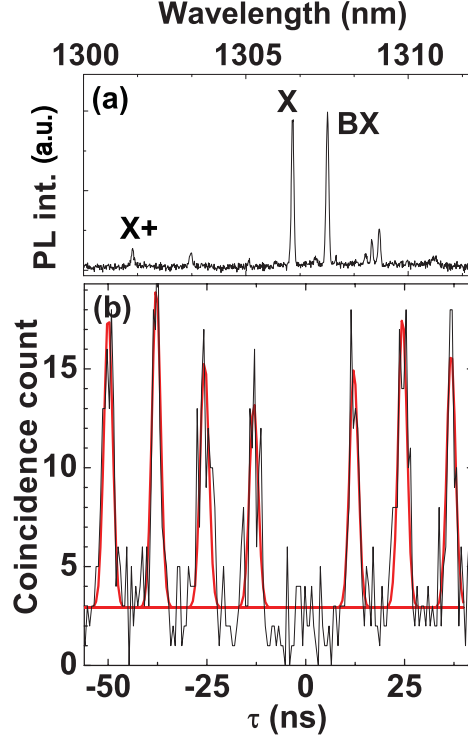
Figure 4.14: (a) Spectrum of the single QD showing the X line used for the photon autocorrelation measurement(b) under pulsed excitation obtained with an integration time of 1.8hrs and a time bin of 560ps. Solid (red) line is a sum of Gaussians with FWHM=2.2ns and an offset of 3 coincidences..

expression [29]: $g^{(2)}(\tau) = 1 - (1+a)*exp(-\tau/\tau1) + a*exp(-\tau/\tau_2)$. To account for the limited setup resolution, detection of uncorrelated photons and dark counts, we fitted the experimental data by convolving a gaussian time distribution (FWHM=220ps) with the correlation function corrected for noise [85]: $g_n^{(2)}(\tau) = 1 + \rho^2(g^{(2)}(\tau) - 1)$. The fit provides the values, a=0.8, τ_1=0.62ns, τ_2=170.8ns and $g^{(2)}(0) = 0.18 \pm 0.02$.

Although the analytical expression for the correlation function derived in Ref.[29] is applicable to our case and describes the light statistics correctly, for a physical interpretation of the fitting parameters we cannot use the expressions derived in Ref.[29] since the system of rate equations is not compatible with our system. We used the three level system described in Fig. 4.16, and the related system of rate

78
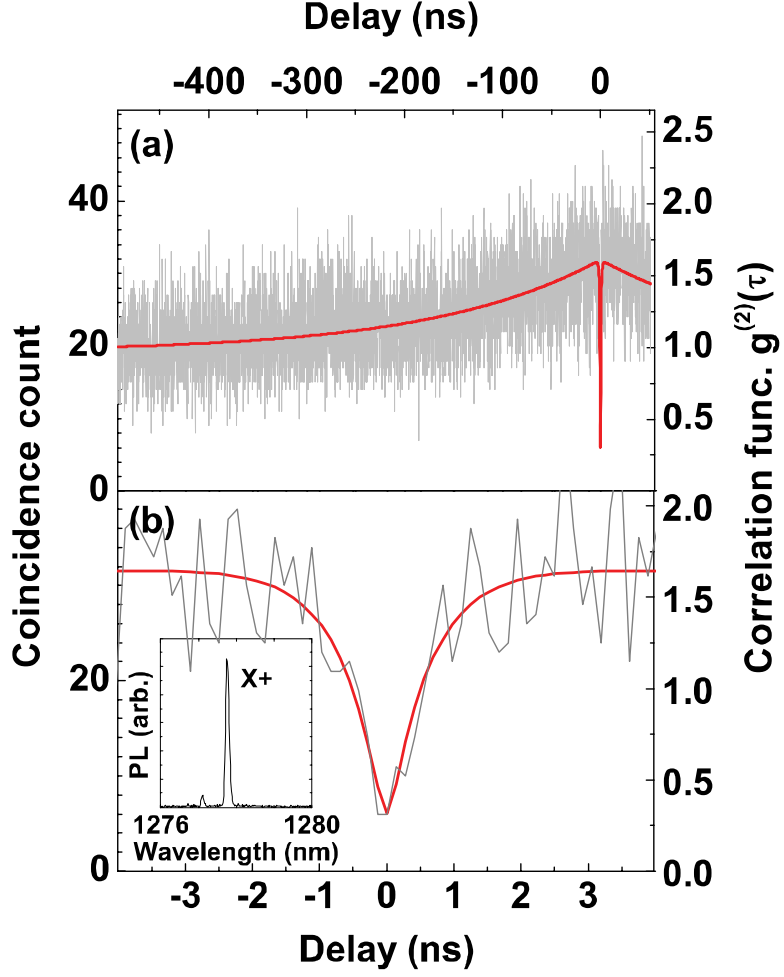
Figure 4.15: a) Measurement of $g^{(2)}(\tau)$ under resonant excitation, with a time bin of 139ps. (b) Blow-up at short time delays demonstrating antibunching. Inset: PL spectrum of the positive trion under resonant excitation (T=10K). Solid (red) line in (a) and (b) is the fit of the correlation function $g^{(2)}(\tau)$.

equations:

$$
\begin{aligned}
\frac{dw_3}{dt} &= \frac{w_2}{t_1} - \frac{w_3}{t_2} \\
&= \frac{w_1}{t_3} + \frac{w_3}{t_2} - \frac{w_2}{t_1} - \frac{w_2}{t_4} \\
&= -\frac{w_1}{t_3} + \frac{w_2}{t_4},
\end{aligned}
$$

where $w_{1,2,3}$ represent the probability of finding the dot empty, occupied by a single hole in the GS, or by an exciton and a hole in the GS, respectively. The time constants t_3 and t_4 are the capture time and escape time for a single hole: the presence

79

of holes in the VB are due to unwanted impurity doping levels. Only when the dot is charged by a hole the energy of the laser beam is resonant with the charged P state and can excite an electron into the conduction band, which then relaxes on a time scale of a few ps to the S state and forms the X+. Since the relaxation time is much faster than the X+ radiative time (t_2), in the model we assume that the laser excites directly in the charged S state with a time constant t_1. The intensity correlation function is related to the the probability of emitting a photon at a time t+τ after a photon has been emitted at time t: a photon emitted from the recombination of the charged exciton ensures that the QD is prepared in the charged state, this state represents the initial conditions of the system ($w_1 = 1$ and $w_0 = w_3 = 0$). The $g^{(2)}$ is then determined by the probability of the QD population evolving into the X+ state. The model was used to fit two intensity correlation measurements taken at different excitation powers. All the time constants are different between the two fits: although t_1 and t_2 are expected to depend on the excitation intensity, the escape and capture time of the holes where not. This implies that other mechanisms are involved: photoabsorbtion by the holes in the VB of the QD and subsequent escape into the continuum, or scattering processes originating from the relaxation of the exciton from ES to the GS expelling the hole. More experimental data and a more complex model involving the formation of other exciton spices are required to build a realistic simulation of the charge dynamics in the QD.
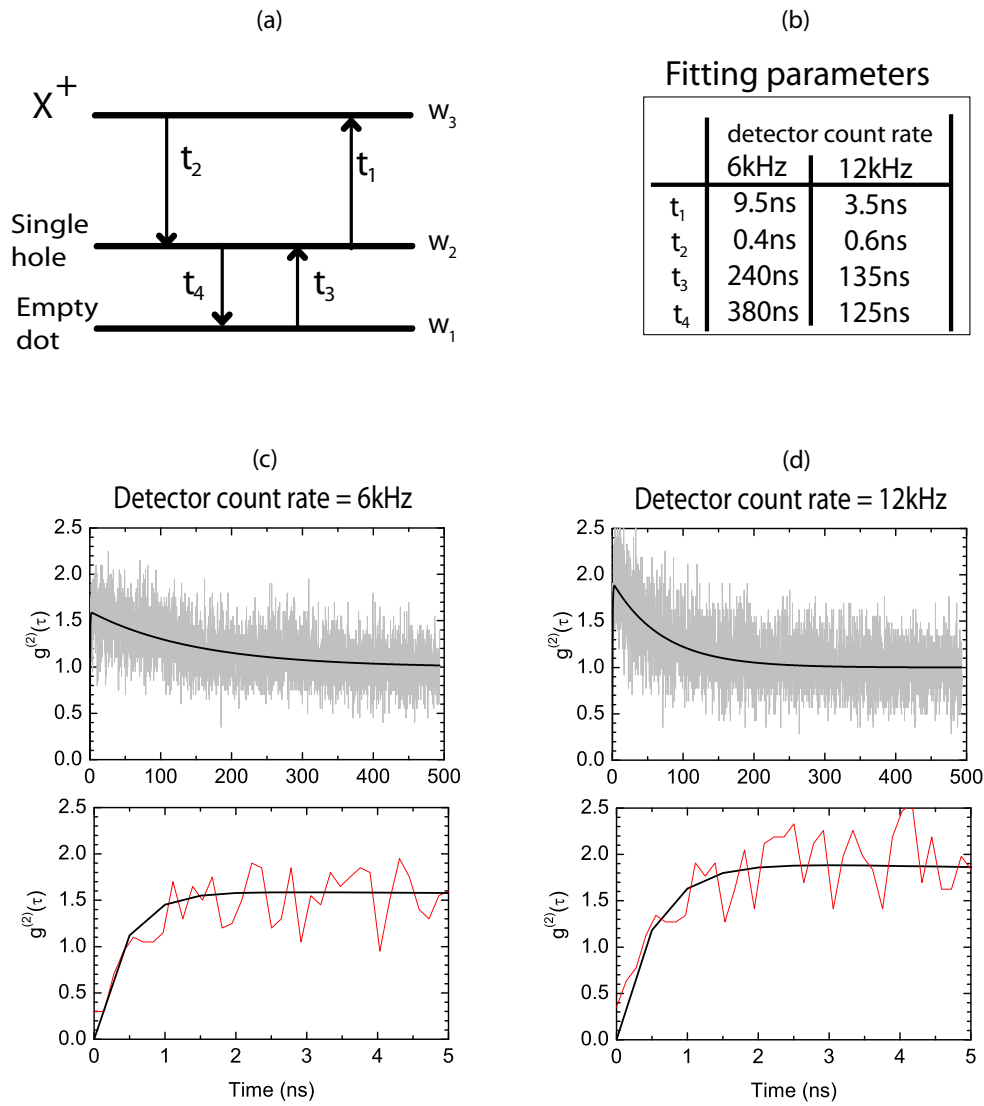
Figure 4.16: (a)Model of the three level system. (b) fitting parameters. (c and d) Fit (black thick line) to the experimental data.

Chapter 5

Purcell-LEDs

We have shown that our QDs can be optically excited to generate single photon states. However for practical applications, electrical pumping would be much preferred to avoid the need of pulsed pump lasers and micro-photoluminescence apparatus. We have also discussed the need to increase the extraction efficiency into the collection optics. One method consists in coupling the QD emission to the fundamental mode of a wavelength-sized microcavity with high quality factor (Q) and small mode volume. In such a structure the spontaneous emission (SE) rate can be increased over the bulk volume as originally predicted by Purcell[23], and experimentally demonstrated in the solid state[95, 96, 97]. This SE increase implies that most photons are emitted in the microcavity mode, which in principle can be easily extracted and leads to a much improved efficiency and higher repetition rates. Electrically pumped single QD emission has been demonstrated by post filtering [98], with a small metal aperture, with no carrier and no optical confinement. Control of carrier injection, in a submicrometer area, has been proposed [99] and achieved [100] using an oxide current aperture surrounded by a weakly confined optical cavity. On the other side, vertical cavity surface emitting lasers (VCSEL), that commonly employ DBRs and oxidized current apertures, achieve electrical and optical confinement with much larger dimensions (typically $> 2\mu$m). In this chapter, we introduce the Purcell-LED, a microcavity QD LED structure that uses an oxidized aperture and DBRs to confine at the same time the carrier injection and the optical mode in

a sub-micrometer volume.

5.1 Purcell-LEDs device fabrication

The structures have been processed from a planar micro-cavity grown by MBE on (001) oriented n-doped GaAs substrate. The active region consists of a single array of self assembled QDs formed from 3 mono-layers of InAs and capped with a 5 nm strain-reducing $In_{15}Ga_{85}As$ layer to extend the emission into the near infrared. In this first test, we used high-density QDs ($3*10^{10}dots/cm^2$) emitting at 1300nm. The QDs are embedded in undoped GaAs. Lateral current and optical confinement is provided by an $Al_{0.85}Ga_{0.15}As$ layer, deposited on the top (p-side) of the GaAs layer, which is laterally oxidized resulting in an insulating, low-index (n∼1.6) aperture. An optical cavity with a target Q (from a 1D simulation neglecting lateral loss) of ∼1000 is obtained by embedding the active region between a top mirror composed of 5 $Al_{0.75}Ga_{0.25}As/GaAs$ quarter-wave pairs plus a top Au layer, and a bottom (output) mirror composed by three pairs of oxidized AlAs/GaAs and 3 pairs of $Al_{0.9}Ga_{0.1}As/GaAs$. Using optical lithography and reactive ion etching we fabricated cylindrical mesa structures with diameters ranging from 10.5μm down to 1.2μm. The etching was stopped in the $Al_{0.85}Ga_{0.15}As$ aperture layer, which was then oxidized, at 400C for 90min in an H_2O atmosphere. In the same oxidation step the AlAs layers where laterally oxidized from trenches etched at 20μm distance from the mesa. The etched surface was electrically insulated with an Si_3N_4 layer deposited by plasma-enhanced chemical-vapor deposition. Au pads were deposited on the mesas to form the p-contact and a layer of Au on the substrate was used as n-contact.
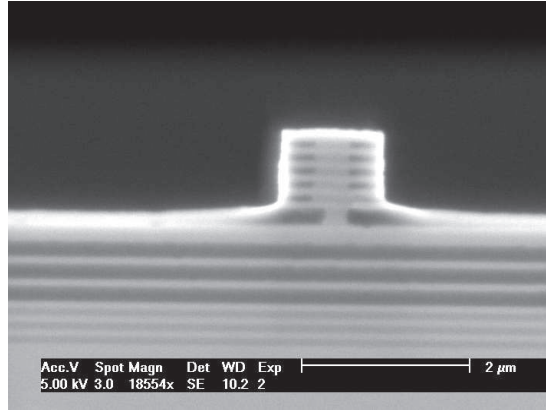
Figure 5.1: SEM cross sectional image of an aperture of 360nm. The darker regions represent the oxidized AlGaAs and AlAs layers.

5.2 Purcell-LEDs characterization

In order to determine the aperture area, a first estimation of the lateral oxidised distance was obtained on etched stripes from cross-sectional SEM images, as shown on Fig. 5.1. The aperture diameter in the mesa was further verified by measuring the scaling of the current-voltage characteristic for different nominal device diameters. As shown in [100] we expect current spreading and carrier diffusion to be negligible in this structure. Despite a high turn-on voltage (due to unoptimized p-doping in the top mirror), all curves can be fitted with a single oxidized length parameter that is also consistent with the SEM estimate.

Figure 5.2 reports light versus current characteristics at room temperature for a range of devices with different oxide apertures, showing that light is extracted from devices as small as 400nm in diameter. The measured efficiency is $3.1 * 10^{-4}$ for the largest devices (9.5μm) and decreases to $1.4 * 10^{-4}$ for the 400nm LEDs. The low efficiency is mostly due to the mismatch between the cavity line width and the source spectral width: the QD emission is limited by the inhomogeneous broadening. The QD LEDs are designed to be efficient devices only for the one or few QDs that are

84
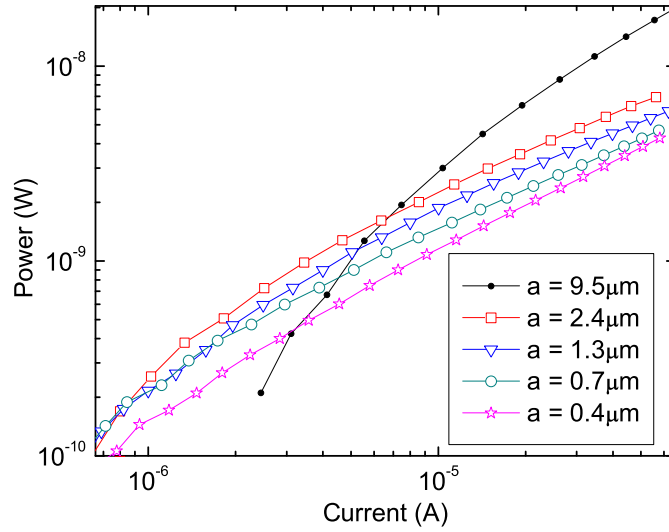
Figure 5.2: Light versus current characteristics (293K) curves for devices with different aperture diameter a.

resonant with the cavity mode: the ultimate goal is to demonstrate enhancement of spontaneous emission from a single emitter which requires high quality factors and small mode volumes. Optimization of these parameters compromises the efficiency for the QD ensemble.

The cw electro-luminescence spectra at 293K are presented in logarithmic scale in Fig. 5.3 for devices with decreasing oxide apertures. The devices where individually contacted on the Au pads and the luminescence was collected with a 100μm core optical fiber in contact with the substrate side, and dispersed into a spectrometer equipped with a liquid nitrogen cooled InGaAs near infrared detector. The individual measurements are characterized by several spectral lines corresponding to the resonant cavity modes. When compared to the single peaked spectra of the planar cavity at 1180nm, this is evidence of strong optical confinement. The ground state transition of the QD is centered at 1245nm (at 293K), the cavity modes are
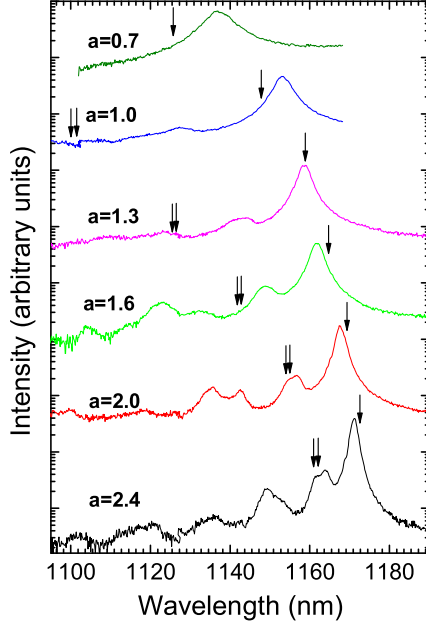
Figure 5.3: Electroluminescence spectra (293K) of microcavities with different oxide apertures (aperture diameter is indicated for each spectra). The arrows indicate the positions of the modes predicted by the effective index model. The modes indicated on each spectrum are respectively from right to left: $HE_{11} HE_{21}$ and EH_{01}, according to the standard convention[101].

therefore pumped by the excited states of the QDs. The inhomogeneous broadening of the QD emission (measured to be 18nm on similar samples without cavity), ensures that the narrow spectral features are related to the cavity modes and not to QD electronic states. As the diameter of the current aperture is reduced we observe a blue shift of the cavity ground state transition (Fig. 5.4(a)) and an increase in the splitting between cavity modes consistent with the conventional theoretical trend for increased lateral confinement. We stress that the energy shift (45meV for the 0.7μm diameter devices) is much larger than the shift commonly measured in VCSELs and comparable to the shift observed in micropillars.

The standard approach [102] used for quantitatively analyzing the optical confinement in cylindrical dielectric structures is based on the assumption that the

Figure 5.4: (a) Comparison of the experimental shift of the fundamental cavity resonance (dots) and prediction by the effective index model (continuous line). (b) Cavity quality factor is plotted as a function of the shift in energy with respect to the planar cavity emission.

transverse component of the resonant electromagnetic field is independent from the longitudinal component, assumption usually correct for planar cavities or 3D cavities with dimensions larger than the wavelength [101]. In this effective index approach[102], the cavity is treated as a 2D circular waveguide with core and cladding indexes given by an effective index weighted by the standing field in the axial direction. In this framework, we solved numerically the eigenvalue equation for the longitudinal standing wave in the core (unoxidised region) approximated to a planar cavity. The resonant wavelength obtained was 1193nm while the averaged refractive index weighted with the standing field intensity was 3.053. For the cladding (oxidised region) the refractive index was calculated to be 2.757 from the relation [102]: $\Delta\lambda/\lambda = \Delta n/n$. Using these values we applied the numerical methods used for evaluating the confined modes for a step index optical fibre [101] (shown as arrows in Fig. 5.3 and as a continuous line in Fig. 5.4(a)). Good agreement was found between experimental evidence and calculated modes for apertures down to 2.0μm, see figure 5.3, below which the cavity dimensions become comparable to the resonant
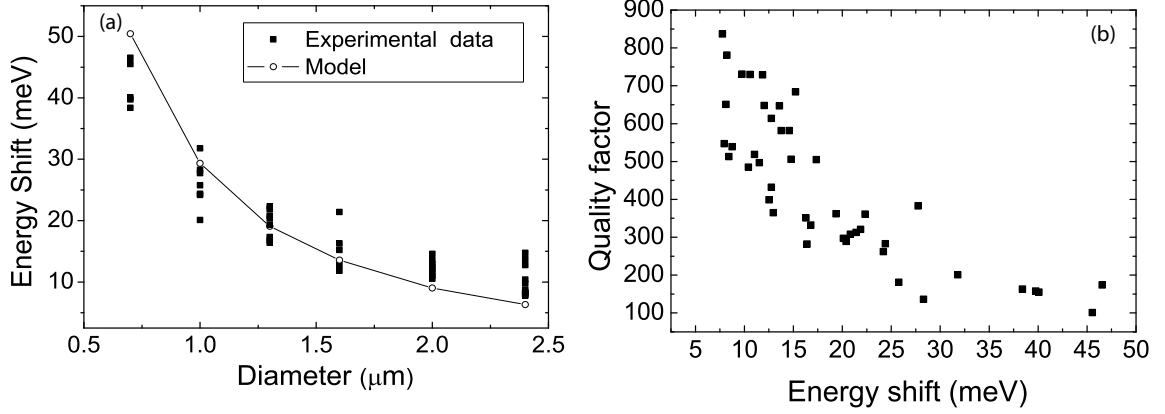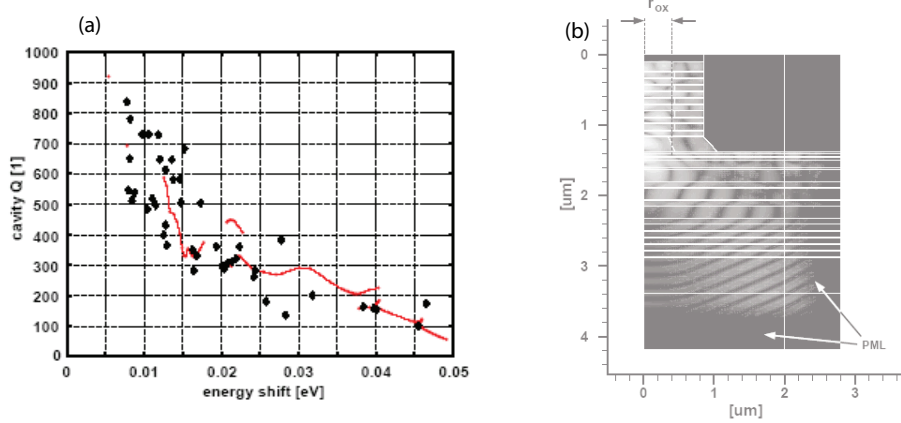
Figure 5.5: (a) Comparison of the experimental shift of the fundamental cavity resonance (dots) and prediction by FEM simulations (continuous red line). (b) Calculated field showing diffraction losses at the oxide aperture. [103]

wavelength and we observe a significant difference between the experimental and theoretical splitting of the cavity modes, thus confirming that the confinement of the transverse component becomes substantial in the smaller devices where the approximation in the effective index model is no longer valid. It is interesting to note that the model predicts single mode propagation when the normalized frequency falls below 2.405 (the first zero in the Bessel J_o function) which corresponds to an oxide aperture of 690nm in our devices. In Figure 5.3 the QD LEDs with apertures estimated at 0.7μm do not indeed show any evidence of multimode confinement, at least within the broad emission spectrum of the QDs. We observe a significant spread in the resonant energies for devices with the same nominal diameter. This can be attributed to variations in the mesa diameters and oxidized length.

Because actual diameters can vary among nominally identical devices we plot in Fig. 5.4(b) the quality factor measured in over 40 devices as a function of the resonant energy shift. Beside the variations in the Q value, probably due to the fluctuating quality of the mesa etching (the dimensions being comparable to the

88

resolution of our optical lithography) a clear trend of decreasing Q for increasing lateral confinement is observed. To gain further understanding of the influence of the cavity geometry on the Q, the optical modes of the microcavities are determined by solving Maxwell's wave equation employing vectorial finite elements [103] (the simulations were done at the ETHZ by M.Streiff and B.WItzigmann). Excellent agreement is achieved between measurements and simulations 5.5(a). The strong degradation of the Q factor observed for oxide confinements with diameters smaller than 1μm are attributed to excessive diffraction losses at the oxide aperture as shown by the calculated field for an aperture of 0.8μm 5.5(b).

In conclusion the degradation of the Q of the cavity seems to be intrinsic to the oxide aperture, making it difficult to obtain a significant enhancement of the spontaneous emission. The high voltages required to inject carriers in the QD, due to unoptimized growth of DBRs, prevented operation at low temperature. For these reasons, we are developing and modeling (at ETHZ) electrically pumped PC cavities.

Chapter 6

Conclusions

The goal of this project was to study and develop a QD based single photon source at telecom wavelength. In particular this thesis dealt with the optical characterization of the single QD device emitting at 1300nm. Thanks to the development and optimization of a novel growth technique we where were able to achieve at the same time emission at 1300nm and ultra low QD densities. A low dot density requires less spatial resolution to selectively inject carriers and/or extract light from a single QD, as a result device fabrication requires less complex technology. To increase the extraction efficiency we embedded the dot in a planar microcavity which yielded an order of magnitude increase in the light extracted as compared to QDs buried in bulk GaAs. The optical properties of the QDs where studied under different optical excitation conditions. Commercial lasers where used to photogenerate carriers in the bulk material and WL. To pump resonantly in the excited states of the QD we developed a temperature control system to tune and stabilize a standard telecom laser from 1210nm to 1300nm. With integrated and time resolved PL measurements we studied the carrier population and dynamics at the single exciton level. Our single QD devices present clear and reproducible spectral signatures in which we can identify X, BX and charged exciton transitions. Quasi-resonant excitation at 70K demonstrates background free single exciton transitions which is very promising for the realization of a single photon device operating at temperatures in easy reach of cryogen-free coolers. Taking advantage of the high

sensitivity of single photon InGaAs APDs we built a TCSPC setup and measured the radiative lifetimes of single exciton transitions. We have also found new evidence confirming the presence of a background emission superposed to the narrow spectral transitions. Antibunching measurements at these wavelengths required the nontrivial task of building a setup to detect fiber-coupled single photons in a 300ps time window, emitted from a nano-device in free space at cryogenic temperatures, with the capability of maintaining the optical alignment on a micrometer scale for several hours. With such a setup we have demonstrated that our QDs can generate single photon states at 1300nm. We used this single photon source to characterize novel detectors based on superconducting nanowires and measured for the first time the intensity correlation function at 1300nm on single photons from a QD. These detectors show at least 2 orders of magnitude improvement on the signal to noise ratio as compared to InGaAs APDs, this is very important since for a QKD system the detector noise, amongst others, determines the maximum distance over which a secure key can be exchanged. It should be noted that due to the difficulties in these measurements, to date there has been only one other clear demonstration of single photon emission at 1300nm. As compared to that work our single QD devices present clear X, BX and charged exciton identification through PL and TRPL measurements. It should also be noted that the extraction efficiency of our device into the collection optics is amongst the highes reported in literature for QDs embedded in a variety of structures emitting above and below the silicon spectral window.

Besides the demonstration of single photon emission in the telecom wavelength range, this thesis has contributed to demonstrating that due to the the deeply confined structures these QDs offer a new tool for investigating the interactions between

the confined exciton states and the carries surrounding the QD. There is the potential to achieve significant results with a campaign of dedicated measurements: understanding of the mechanisms involved in the carrier dynamics can lead to the design of devices with improved single photon properties. In the antibunching experiments the single photon efficiency measured in the fiber is close to the security limit for QKD applications, but replacing the APDs with stable SSPDs brings the SNRs within acceptable levels. Nevertheless the efficiency of the source is a problem that must be addressed since a device with 40dB efficiency cannot be termed 'single photon source *on demand*'. The solution of the efficiency problem must address two issues: the losses in the light extraction from the device and in the SMF coupling stage. Coupling directly the mode from a micropillar structure into the fiber guided mode, although technologically complex, has the potential for improving the efficiency by at least one order of magnitude. Another possibility comes from the new generation of devices based on photonic crystal defect micro cavities. These devices are very attractive since they can achieve high Purcell enhancement factors due to the small mode volumes: extraction efficiencies as high as 50% are predicted for devices without a bottom mirror. Preliminary calculations show that the spatial distribution of the mode is compatible with 0.5NA collection optics. But a successful and efficient implementation of the collection strategies mentioned above relies on the development of growth techniques for controlling the nucleation sites of QDs.

Bibliography

[1] S. Kaiser, T. Mensing, L. Worschech, F. Klopf, J. P. Reithmaier, and A. Forchel. "Optical spectroscopy of single InAs/InGaAs quantum dots in a quantum well". *App. Phys. Lett.*, 81(26):4898, 2002.

[2] N. I. Cade, H. Gotoh, H. Kamada, H. Nakano, S. Anantathanasarn, and R. Notzel. "Optical characteristics of single InAs/InGaAsP/InP (100) quantum dots emitting at 1.55μm". *App. Phys. Lett.*, 89(18):181113, 2006.

[3] G. Saint-Girons, N. Chauvin, A. Michon, G. Patriarche, G. Beaudoin, G. Braámond, C. Bru-Chevallier, and I. Sagnes. "Microphotoluminescence of exciton and biexciton around 1.5μm from a single InAsInP (001) quantum dot". *App. Phys. Lett.*, 88(13):133101, 2006.

[4] N. I. Cade, H. Gotoh, H. Kamada, T. Tawara, T. Sogawa, H. Nakano, and H. Okamoto. "Charged exciton emission at 1.3μm from single InAs quantum dots grown by metalorganic chemical vapor deposition". *App. Phys. Lett.*, 87(17):1, 2005.

[5] K. Takemoto, Y. Sakuma, S. Hirose, T. Usuki, N. Yokoyama, T. Miyazawa, M. Takatsu, and Y. Arakawa. "Single InAs/InP quantum dot spectroscopy in 1.3-1.55μm telecommunication band". *Phys. E*, 26(1-4):185, 2005.

[6] M. B. Ward, O. Z. Karimov, D. C. Unitt, Z. L. Yuan, P. See, D. G. Gevaux, A. J. Shields, P. Atkinson, and D. A. Ritchie. "On-demand single-photon source for 1.3μm telecom fiber". *Appl. Phys. Lett.*, 86(20):201111, 2005.

[7] A. Zeilinger, G. Weihs, T. Jenmewein, and M. Aspelmeyer. "Happy centenary, photon". *Nature*, 433(7023):230, 2005.

[8] J. G. Rarity, P. C. M. Owens, and P. R. Tapster. "Quantum random-number generation and key sharing". *J. Mod. Optics*, 41(12):2435, 1994.

[9] C.H. Bennet and G. Brassard. In *IEEE International Conference on Computers, Systems and Signal Processing*, page 175, Bangalore, India, 1984. IEEE, New York.

[10] N. Gisin, G. Ribordy, W. Tittel, and H. Zbinden. "Quantum cryptography". *Rev. Mod. Phys.*, 74(1):145, 2002.

[11] E. Knill, R. Laflamme, and G.J. Milburn. "A scheme for efficient quantum computation with linear optics". *Nature*, 409:46, 2001.

[12] R. M. Stevenson, R. J. Young, P. Atkinson, K. Cooper, D. A. Ritchie, and A. J. Shields. "A semiconductor source of triggered entangled photon pairs". *Nature*, 439(7073):178, 2006.

[13] W. K. Wootters and W. H. Zurek. "A single quantum cannot be cloned". *Nature*, 299(5886):802, 1982.

[14] C. H. Bennett. "Quantum cryptography using any two nonorthogonal states". *Phys. Rev. Lett.*, 68(21):3121, 1992.

[15] C. Gobby, Z. L. Yuan, and A. J. Shields. "Quantum key distribution over 122 km of standard telecom fiber". *Appl. Phys. Lett.*, 84(19):3762, 2004.

[16] A. J. Bennett, D. C. Unitt, P. Atkinson, D. A. Ritchie, and A. J. Shields. "High performance single photon sources from photolithographically defined pillar microcavities". *Opt. Expr.*, 13(1):50, 2005.

[17] R. Loudon. *The quantum theory of light*. Okford university press, New York, third edition, 2004.

[18] D.F. Walls and G.J. Milburn. *Quantum optics*. Springer, US, 1994.

[19] R. Q. Twiss R. Hanbury-Brown. *Nature*, 177:27, 1956.

[20] B. Lounis and M. Orrit. "Single-photon sources". *Rep. Prog. Phys.*, 68(5):1129, 2005.

[21] P. Grangier, B. Sanders, and J. Vučković. "Focus on single photons on demand". *New J. of Phys.*, 6, 2004.

[22] A. Niederberger, V. Scarani, and N. Gisin. "Photon-number-splitting versus cloning attacks in practical implementations of the bennett-brassard 1984 protocol for quantum cryptography". *Phys Rev A*, 71(4):1, 2005.

[23] E.M. Purcell. "Spontaneous emission probabilities at radio frequencies". *Phys. Rev.*, 69:681, 1946.

[24] Y. Lill and B. Hecht. "Single dye molecules in an oxygen-depleted environment as photostable organic triggered single-photon sources". *Appl. Phys. Lett.*, 84(10):1665, 2004.

[25] P. Michler, A. Kiraz, C. Becher, W. V. Schoenfeld, P. M. Petroff, L. Zhang, E. Hu, and A. Imamoğlu. "A quantum dot single-photon turnstile device". *Science*, 290(5500):2282, 2000.

[26] J. McKeever, A. Boca, A. D. Boozer, R. Miller, J. R. Buck, A. Kuzmich, and H. J. Kimble. "Deterministic generation of single photons from one atom trapped in a cavity". *Science*, 303(5666):1992, 2004.

[27] S. Fasel, O. Alibart, S. Tanzilli, P. Baldi, A. Beveratos, N. Gisin, and H. Zbinden. "High-quality asynchronous heralded single-photon source at telecom wavelength". *New J. of Phys.*, 6, 2004.

[28] A. Kiraz, M. Ehrl, Th Hellerer, Ö. E. Müstecaplioğlu, C. Bräuchle, and A. Zumbusch. "Indistinguishable photons from a single molecule". *Phys. Rev. Lett.*, 94:223602, 2005.

[29] S. C. Kitson, P. Jonsson, J. G. Rarity, and P. R. Tapster. "Intensity fluctuation spectroscopy of small numbers of dye molecules in a microcavity". *Phys Rev A*, 58(1):620, 1998.

[30] R. Brouri, A. Beveratos, J. P. Poizat, and P. Grangier. "Photon antibunching in the fluorescence of individual color centers in diamond". *Opt. Lett.*, 25(17):1294, 2000.

[31] B. Fisher, J. M. Caruge, D. Zehnder, and M. Bawendi. "Room-temperature ordered photon emission from multiexciton states in single CdSe core-shell nanocrystals". *Phys. Rev. Lett.*, 94(8):087403, 2005.

[32] M. T. Borgström, V. Zwiller, E. Müller, and A. Imamoglu. "Optically bright quantum dots in single nanowires". *Nano Lett.*, 5(7):1439, 2005.

[33] P. Atkinson, M. B. Ward, S. P. Bremner, D. Anderson, T. Farrow, G. A. C. Jones, A. J. Shields, and D. A. Ritchie. "Site control of InAs quantum dot nucleation by ex situ electron-beam lithographic patterning of GaAs substrates". *Phys. E*, 32:21, 2006.

[34] A. Badolato, K. Hennessy, M. Atature, J. Dreiser, E. Hu, P. M. Petroff, and A. Imamoğlu. "Deterministic coupling of single quantum dots to single nanocavity modes". *Science*, 308(5725):1158, 2005.

[35] J.M. Gérard, J. M.rard and B. Gayral. "Toward high-efficiency quantum-dot single photon sources". *Proc. SPIE*, 5361:88, 2004.

[36] D. Bimberg, M. Grundmann, and N. N. Ledentsov. *Quantum dot heterostructures*. Wiley, Chichester, 1999.

[37] S. Rodt, R. Heitz, A. Schliwa, R. L. Sellin, F. Guffarth, and D. Bimberg. "Repulsive exciton-exciton interaction in quantum dots". *Phys. Rev. B*, 68(3):353311, 2003.

[38] G. A. Narvaez, G. Bester, and A. Zunger. "Excitons, biexcitons, and trions in self-assembled (In,Ga)As gaas quantum dots: Recombination energies, polarization, and radiative lifetimes versus dot height". *Phys. Rev. B*, 72(24):1, 2005.

[39] Leroy L.Chang and Klaus Ploog. *Molecular beam epitaxy [MBE] and heterostructures*. NATO ASI series; series E - applied sciences, no. 87. Nijhoff, Dordrecht, 1985.

[40] D. Leonard, K. Pond, and P.M. Petroff. "Critical layer thickness for self-assembled InAs islands on GaAs". *Phys. Rev. B*, 50(16):11687, 1994.

[41] J. M. Gérard, J. B. Genin, J. Lefebvre, J. M. Moison, N. Lebouche, and F. Barthe. "Optical investigation of the self-organized growth of InAs/GaAs quantum boxes". *J Cryst Growth*, 150(1 -4 pt 1):351, 1995.

[42] B. Alloing, C. Zinoni, V. Zwiller, L. H. Li, C. Monat, M. Gobet, G. Buchs, A. Fiore, E. Pelucchi, and E. Kapon. "Growth and characterization of single quantum dots emitting at 1300 nm". *Appl. Phys. Lett.*, 86(10):101908, 2005.

[43] Holger T. Grahn. *Introduction to semiconductor physics*. World Scientifc, Singapore, 1999.

[44] D. V. O'Connor and D. Phillips. *Time-correlated single photon counting.* Academic Press, London, 1984.

[45] E. Fred Schubert. *Light-emitting diodes.* Cambridge University Press, Cambridge, 2003.

[46] H. Benisty, H. De Neve, and C. Weisbuch. "Impact of planar microcavity effects on light extraction - part i: Basic concepts and analytical trends". *IEEE J. of Quantum Elect.*, 34(9):1612, 1998.

[47] P. Yeh. *Optical waves in layered media.* Wiley, New York, 1998.

[48] B. Alloing. *Growth of Single Quantum Dot Devices for Fiber-based Quantum Communications.* PhD thesis, EPFL, 2006.

[49] "The processing of the structures was done at the institute of phtonics and nanotechnology of the italian CNR (Rome).".

[50] C. F. Wang, A. Badolato, I. Wilson-Rae, P. M. Petroff, E. Hu, J. Urayama, and A. Imamoğlu. "Optical properties of single InAs quantum dots in close proximity to surfaces". *Appl. Phys. Lett.*, 85(16):3423, 2004.

[51] W.L. Barnes, G. Björk, J.M. Geérard, P. Jonsson, J.A.E. Wasey, P.T. Worthing, and V. Zwiller. "Solid-state single photon sources: light collection strategies". *Eur. Phys. J. D*, 18:197, 2002.

[52] J. Vučković, M. Pelton, A. Scherer, and Y. Yamamoto. "Optimization of three-dimensional micropost microcavities for cavity quantum electrodynamics". *Phys Rev A*, 66(2):023808, 2002.

[53] P. Royo, R. P. Stanley, and M. Ilegems. "Planar dielectric microcavity light-emitting diodes: Analytical analysis of the extraction efficiency". *J Appl Phys*, 90(1):283, 2001.

[54] J. J. Finley, A. D. Ashmore, A. Lematre, D. J. Mowbray, M. S. Skolnick, I. E. Itskevich, P. A. Maksym, M. Hopkinson, and T. F. Krauss. "Charged and neutral exciton complexes in individual self-assembled In(Ga)As quantum dots". *Phys. Rev. B*, 63(7):073307, 2001.

[55] Ph Lelong and G. Bastard. "Binding energies of excitons and charged excitons in GaAs/Ga(In)as quantum dots". *Sol. Stat. Comm.*, 98(9):819, 1996.

[56] D. V. Regelman, E. Dekel, D. Gershoni, E. Ehrenfreund, A. J. Williamson, J. Shumway, A. Zunger, W. V. Schoenfeld, and P. M. Petroff. "Optical spectroscopy of single quantum dots at tunable positive, neutral, and negative charge states". *Phys. Rev. B*, 64(16):1653011, 2001.

[57] L. He and A. Zunger. "Multiple charging of InAs GaAs quantum dots by electrons or holes: Addition energies and ground-state configurations". *Phys. Rev. B*, 73(11):115324, 2006.

[58] John H. Davies. *The physics of low-dimensional semiconductors : an introduction.* Cambridge University Press, Cambridge, 1998.

[59] G. A. Narvaez, G. Bester, and A. Zunger. "Excitons, biexcitons, and trions in self-assembled (In,Ga)As GaAs quantum dots: Recombination energies, polarization, and radiative lifetimes versus dot height". *Phys. Rev. B*, 72(24):245318, 2005.

[60] D. V. Regelman, U. Mizrahi, D. Gershoni, E. Ehrenfreund, W. V. Schoenfeld, and P. M. Petroff. "Semiconductor quantum dot: A quantum light source of multicolor photons with tunable statistics". *Phys. Rev. Lett.*, 87(25):257401, 2001.

[61] M. Ediger, P. A. Dalgarno, J. M. Smith, B. D. Gerardot, R. J. Warburton, K. Karrai, and P. M. Petroff. "Controlled generation of neutral, negatively-charged and positively-charged excitons in the same single quantum dot". *Appl. Phys. Lett.*, 86(21):211909, 2005.

[62] E. S. Moskalenko, K. F. Karlsson, P. O. Holtz, B. Monemar, W. V. Schoenfeld, J. M. Garcia, and P. M. Petroff. "Influence of excitation energy on charged exciton formation in self-assembled InAs single quantum dots". *Phys. Rev. B*, 64(8):853021, 2001.

[63] R. Oulton, J. J. Finley, A. I. Tartakovskii, D. J. Mowbray, M. S. Skolnick, M. Hopkinson, A. Vasanelli, R. Ferreira, and G. Bastard. "Continuum transitions and phonon coupling in single self-assembled stranski-krastanow quantum dots". *Phys. Rev. B*, 68(23):2353011, 2003.

[64] B. Patton, W. Langbein, and U. Woggon. "Trion, biexciton, and exciton dynamics in single self-assembled CdSe quantum dots". *Phys. Rev. B*, 68(12):125316, 2003.

[65] A. Berthelot, I. Favero, G. Cassabois, C. Voisin, C. Delalande, Ph Roussignol, R. Ferreira, and J. M. Gérard. "Unconventional motional narrowing in the optical spectrum of a semiconductor quantum dot". *Nature Phys.*, 2(11):759, 2006.

[66] A. Markus, A. Fiore, J. D. Ganire, U. Oesterle, J. X. Chen, B. Deveaud, M. Ilegems, and H. Riechert. "Comparison of radiative properties of InAs quantum dots and GaInNAs quantum wells emitting around 1.3μm". *Appl. Phys. Lett.*, 80(6):911, 2002.

[67] O. Labeau, P. Tamarat, and B. Lounis. "Temperature dependence of the luminescence lifetime of single CdSe/ZnS quantum dots". *Phys. Rev. Lett.*, 90(25 I):257404, 2003.

[68] G. Bacher, R. Weigand, J. Seufert, V. D. Kulakovskii, N. A. Gippius, A. Forchel, K. Leonardi, and D. Hommel. "Biexciton versus exciton lifetime in a single semiconductor quantum dot". *Phys. Rev. Lett.*, 83(21):4417, 1999.

[69] A. Malko, D. Y. Oberli, M. H. Baier, E. Pelucchi, F. Michelini, K. F. Karlsson, M. A. Dupertuis, and E. Kapon. "Single-photon emission from pyramidal quantum dots: The impact of hole thermalization on photon emission statistics". *Phys. Rev. B*, 72(19):195332, 2005.

[70] K. Sebald, P. Michler, T. Passow, D. Hommel, G. Bacher, and A. Forchel. "Single-photon emission of CdSe quantum dots at temperatures up to 200 k". *Appl. Phys. Lett.*, 81(16):2920, 2002.

[71] S. M. Ulrich, M. Benyoucef, P. Michler, N. Baer, P. Gartner, F. Jahnke, M. Schwab, H. Kurtze, M. Bayer, S. Fafard, Z. Wasilewski, and A. Forchel. "Correlated photon-pair emission from a charged single quantum dot". *Phys. Rev. B*, 71(23):235328, 2005.

[72] L. Besombes, K. Kheng, L. Marsal, and H. Mariette. "Acoustic phonon broadening mechanism in single quantum dot emission". *Phys. Rev. B*, 63(15):1553071, 2001.

[73] P. Borri, W. Langbein, S. Schneider, U. Woggon, R.L. Sellin, D. Ouyang, and D. Bimberg. "Ultralong dephasing time in InGaAs quantum dots". *Phys. Rev. Lett.*, 87(15):157401, 2001.

[74] I. Favero, G. Cassabois, R. Ferreira, D. Darson, C. Voisin, J. Tignon, C. Delalande, G. Bastard, Ph Roussignol, and J. M. Geérard. "Acoustic phonon sidebands in the emission line of single InAs/GaAs quantum dots". *Phys. Rev. B*, 68(23):233301, 2003.

[75] J. Szczytko, L. Kappei, J. Berney, F. Morier-Genoud, M. T. Portella-Oberli, and B. Deveaud. "Determination of the exciton formation in quantum wells from time-resolved interband luminescence". *Phys. Rev. Lett.*, 93(13):137401, 2004.

[76] P. Senellart, E. Peter, J. Hours, A. Cavanna, and J. Bloch. "Few particle effects in the emission of short-radiative-lifetime single quantum dots". *Phys. Rev. B*, 72(11):1, 2005.

[77] M. Koashi, K. Kono, T. Hirano, and M. Matsuoka. "Photon antibunching in pulsed squeezed light generated via parametric amplification". *Phys. Rev. Lett.*, 71(8):1164, 1993.

[78] ARDA. "A quantum information science and technology roadmap". *http://qist.lanl.gov*, 2004.

[79] N. Lütkenhaus. "Estimates for practical quantum cryptography". *Phys Rev A*, 59(5):3301, 1999.

[80] E. Moreau, I. Robert, L. Manin, V. Thierry-Mieg, J. M. Gérard, and I. Abram. "Quantum cascade of photons in semiconductor quantum dots". *Phys. Rev. Lett.*, 8718(18):257401, 2001.

[81] M. Pelton, C. Santori, J. Vučković, B. Zhang, G. S. Solomon, J. Plant, and Y. Yamamoto. "Efficient source of single photons: A single quantum dot in a micropost microcavity". *Phys. Rev. Lett.*, 89(23):233602, 2002.

[82] V. Zwiller, H. Blom, P. Jonsson, N. Panev, S. Jeppesen, T. Tsegaye, E. Goobar, M. E. Pistol, L. Samuelson, and G. Bjork. "Single quantum dots emit single photons at a time: Antibunching experiments". *Appl. Phys. Lett.*, 78(17):2476, 2001.

[83] A. Malko, M. H. Baier, K. F. Karlsson, E. Pelucchi, D. Y. Oberli, and E. Kapon. "Optimization of the efficiency of single-photon sources based on quantum dots under optical excitation". *Appl. Phys. Lett.*, 88(8):081905, 2006.

[84] H. Rigneault, J. Broudic, B. Gayral, and J. M. Gérard. "Far-field radiation from quantum boxes located in pillar microcavities". *Opt. Lett.*, 26(20):1595, 2001.

[85] C. Becher, A. Kiraz, P. Michler, A. Imamoglu, W.V. Schoenfeld, P.M. Petroff, L. Zhang, and E. Hu. "Nonclassical radiation from a single self-assembled InAs quantum dot". *Phys. Rev. B*, 63:121312, 2001.

[86] G. N. Gol'tsman, O. Okunev, G. Chulkova, A. Lipatov, A. Semenov, K. Smirnov, B. Voronov, A. Dzardanov, C. Williams, and R. Sobolewski. "Picosecond superconducting single-photon optical detector". *Appl. Phys. Lett.*, 79(6):705, 2001.

[87] A. D. Semenov, G. N. Gol'tsman, and A. A. Korneev. "Quantum detection by current carrying superconducting film". *Phys. C*, 351(4):349, 2001.

[88] G. N. Gol'tsman, K. Smirnov, P. Kouminov, B. Voronov, N. Kaurova, V. Drakinsky, J. Zhang, A. Verevkin, and R. Sobolewski. "Fabrication of nanostructured superconducting single-photon detectors". *IEEE Trans. on Appl. Supercon.*, 13(2 I):192, 2003.

[89] R. H. Hadfield, M. J. Stevens, S. S. Gruber, A. J. Miller, R. E. Schwall, R. P. Mirin, and S. W. Nam. "Single photon source characterization with a superconducting single photon detector". *Opt. Expr.*, 13(26):10846, 2005.

[90] W. Slysz, M. Wegrzecki, J. Bar, P. Grabiec, M. G. Rska, V. Zwiller, C. Latta, P. Bohi, I. Milostnaya, O. Minaeva, A. Antipov, O. Okunev, A. Korneev, K. Smirnov, B. Voronov, N. Kaurova, G. Gol'tsman, A. Pearlman, A. Cross, I. Komissarov, A. Verevkin, and R. Sobolewski. "Fiber-coupled single-photon detectors based on nbn superconducting nanostructures for practical quantum cryptography and photon-correlation studies". *Appl. Phys. Lett.*, 88(26):261113, 2006.

[91] A. Verevkin, A. Pearlman, W. Slysz, J. Zhang, M. Currie, A. Korneev, G. Chulkova, O. Okunev, P. Kouminov, K. Smirnov, B. Voronov, G. N.

Gol'tsman, and R. Sobolewski. "Ultrafast superconducting single-photon detectors for near-infrared- wavelength quantum communications". *J. Mod. Opt.*, 51(9-10):1447, 2004.

[92] N. Namekata, S. Sasamori, and S. Inoue. "800 mhz single-photon detection at 1550-nm using an InGaAs/InP avalanche photodiode operated with a sine wave gating". *Opt. Express*, 14:10043, 2006.

[93] C. Zinoni, B. Alloing, C. Monat, V. Zwiller, L. H. Li, A. Fiore, L. Lunghi, A. Gerardino, H. de Riedmatten, H. Zbinden, and N. Gisin. "Time-resolved and antibunching experiments on single quantum dots at 1300 nm". *Appl. Phys. Lett.*, 88(13):131102, 2006.

[94] C. Santori, D. Fattal, J. Vuckovic, G. S. Solomon, E. Waks, and Y. Yamamoto. "Submicrosecond correlations in photoluminescence from InAs quantum dots". *Phys. Rev. B*, 69(20):205324, 2004.

[95] J.M. Gérard, B. Sermage, B. Gayral, B. Legrand, E. Costard, and V. Thierry-Mieg. "Enhanced spontaneous emission by quantum boxes in a monolithic optical microcavity". *Phys. Rev. Lett.*, 81(5):1110, 1998.

[96] M. Bayer, T.L. Reinecke, F. Weidner, A. Larionov, A. McDonald, and A. Forchel. "Inhibition and enhancement of the spontaneous emission of quantum dots in structured microresonators". *Phys. Rev. Lett.*, 86(14):3168, 2001.

[97] G.S. Solomon, M. Pelton, and Y. Yamamoto. "Single-mode spontaneous emission from a single quantum dot in a three-dimensional microcavity". *Phys. Rev. Lett.*, 86(17):3903, 2001.

[98] Z. Yuan, B. E. Kardynal, R. M. Stevenson, A. J. Shields, C. J. Lobo, K. Cooper, N. S. Beattie, D. A. Ritchie, and M. Pepper. "Electrically driven single-photon source". *Science*, 295(5552):102, 2002.

[99] X. Huang, A. Stintz, C.P. Hains, G.T. Liu, J. Cheng, and K.J. Malloy. "Efficient high-temperature cw lasing operation of oxide-confined long-wavelength InAs quantum dot lasers". *Electron. Lett.*, 36(1):41, 2000.

[100] A. Fiore, J. X. Chen, and M. Ilegems. "Scaling quantum-dot light-emitting diodes to submicrometer sizes". *Appl. Phys. Lett.*, 81(10):1756, 2002.

[101] A. Yariv. *Optical Electronics*. Saunders College Publishing, New York, 1991.

[102] G. R. Hadley. "Effective-index model for vertical-cavity surface-emitting lasers". *Opt. Lett.*, 20(13):1483, 1995.

[103] M. Streiff, B. WItzigmann, C. Zinoni, C. Monat, B. Alloing, and A. Fiore. "Technology cad based design of semiconductor optical microcavities for single photon emitters". *Proc. SPIE*, 5840::602, 2005.

Carl Zinoni

Ch. Du Risoux 6, Morges, CH-1110, Switzerland

carl.zinoni@epfl.ch

+41(0)21 6935367(work) | +41(0)21 8033004 (home)

Availability: 1 Month notice

Date of Birth: 09 July 1971

Nationality: British and Italian

EDUCATION

Jan.03-Jan.07 **EPFL – ECOLE POLYTECHNIQUE FEDERALE DE LAUSANNE**   Lausanne, Switzerland

PhD: "Optical characterization of single quantum dots emitting at 1300nm"

- Low-temperature high-resolution optical spectroscopy of nanostructures and single photon correlation measurements at telecom wavelength.
- Designed and developed optical systems for highly sensitive measurements, including electronics and data acquisition software.
- Decreased the development time of the semiconductor single photon source through the implementation of two real-time image processing systems.

Sep.97-Jun.00 **SHEFFIELD HALLAM UNIVERSITY**   Sheffield, UK

1st Class Honours Degree in Engineering Physics

- Awards: - Môssbauer Prize for Excellence in Engineering Physics.
              - Alcan International Prize for Excellence on Industrial Placement.

Oct.93-Jun.95 **GLASGOW UNIVERSITY**   Glasgow, UK

Two years of a BSc. Honours Degree in Astronomy

- Award: Certificate of merit in Astronomy.

Sep.86-Jul.92 **FRANCESCO DE PINEDO, STATE AERONAUTICAL INSTITUTE**   Rome, Italy

Diploma di Maturità Tecnica Aeronautica. Grade: 80%

PROFESSIONAL EXPERIENCE

Oct.00-Dec.02 **CERN – EUROPEAN ORGANISATION FOR NUCLEAR RESEARCH**   Geneva, Switzerland

Fellowship

- Designed and developed a radiation tolerant Gas Flow Meter, 4000 are being installed.
- Managed the outsourcing for the development of the embedded software.

Jun.00-Sep.00 **BYTRONIC AUTOMATION LTD.**   Leamington SPA, UK

Development Engineer

- Developed process control and industrial automation systems.

Sep.98-Sep.99 **CERN – EUROPEAN ORGANISATION FOR NUCLEAR RESEARCH**   Geneva, Switzerland

Technical Student

- Reduced running costs by optimizing a gas purification system.
- Decreased detectors downtime through the development of a large distributed database enabling preventive maintenance.

Jul.96-Dec.96 **NATS – NATIONAL AIR TRAFFIC SERVICES LTD.**   Bournemouth, UK

Air Traffic Control Officer

- Ground Control, Take-off & Landing, Visual Aerodrome Area Control, Phraseology, Flying training.

Aug.91-Jun.00 **TEMPORARY POSITIONS**   UK, France and Italy

Occasional jobs with sales/market research agencies and holiday resorts.

COMPUTER SKILLS

- LabView, Matlab (Octave), C, HTML, Java Script, PLC programming.
- Developed online software for simulations of optical devices (http://ephotonics.epfl.ch/) and calculation of gas parameters (http://detector-gas-systems.web.cern.ch).

LANGUAGES

- Bilingual English and Italian, French good.

REFEREES

PROFESSIONAL:
Dr. Ferdinand Hahn
CERN, EP Division
CH-1211 GENEVE 23
Switzerland
ferdinand.hahn@cern.ch
Tel. +41(0)22 767 5851

ACADEMIC 1:
Prof. Andrea Fiore
EPFL FSB IPEQ GR/FI
CH-1015 Ecublens
Switzerland
andrea.fiore@epfl.ch
Tel.+41(0)21 353 34428

ACADEMIC 2:
Dr. Ian Halliday
Sheffiled Hallam University
School of Science and Maths
Sheffiled, S1 1WB - UK
i.halliday@shu.ac.uk
Tel.+44(0)114 225 3045

PUBLICATIONS

C. Zinoni, B. Alloing, L.H. Li, F. Marsili, A. Fiore L. Lunghi, A. Gerardino, Yu. B. Vakhtomin, K. V. Smirnov, G.N. Gol'tsman *"Single photonics at telecom wavelengths using nanowire superconducting detectors"* **Appl. Phys. Lett.** *submitted.*

B. Alloing, C. Zinoni, L.H. Li, A. Fiore and G. Patriarche *"Structural and optical properties of low-density and In-rich InAs/GaAs quantum dots"* **J. App. Phys.** *Accepted for publication.*

C. Zinoni, B. Alloing, C. Monat, V. Zwiller, L. H. Li, A. Fiore, L. Lunghi, A. Gerardino, H. de Riedmatten, H. Zbinden, and N. Gisin *"Time-resolved and antibunching experiments on single quantum dots at 1300 nm"* **Appl. Phys. Lett.**, Vol. 88, 131102 , 2006.

C. Monat, B. Alloing, C. Zinoni, L.H. Li and A. Fiore *"Nanostructured current-confined single quantum dot light-emitting-diode at 1300nm"* **Nano Letters** Vol. 6, Pages 1464-1467, 2006.

C. Zinoni, B. Alloing, C. Monat, L. H. Li, L. Lunghi, A. Gerardino and A. Fiore *"Time resolved measurements on low-density single quantum dots at 1300nm"* **QD 2006 Proceedings** – **Phys. Stat. Sol**. (c), Vol.11, 3717 (2006)

M. Streiff, B. Witzigmann, C. Zinoni, B, Alloing, C, Monat, and A. Fiore *"Technology CAD based design of semiconductor optical microcavities for single photon emitters"* **Proceedings of SPIE** Vol. 5840 PART II, Pages 602-613, 2005.

A. Fiore, C. Zinoni, B. Alloing, V. Zwiller, L. H. Li, and C. Monat *"Nanoscale single quantum dot devices at 1300 nm"* **Proceedings of SPIE** Vol. 5734, Pages 106-115, 2005.

B. Alloing, C. Zinoni, V. Zwiller, L.H. Li, C. Monat, M. Gobet, G. Buchs, A. Fiore, E. Pelucchi and E. Kapon, *"Growth and characterization of single quantum dots emitting at 1300 nm"*, **Appl. Phys. Lett.**, Vol. 86, 101908, 2005.

C. Zinoni, B. Alloing, C. Paranthoen, and A. Fiore, *"Three-dimensional wavelength-scale confinement in quantum dot microcavity light-emitting diodes"*, **Appl. Phys. Lett.**, Vol. 85, 2178, 2004.

CONFERENCES

C. Zinoni, B. Alloing, C. Monat, V. Zwiller, L.H. Li, and A. Fiore, "Time-resolved and antibunching experiments on single quantum dots at 1300nm" & "Nanoscale single quantum dot LEDs at 1300 nm", **Photonics West 2006**, *two oral presentations.*

C. Zinoni, B. Alloing, C. Monat, V. Zwiller, L.H. Li, and A. Fiore, "Time-resolved and antibunching experiments on single quantum dots at 1300nm", **MRS 2005**, *oral presentation.*